Ph.D. Thesis

Université de Limoges

UNIVERSITY OF LIMOGES

Doctoral School number 609 (SIMME)
Sciences and Engineering of Materials, Mechanic and Energetic

Institute of Research for Ceramics - UMR CNRS 7315

irCer

Year: 2021   Nb XXX

Hydroxyapatite-based architectured and nano-structured bioactive coatings fabricated by cold spray

Thesis submitted to University of Limoges in partial fulfillment
of the requirements of the degree of **Doctor of Philosophy**
Specialty: Ceramic Materials and Surface Treatments

Presented and defended by **Puiu Alberto ION** on March 26th, 2021
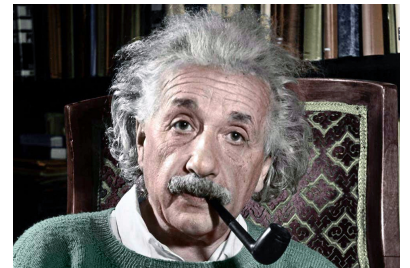
Co-supervisors: Dr Alain DENOIRJEAN, Dr Fabrice ROSSIGNOL and Dr Nicolas TESSIER-DOYEN

JURY:

Pr. Ghislaine BERTRAND	ENSIACET-CIRIMAT, Toulouse, France	President
Pr. Cécile LANGLADE	ICB-UTBM-LERMPS, Belfort, France	Reporter
Pr. Adelina IANCULESCU	University Politehnica of Bucharest, Romania	Reporter
Pr. Sophie COSTIL	ICB-UTBM-LERMPS, Belfort, France	Examiner
Dr. Vincent GUIPONT	Materials Center, MINES Paritech, Paris, France	Examiner
Ass. Pr. Nicolas TESSIER-DOYEN	IRCER, Limoges, France	Co-supervisor
Dr. Fabrice ROSSIGNOL	IRCER, Limoges, France	Co-supervisor
Dr. Alain DENOIRJEAN	IRCER, Limoges, France	Co-supervisor
Dr. Francis TOURENNE	Director Medicoat France, Etupes, France	Guest

"Imagination is more important than knowledge. For knowledge is limited, whereas imagination embraces the entire world, stimulating progress, giving birth to evolution."

Albert EINSTEIN (1879-1955)

Acknowledgements

Contents

List of Figures

List of Tables

List of Tables

Background and Motivation

Over the last decade, the biomaterials research field, especially bone implants, has been focused on the manufacturing of innovative implants with a long lifetime and able to i) improve bone in-growth rate, ii) reduce plaque after treatment and iii) remove largely the surgical re-intervention. In normal conditions, human bone can easily regenerate and in case of fractures some support devices take over the burden from the newly forming bone. However, in case of large traumas, diseases, or osteoporosis due to ageing, the bone has to be assisted to regenerate through the implants. Biocompatibility, osseointegration and strength are the three major factors that need to be considered when a material or combination of materials are used to develop implants for bone regeneration [36].

The employed graft materials and the macro- and micro-features in medical implant design are also relevant factors to succeed in creating a long-term implant. These implants need to be developed from materials that mimic the extracellular matrix structure with osteointegration and infection preventing abilities [37]. Nature-inspired materials or composite biomaterials can be employed to design different features and functionalize the metallic implant with nanometric and submicronic size coatings [36, 38].

The general purpose of a bioactive orthopaedic device is to stimulate the bone to regenerate. The implanted biomaterial is expected to withstand the applied physiological constraints without dimensional changes, brittle fracture or breaking in the long-term due to fatigue or stress corrosion.

The development of biomaterials used in medicine has evolved through three generations that are slightly overlapping even if they present different requirements. The first generation of materials used for implants needed to exhibit biological inertia with minimal reaction/interaction and present non-toxic properties [39]. In this generation, the most representative examples are zirconia and alumina which are still used in some prosthesis components provided that they ensure a suitable combination of functional properties [40]. However, their reliability is questionable in the cases when a foreign body response occurs or the micro-movements in the bone promote a failure of the implant [41].

In order to induce the desired therapeutic effect when implanted inside the body, research efforts were focused on biomaterials that are able to produce a favourable interaction with the living tissue and allow the biological healing process. The key properties of this second generation are bioactivity and/or resorbability [42]. Bioactivity promotes osteointegration for bonding and better stability of the implant for a longer functional life in comparison with the only bio-inert ceramics. Depending on the desired medical application field, the resorbable biomaterials rates could be tailored in the way that the foreign material introduced in the host body will be degraded to non-toxic and soluble products. Calcium phosphates, bioglasses, mesoporous silica and organic/inorganic hybrids are the most used materials belonging to this second generation of biomaterials.

The third generation of biomaterials is the result of the development of tissue-engineered implants designed to regrow rather than replace the tissues by utilizing scaffold of substances with biological activity in combination with bioceramics [43].

The bioactivity and biocompatibility are influenced by the specific chemistry and the topography of the implant surfaces. To enhance these properties different surface treatments are employed by developing coatings on the implant that will lead to superior osteointegration. These bioactive coatings, with high specific surface area, will encourage quicker solubility of the biomaterial, availability of ions in the surrounding area, and enhanced protein adsorption ability. The bioactive coating was initiated

by developing a layer of synthesized hydroxyapatite (HAp) on the surface of the implant.

Hydroxyapatite remains the "golden-standard" since it mimics the carbonated hydroxyapatite, the main inorganic constituent of bone tissue. In spite of this similarity, hydroxyapatite presents weaker mechanical properties than native bone. For high-load-bearing applications, hydroxyapatite is used as a bioactive coating on metallic substrates. Hydroxyapatite coating allows the significant improvement of the metallic implants (e.g., hip joints, dental implants, etc.) due to their excellent association of mechanical and biological properties.

Many techniques such as dip coating, sol-gel, pulsed laser deposition, sputtering, PVD, CVD, and plasma spraying have been employed to deposit HA coatings. Plasma sprayed implants are widely commercially available. However, long-term coating stability, structural morphology, and composition remain questionable. The main drawback of plasma spraying is the high temperature involved in the process favouring melting and solidification of the deposited materials [44].

Since cold spray utilizes kinetic rather than thermal energy for deposition, this promising method promotes unique characteristics compared to other conventional thermal spray techniques. Indeed, the cold spray permits to avoid undesirable phase transformations, and as well as to prevent grain growth, which is essential for better osteointegration [45].

The main objective of this work is to derive the benefit of cold spray capabilities to design coatings that perform outstanding bioactivity adapted to fulfil the patient's necessity, overcoming the actual issues of implants.

Chapter 1 briefly describes the various thermal spray technologies focusing on Cold Spray (CS) and their forecast evolution on the global market. The second part of this chapter reports an up-to-date review of ceramic deposition by CS and more specifically bioceramics such as hydroxyapatite (HAp) which is of particular interest for this PhD thesis. As highlighted in the literature, metals are the most suitable investigated materials in the CS deposition process because of their high plastic deformation and metallic bonding. Non-metallic materials, such as polymers, oxides and ceramics, and a combination of these materials, have started to receive considerable attention due to their promising applications in the bioengineering field. The bonding mechanism of ceramics coatings onto a metallic substrate by CS deposition technique is not yet completely understood. As presented in the literature, this mechanism is highly dependent on the particle-substrate hardness ratio, surface topography, and microstructure of the feedstock ceramic powder.

The second Chapter describes the characterization of the feedstock powders from commercially available HAp to hybrid composites obtained by spray-drying, along with the chemical and morphological modification of substrates used in this thesis. Since cold spray is a kinetic process, the powder remains in solid state and as a consequence, a special attention needs to be given to the feedstock and substrate. The powder need to be carefully adapted in terms of particle size distribution and morphology influencing the in-flight velocity and the ability to obtain an optimized fragmentation of particles on impact within the substrate. Some of HAp powdered granules were subjected to a preliminary thermal treatment of partial consolidation to adjust the mechanical response and further fragmentation ability. To control this fragmentation at the impact and mechanical anchor of the coatings, the substrates were adapted in terms of surface preparation through laser texturing, grit blasting and surface softening by titanium grade 2 deposition through CS. To derive the benefit of

the CS highly bioactive thermosensitive materials such as collagen, bioglass has been specially chosen as promising candidate. Collagen and bioglass-HAp hybrids exhibit an attracted growing interest for the bio-compatibility but also in fragmentation and consolidation. As the structural protein inside the body, Collagen can allow a fast regenerative cells growth on the defect area. Bioglass is able to add a corrosion protection to the implant of bodily fluids and minimizes the risk of toxic products entering in the body besides the osteoinductivity. Another issue addressed in this thesis is the development of effective anti-microbial coating in order to combat the antibiotic-resistant bacterial strains. We studied the possibility to functionalize the HAp powder surface with silver nanoparticles through Physical Vapor Deposition (PVD) on prior to CS, to overcome potential antibiotic resistance issues.

The first two sections of **chapter 3** present the understanding and implementations of HAp-based coatings using CS. Firstly, all the processing parameters (pressure, stand off distance, particle velocity influence, single-particle impact) were studied. In the second step, the characterization of the coatings build up proccess mechanism is performed. As presented in chapter 1, the CS ceramic quality not only depends on the process parameters but also on the feedstock powder and substrate characteristics. Since ceramics exhibit an intrinsic brittle nature, the ability to fragmentation and post-consolidation plays an essential role in the build-up of the coating. The third section is dedicated to novel functionality hybrid collagen (bioglass-hydroxyapatite) and antimicrobial bio-active silver nanoparticles hydroxyapatite coatings. These coatings may favour a faster osteointegration that guarantees the implantation success and provide a longer implant life improving the patient comfort and reducing the costs imposed by reimplantation and administration of drugs.

The last short **chapter 4** is devoted to *in vitro* biological tests of cell proliferation and adhesion to determine the viability and cytotoxicity of the various HAp-based coatings produced by cold spray.

Chapter 5 gives the final conclusion and draw future perspectives.

French and English abstracts of this PhD thesis are given on the last page of the manuscript.

Chapter 1 : Literature review

Overview ───

In this chapter, we first give a brief description of thermal spray technologies with a specific focus on Cold Spray (CS), as well as the forecast evolution of the global thermal spray market in revenue by industrial sectors and the market share for each thermal spray technology. In a second part, we present the forefront researches on CS of ceramics and more specifically bioceramics like hydroxyapatite (HAp) which is of particular interest for this PhD thesis. It is shown that the main advantage of CS is that it involves kinetic energy for consolidation rather than thermal energy compared to well-established thermal spray technologies. As a consequence, CS is less sensitive to oxygen in the atmosphere during the deposition process and possibly no thermal post-treatment is necessary to get the final consolidation.

1.1 The world of coatings - Thermal Spray

1.1.1 Definition

Thermal spray (TS) techniques (Figure 1.1) are coating processes in which melted, partially-melted or even unmelted particles of a size of several tenths of microns are sprayed and accumulated onto a surface using a carrier gas at high velocity (typically hundreds of m·s^{-1}). Thermal spray can provide thick coatings (approx. thickness range from 20 microns to several mm, depending on the process and feedstock), over large areas at high deposition rates as compared to other coating processes (*e.g.* electroplating, physical and chemical vapour deposition, sol-gel, etc.). Coating materials available for thermal spray include metals, alloys, ceramics, plastics and composites [1, 46, 47].
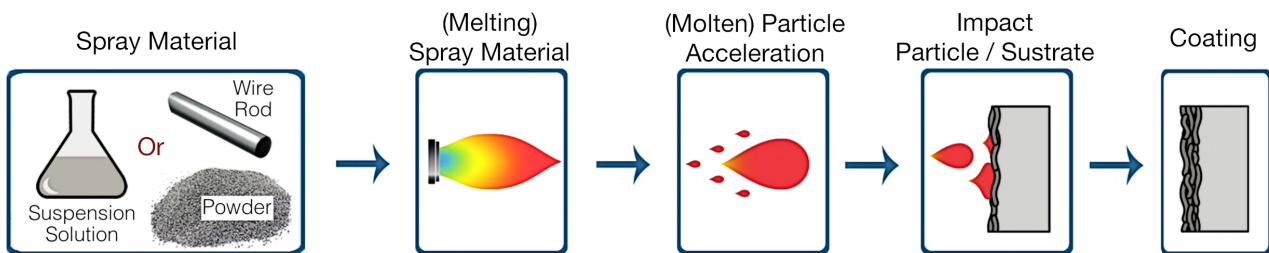
Figure 1.1 – *Thermal spray techniques, adapted from [1].*

1.1.2 Market

The sector of thermal spray coating is among those exhibiting the largest CAGR[1] (Figure 1.2). As per one of the latest surveys published on the topic, the global thermal spray coating market was valued at around US\$ 10 billion in 2019 (by revenue) and was projected to expand at a CAGR of 6.5% from 2015 to 2024. The market should then reach nearly US\$ 15 billion by 2024.

In Europe, the market is strongly dominated by Germany, followed by UK and France (Figure 1.3.a). Europe and North America have almost the same weight on the market, the sum of both representing nearly 2/3 of the overall activity (Figure 1.3.b). Major

Figure 1.2 – *Industries with largest CAGR.*

application fields are linked to the automotive, aerospace and healthcare sectors (Figure 1.3.c).

Key players involved worldwide in this market are Oerlikon Metco, A&A Coatings, Praxair Surface Tech., Flame Spray Coating Comp., Air Products & Chemicals, General Magnaplate Corp., Cincinnati Thermal Spray Inc., H.C. Starck GmbH (now Kyocera GmbH), Bodycote and TWI Ltd, just to name a few.

---

[1]CAGR (Compound Annual Growth Rate) is used in business and investing in accounting for the geometric progression ratio that provides a constant rate of return over the time. The rate of return is the one that would be required for an investment to grow from its beginning balance to its ending balance, assuming the profits were reinvested at the end of each year of the investment's lifespan.

Figure 1.3 – *(a) European and (b) world thermal spray market share, (c) Major application fields [2]*

1.1.3 Thermal Spray Technologies

Several types of thermal spray technologies can be distinguished (Figure 1.4.a). The corresponding equipment market evolution is quite stable in many application fields (Figure 1.4.b), except for the aerospace and electronic domains for which the increase is expected to be quite significant in the future. The thermal spray technologies can be categorized into three groups according to the way the energy is generated: combustion, electrical discharge plasma, kinetic energy.

In classical technologies (developed in the early 20th century but still widely used), such as flame and electric arc spraying, the particles velocities are "quite" low (< 150 m.s^{-1}) and the raw materials have to be entirely molten (*i.e.* droplets) to be properly deposited. Instead, plasma spraying, developed in the 1970's, exploits a high-temperature plasma jet generated by an arc discharge with temperatures above 10000°C. It makes it possible to spray refractory materials such as ceramic oxides (*e.g.* alumina, zirconia, etc.). Those materials can be melted (or partially melted) in the plasma and are accelerated typically above 300 m.s^{-1} [1, 46, 48, 49, 50].
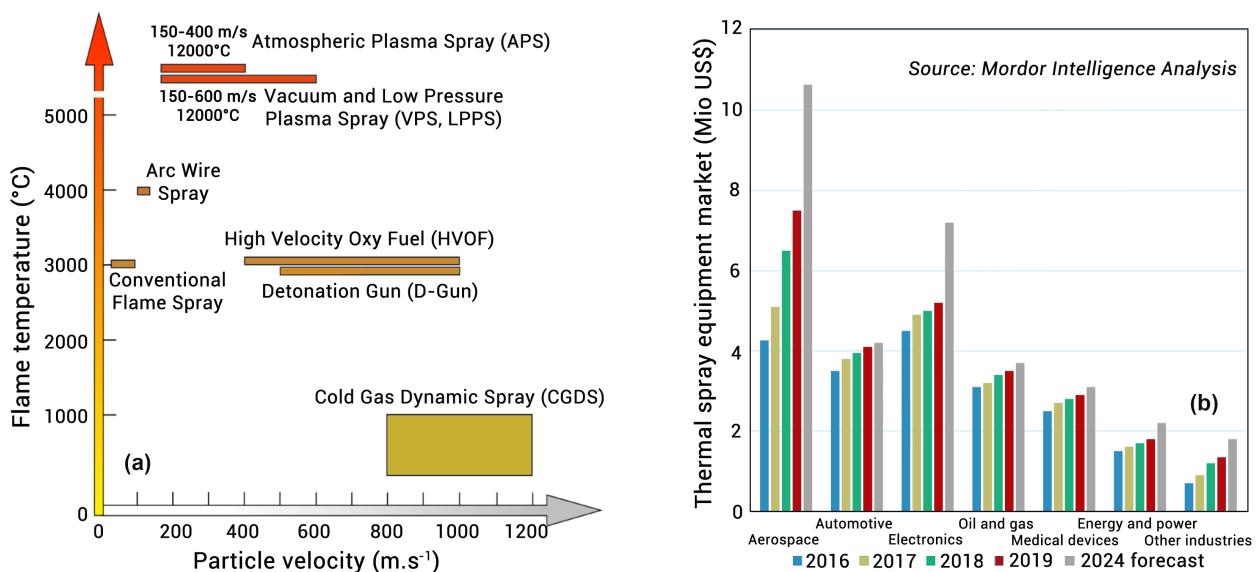
Figure 1.4 – *(a) Classification of thermal spray technologies as a function of particles velocity and flame temperature[3], (b) Evolution of thermal spray equipment market in revenue by industrial sectors.*

Finally, one of the most recent technologies, developed in Russia in the middle of the 80's and of interest for this PhD, is the Cold Gas Dynamic Spray (CGDS, usually abbreviated as Cold Spray (CS)). Here, particles are accelerated at very high speeds (up to 1200 m.s^{-1}) by a carrier gas forced through a convergent-divergent nozzle. The gas can be heated up to 1100°C to improve the acceleration capability. Soft metals such as Cu and Al are best-suited for CS, but coating of other materials (W, Ta, Ti, MCrAlY, WC–Co, etc.) has also been reported. However, the CS technology is not yet fully mature, so that CS is, at present, used more for R&D activities (60%) than for production (40%) [4]. It is especially the case for ceramic coatings for which CS is still a great challenge and a field of intensive research [51, 45, 4].

It is interesting to notice that, despite the significant growth of the thermal spray coating market already mentioned (Figure 1.2), the market of the associated thermal spray equipment remains itself relatively stable, except for the fields of aerospace and electronics (Figure 1.4.b). This is actually an obvious indirect indication of the maturity, reliability and high production capabilities of the technologies already implemented at the industrial level.
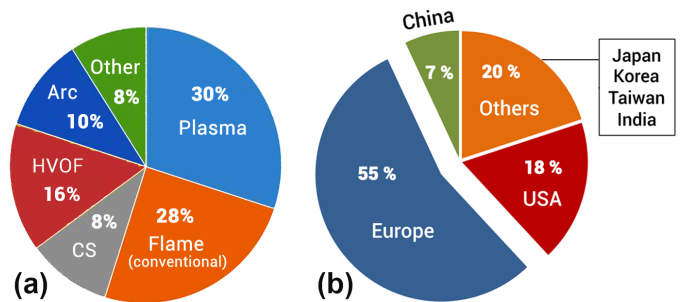
Figure 1.5 – *(a) Market share between thermal spray technologies,(b) CS equipment worldwide [4].*

Among these well-proven industrial thermal spray technologies, the most used ones are plasma spraying, combustion flame spraying and HVOF (Figure1.5.a). Dealing more specifically with CS equipment, Europe is clearly the leader in terms of the number of equipments (55%), followed by the USA and China (Figure 1.5.b), with a significant part of these equipments still dedicated to R&D [4].

The sections 1.1.3.1 to 1.1.3.4 briefly describe the four families of thermal spray technologies.

1.1.3.1 Combustion Flame Spraying

Combustion Flame Spraying is the simplest and the oldest thermal spray process family developed by Dr. Schoop in 1912. It can be divided into two sub-categories: conventional low velocity processes (*e.g.* wire/rod/cord and powder spraying) and high velocity processes (*e.g.* High-Velocity Oxy-Fuel spraying (HVOF), Detonation-Gun spraying (D-Gun^{TM})) [1, 46, 47]. The flame temperature and enthalpy depend mostly on the ratio between the fuel gas (C$_x$H$_y$) and the oxygen contents, as well as on the pressure. The temperature can reach 3500°C. The main advantages are the competitiveness in terms of process cost and operability (*i.e.* portable, easy to perform) [1, 46, 47].

$$2\,C_2H_2 + 5\,O_2 \longrightarrow 4\,CO_2 + 2\,H_2O \ (\textit{example of combustion with acetylene as fuel gas})$$
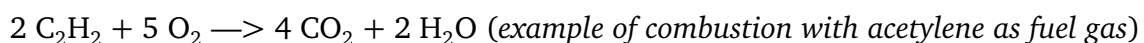
Conventional Wire/Rod/Cord and Powder Flame Spraying

In the case of wire/rod/cord spray technologies (Figure 1.6.a), the wire (or rod, or cord) is fed axially and continuously in the flame and melted. Then the material is atomized into droplets by a compressed air stream and propelled at velocities up to 100 m.s^{-1} towards the substrate. The French Company Saint-Gobain offers one of the most versatile system of this kind which can be used to spray metal wires, cored wires, flexicords and ceramic rods [1, 46, 47]. As for the powder spray technology (Figure 1.6.b), the design does not integrate any compressed air stream for atomization, and the powder is generally fed perpendicularly to the flame axis.
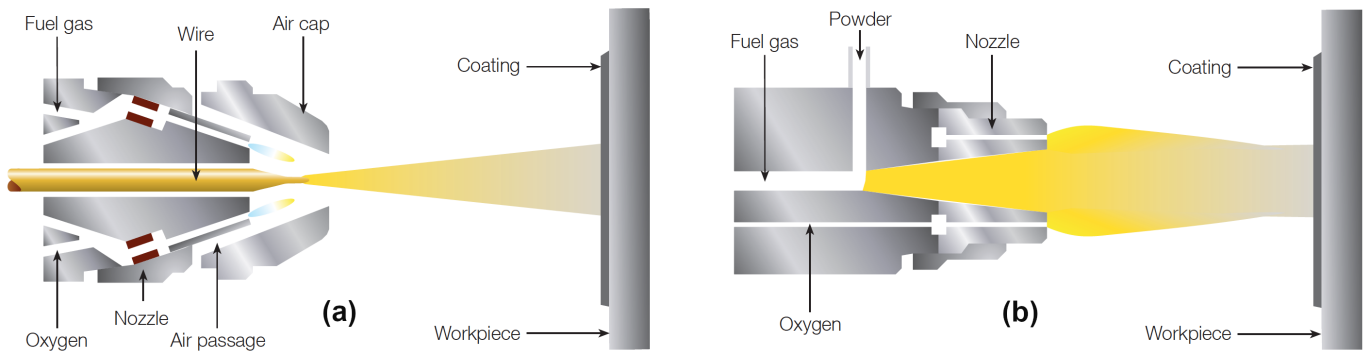
Figure 1.6 – *Conventional combustion flame spray technologies: (a) wire/rod/cord and (b) powder [5].*

High-Velocity Oxy-Fuel Spraying (HVOF)

This process is a "high-velocity flame-spray process" exploiting the fuel combustion at more than 1 atm in a pressurized chamber (Figure 1.7.a). Fuel may be gases like propane, propylene, acetylene, hydrogen and natural gas or liquids like kerosene. The hot gas generated by the combustion expands and accelerates through a "de Laval" nozzle.[2] The feedstock powder can be fed into the system axially or radially, entrained into the high-velocity jet, and accelerated through the barrel to deposit onto a substrate. The main advantage of HVOF stands in the high gas velocity that can reach up to 1000 m.s^{-1} [1, 46, 47].

Detonation-Gun Spraying (D-GUN)

The Detonation-gun technology is usually considered as the first invented thermal spray process that can be qualified as a high-velocity process. It uses a long, closed at one end and open at the other end, water-cooled gun barrel (Figure 1.7.b). Oxygen and fuel gas (usually acetylene, *i.e.* C_2H_2) mixture is fed into the barrel together with a powder load. A spark is used to ignite the gas mixture and the resulting detonation heats and accelerates the powder up to supersonic velocity (500 to 1000 m.s^{-1}) down the barrel. A pulse of nitrogen is used to purge the barrel after each detonation. This process is repeated many times a second (*e.g.* 15 times). The high kinetic energy of the hot powder particles at impact on the substrate results in the build-up of the coating.
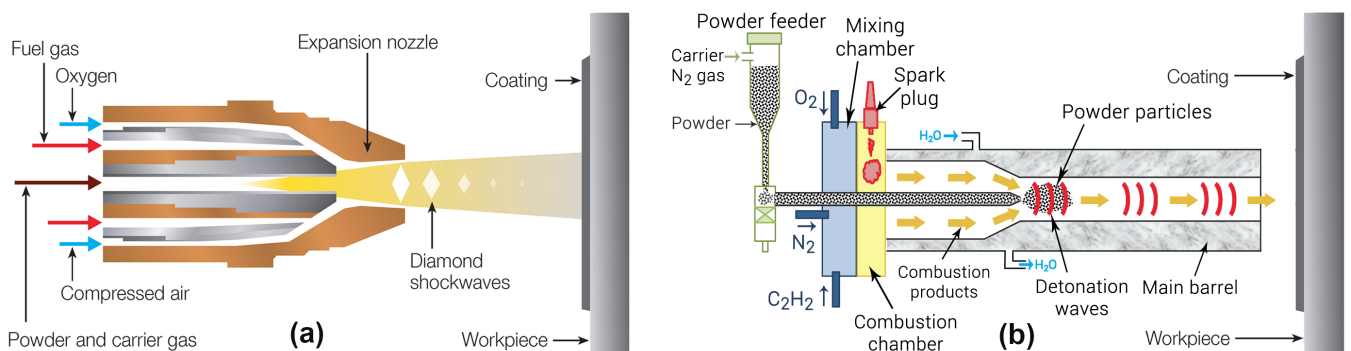
Figure 1.7 – *High velocity combustion flame spray technologies: (a) HVOF and (b)D-GUN [5].*

---

[2]A "de Laval" nozzle (also called convergent-divergent nozzle, CD nozzle or con-di nozzle) is a tube that is pinched in its middle. It is used to accelerate a hot, pressurized gas passing through it to a higher supersonic speed in the axial (thrust) direction, by converting the heat energy of the flow into kinetic energy.

1.1.3.2 Plasma Spraying

The plasma spraying processes (Figure 1.8.a) are using arcs and plasma as energy generation with different types of torches: d.c. Plasma Spraying (PS), Plasma-Transferred Arc Deposition (PTA), Vacuum Induction Plasma Spraying (VIPS).

d.c. Plasma Spraying (PS)

In this case, a strong electric arc is generated between an anode and a cathode. It ionizes a flowing gas into a high enthalpy plasma. The feedstock material is injected into the plasma jet, where it is melted (or partially melted) and propelled onto the substrate surface. The feedstock can be injected in the form of a powder, a suspension (Suspension Plasma Spraying, SPS) or a solution/precursor (Solution and Precursor Plasma Spraying (SPPS)). d.c. Plasma Spraying is one of most versatile of all thermal spraying processes, which can be applied to a wide variety of coatings performed in the ambient atmosphere (APS) or in vacuum (VPS). The characteristics of the coatings such as their porosity, local micro(nano)structure, roughness, cohesion and adhesion are fundamentally related to the interaction of the feedstock with the plasma jet [1, 46, 47].

Plasma-Transferred Arc Deposition (PTA) This process can be linked to the classical welding process. It is characterized by two electric arcs. The first one leads to a high-density plasma, obtained by ionization of Argon passing trough the electric arc formed between a non-consumable tungsten electrode (negative polarization) and a copper nozzle (positive polarization) into the welding torch (pilot arc). The second electric arc, called Transferred Arc, produces the energy needed to melt both the base metal and the filler metal. The transferred arc is "throttled" to obtain a further increase of the temperature. The plasma plume can reach a temperature up to 18000°C [1, 46, 47].

Vacuum Induction Plasma Spraying (VIPS) The torch consists essentially of a plasma confinement ceramic tube with its outer surface cooled using a high-velocity thin-film water stream. A water-cooled induction copper coil surrounds the ceramic tube creating an alternating magnetic field in the discharge cavity. On ignition, a conductive plasma load is produced within the discharge cavity, in which the energy is transferred through electromagnetic coupling. An internal gas flow introduced through the gas distributor head ensures the shielding of the internal surface of the ceramic tube from the intense heat to which it is exposed. The hot plasma gases exit the torch cavity through the downstream flange-mounted nozzle [1, 46, 47].
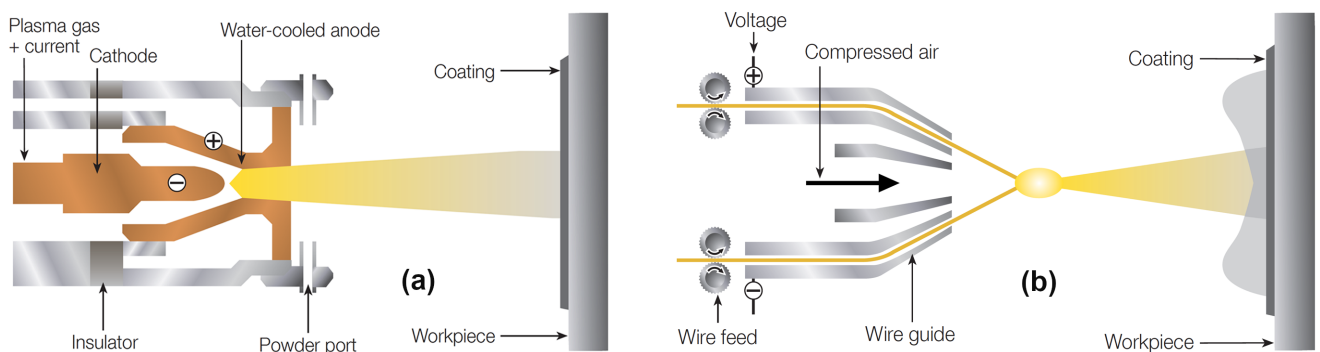
Figure 1.8 – *(a) Plasma spray and (b) Electrical arc wire spray technologies [5].*

1.1.3.3 Electrical Arc Wire Spray

Two metallic wires (usually of the same composition) are electrically charged with opposing polarity, feed into the gun and the tip of wires is continuously melted by an electrical arc. The compressed air jet then atomizes the now molten material and accelerates it onto the surface to form the coating, as shown schematically in Figure 1.8.b. The gas velocities are of a few hundreds of m·s⁻¹, but the gas is practically not heated by the arc, allowing one to keep the substrate temperature below a few tens of °C without cooling. For this reason, even polymer substrates can be coated [1, 46, 47].

1.1.3.4 Cold spraying

Cold spray (CS), formerly called Cold Gas Dynamic Spray (CGDS), is a solid-state coating process in which material is accelerated at supersonic velocities in a range between 300 and 1200 m·s⁻¹ through a "de Laval" nozzle toward the surface of the substrate by an inert carrier gas. Cold spray is a promising technology allowing to obtain thermal- and oxygen-sensitive coatings on different substrates.

      CS is based on the kinetic energy of the particles and not on the thermal energy. In this process, no high-temperature source is used to melt and deposit the feedstock material, like for flame or plasma spraying, so that the feedstock materials do not thermally degrade through oxidation or through other chemical reactions that can take place during the deposition. The coatings obtained in CS are thick (up to hundreds of microns), have even free-standing shapes. In addition, materials that are often hard to spray with conventional thermal spray techniques can even be deposited, such as amorphous materials, nanophase materials, intermetallics... This process can also be employed as an additive manufacturing process. Finally, during CS, the formation of brittle phases and grain growth is avoided [51, 45].
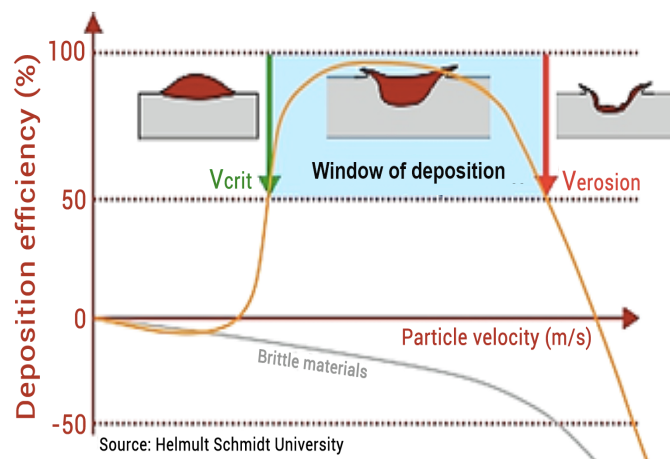
Figure 1.9 – *Correlation between the particles velocity and the deposition efficiency [6].*

In CS, the kinetic energy is dissipated at the impact on the substrate into heat, plastic deformation and or brittle fragmentation leading to the build-up of the coating [52]. The particles are mainly dependent on the carrier gas (pressure and temperature) and on the nozzle specific geometry [53]. The adhesion to the substrate takes place when the powder particles exceed a critical impact velocity. This velocity depends on the physico-chemical properties of the chosen material that will be sprayed, such as particle size and shape, melting temperature and specific heat [52]. These properties influence the deposition efficiency (DE), defined as the ratio between the mass of the particles that are adherent to the substrate and the total mass of sprayed particles. Figure 1.9 shows such a feedstock material DE (Deposition Efficiency) as a function of the critical velocity, when the temperature of the gas is constant. DE can be defined in agreement with the following relation 1.1:

$$DE = \frac{m_s}{M_p} \cdot 100 \tag{1.1}$$

With 'm_s' the mass of the coating and 'M_p' the total mass of sprayed particles.

As already mentioned before, one of the most important factor in CS is the critical velocity, (V_{crit}), which is defined as the minimum particle velocity required for a material to adhere to the substrate. Assadi *et al.* [54] used numerical modeling to predict V_{crit} in the case of metals. The results gave the following equation:

$$V_{crit} = 667 - 0.014\rho + 0.08\left(T_m - T_{Ref}\right) + 10^{-7}\sigma_{uts} - 0.4\left(T_i - T_{Ref}\right) \qquad (1.2)$$

where 'ρ' is the particle density, 'T_m' the melting temperature, T_{Ref}' the reference temperature at which the ultimate tensile strength is determined, 'σ_{uts}' the ultimate tensile strength, and 'T_i' the initial particle temperature.

The work of Assadi *et al.* [54] did not consider the size of particles which is actually a significant factor in determining V_{crit}. Schmidt *et al.* [6] developed another correlation in order to predict V_{crit}:

$$V_{crit} = \sqrt{\left[4F_1\sigma_{uts}\left(1 - \frac{T_i - T_{Ref}}{T_m - T_{Ref}}\right)\rho_p^{-1}\right] + F_2 c_p\left(T_m - T_i\right)} \qquad (1.3)$$

where 'σ_{uts}' is the ultimate tensile strength, 'T_{Ref}' the reference temperature for which the ultimate tensile strength is determined, 'T_i' the initial particles temperature, 'T_m' the melting point of the particles, 'ρ_p' the density of particles, 'F_1' and 'F_2' two constants that represent material-dependent calibration factors, and 'c_p' the particles specific heat capacity.

As it can be seen from 1.9, when the critical velocity is reached, the deposition of particles on the substrate takes place and a coating is formed with a significant adhesion and consolidation. On the contrary, if the particles velocity is below the critical one, particles do not attach well to the substrate or simply rebound at the impact on it. Actually, in these conditions, a coating may be formed but it looks more like a simple stacking of particles with no real bonding between them. Then, by increasing the velocity above V_{crit}, the deposition efficiency and the bonding strength between particles increase until a new velocity threshold is reached. At this threshold, called $V_{erosion}$, an erosion phenomenon starts to occur preventing from any coating build-up. We mean by erosion something similar to sand blasting. Van Steenkiste *et al.* [7] proposed a model to explain the coating build-up in the CS process and in the specific case of metallic powders, i.e. > 50 μm aluminium powder (figure 1.10). This model considers four basic stages: (1) the substrate cratering for the first layer of the coating by fracturing the surface oxide layer of the substrate, (2) the particles deformation and realignment as a result of successive particles impacts, (3) the formation of metallic bonds that reduce porosity, and (4) the further densification and hardening of the coating.

Figure 1.10 – *Coating build-up stages in the CS process for metallic powders [7].*

Other studies reported in the literature are focused on the control of the bonding mechanisms of a soft/hard system in order to optimize the CS parameters and obtain a high deposition

efficiency. These bonding mechanisms are linked to the deposition and deformation behaviours that occur at the particle/substrate and particle/particle contacts [54, 8, 55, 56, 57, 10, 58]. More specifically, the strong pressure field that is propagating spherically into the particle and substrate from the point of contact can generate a shear load that accelerates the material laterally causing a localized shear strain. Under critical conditions, this shear load leads to adiabatic shear instability, that can conduct to a viscous flow of material in an outward flowing direction at temperatures close to its melting temperature. This excessive lateral deformation of the material is called jetting [59]. The material jetting makes the surfaces mutually conforming by removing the oxides and providing good atomic interactions between the clean contacting interface at high contact pressures [56].

The thermal and mechanical properties of the feedstock powder are also crucial factors in the bonding process between the substrate and the particles [60]. Figure 1.11 presents the critical velocities for 25 μm particles of different materials, calculated and experimentally determined, compared with 20 mm ball impacts. The critical velocities determined experimentally show a better agreement with the Schmidt's equation 1.3.
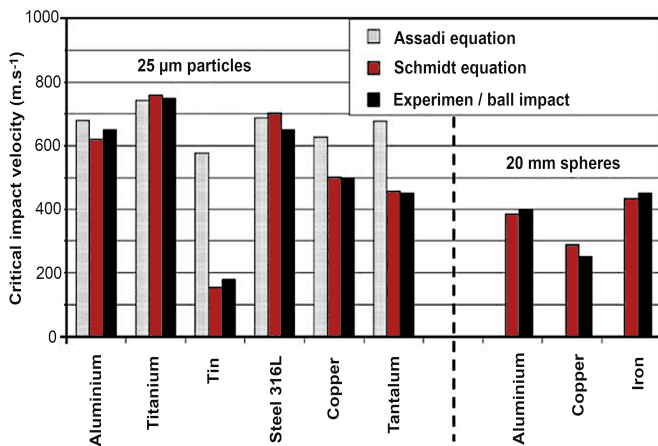
Figure 1.11 – *Correlation between particles velocity and deposition efficiency [8, 9].*

If the hard particles velocity is low, a deformation of the soft substrate may occur. Then, when increasing the particles velocity, there is a considerable deformation of the particles onto the substrate that creates bonding in the particles/substrate region and it can sometimes be observed that the substrate itself remains undeformed. For the highest particles velocities, the particles and the substrate both deform significantly [61].

Now, as reported in Figure 1.12, four possible types of interactions may actually occur in the CS process between the particles and the substrate : (a) soft particles onto a soft substrate (*e.g.* Al/Al), where, due to the material strength, large deformation can be observed, as compared with (b) hard particles onto a hard substrate (*e.g.* Ti/Ti); for (c) soft particles onto a hard substrate (*e.g.* Al/mild steel), and (d) hard particles onto a soft substrate (*e.g.* Ti/Al), the deformation will occur in the relative soft counterpart. The highest temperature was registered at the substrate side for the (a) and (b) cases, and at the softer side for the (c) and (d) cases[10].

The process parameters used in CS that influence the bonding, the deposition process and the formation of a coating are the propulsive gas parameters (pressure, temperature and type of gas), the powder feeder parameters (powder feed rate), the deposition parameters (traverse speed, scanning step, stand-off distance, spray angle and trajectory). The Table 1.1 summarizes the influence of those process parameters on the qualitative coating properties.

According to the pressure and temperature of the inert carrier gas, the CS technique can be separated in two main categories: the high-pressure cold spray (HPCS) (> 1 MPa, 500°C - 1100°C) and the low-pressure cold spray (LPCS) (< 1 MPa, <500°C). The Figure 1.13 shows the schematic representations of HPCS and LPCS.
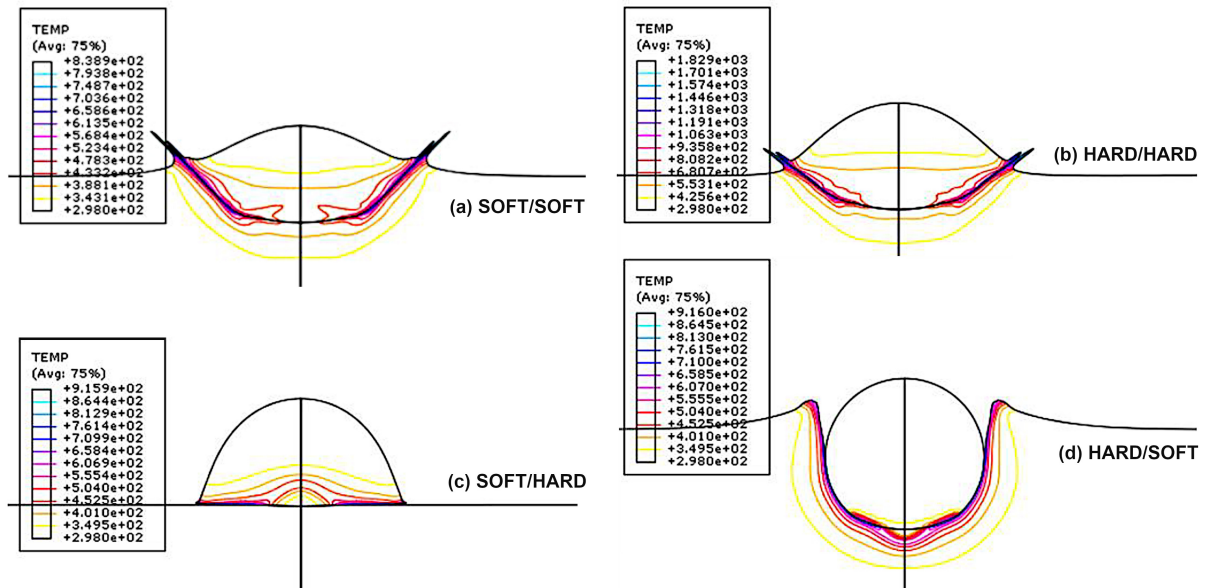
Figure 1.12 – *Four types of particles/substrate interactions observed in CS: (a) soft/soft (e.g. Al/Al), (b) hard/hard (e.g. Ti/Ti), (c) soft/hard (e.g. Al/Ti) and (d) hard/soft (e.g. Ti/Al) [10].*

Process parameters	Mechanical strength	Coating adhesion	Coating porosity	Residual stress	Deposition efficiency
Gas pressure ↑	↑	↑	↑	↓	↑
Gas temperature ↑	↑	↑	↑	↓	↑
Gas molecular weight ↑	↓	↓	↑	↑	↑
Powder feed rate ↑	↓	↓	↑	↑	↑
Traverse speed ↑	↑	↑	↑	↑	↓
Stand-off distance ↑	↑	↑	↑	↓	↑

Table 1.1 – Qualitative coating properties as a function of the CS process parameters.
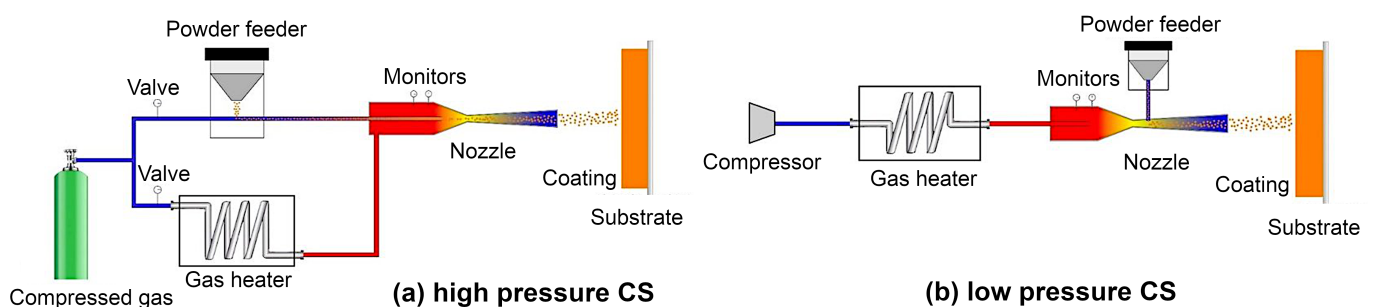
Figure 1.13 – *Schematic representations of: (a) high pressure CS and (b) low pressure CS systems [1].*

LPCS are small and compact systems, that can be transported without difficulties and that are being used in industrial platforms. As carrier gas, these systems use readily available compressed air or nitrogen. The materials deposited by LPCS are lighter, and they do not flow directly through the throat of the nozzle. Instead they are injected downstream into the gas. The deposition efficiency is then low when the sprayed materials are ceramics or also for some metals like copper or aluminium. [60].

In the HPCS system, the propulsive gases employed are those exhibiting a low molecular weight, such as nitrogen or helium, which will generate a higher velocity of the particles. The system is stationary and it is employed for spraying various feedstock materials with higher densities. The deposition efficiency is high even for hard materials such as titanium or molybdenum.

The most used feedstock materials in CS are:

- Metals: *e.g.* ductile materials (Aluminium, Copper); harder and less ductile materials (Titanium, Nickel); Silver, Magnesium, etc.

- Alloys: *e.g.* Titanium-Alloys, Aluminum-Alloys, Nickel-Chromium, Bronze, MCrAlY's, etc.

- Composites: *e.g.* metal matrix composites.

- "Soft" ceramics: *e.g.* TiO_2, ZnO, calcium phosphates.

The deposition efficiency is high for metals and alloys, as well as for composites containing metals. Usually, with such high deposition rates, the coatings produced by CS have a thickness ranging from 100–200 μm up to very high thickness values allowing to use CS as an additive manufacturing process in itself.

Unlike other thermal spraying techniques, where the particles are molten or semi-molten, in CS the particle temperatures remain below the melting temperature. Therefore, the coating process is a solid-state process, and the coatings formation occurs due to the particles kinetic energy release at the impact, which gives CS various advantages, such as:

- A high deposition efficiency (*e.g.* titanium 100% [12] and copper) and a high deposition rate (up to 14 Kg·h^{-1} for various materials [2]),

- A low porosity coating because of the viscoplastic deformation of the particles during deposition and tamping effect [7],

- A minimal thermal input to the substrate because of the absence of any high-temperature jet which might heat up the substrate significantly,

- A compressive residual stress in the coating because of plastic deformation in the solid-state,

- No phase change, no oxidation and no grain growth due to a lack of heating of the powders.

1.2   Ceramic coatings by Cold Spray (CS): A State of the Art

The CS deposition of ceramic powder feedstocks is considered challenging because of the intrinsic brittleness of ceramics. Actually, contrary to metals, ceramics rather fragment than undertake massive plastic deformation [13]. This lack of deformation capability conducts to the formation of quite thin coatings, with typically a maximum thickness of 100 μm. Even MAX-phase materials, which exhibit both ceramic and metallic properties, cannot usually exceed a thickness greater than 100 μm. In addition, at the direct impact with the substrate during the initial stage of the coating build-up, since the ceramic particles do not easily deform, a "monolayer" of these particles is generally embedded into the substrate. Subsequent impacts on that "monolayer" adhering to the substrate can cause its fracturing [62] [63].

The bonding mechanism of ceramic coatings onto metallic substrates by the CS deposition technique is not yet fully understood. A of the the literature shows that this mechanism is highly dependent on the particle-substrate hardness ratio, the surface topography that may limit the lateral movement of particles at the impact (Figure 1.14), and the microstructure of the feedstock ceramic powder [11].
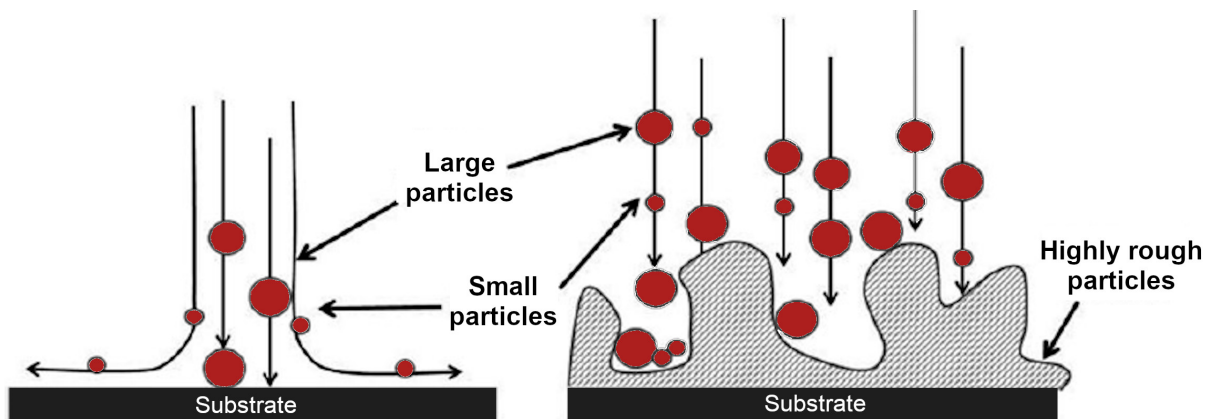
Figure 1.14 – *Influence of the surface topography on the particles-substrate interaction during CS [11].*

R. Chakrabarty and J. Song recently published a work in which they used systematic numerical simulations to study the dynamic fragmentation of ceramic particles in the CS process on different metallic substrates (Figure 1.15) [12]. The Johnson-Holmquist model (JH-2) was utilized to examine the fracture/damage of the ceramic particles, as well as of glass particles [64],[65]. The crater depth that was formed at the impact of the ceramic particles on the substrate was a crucial factor for the determination of the ceramic holding onto the substrate. A significant ceramic loss at the crater edges could be attributed to soft substrates due to the jetting in the CS process that induced highly localized plastic deformation. The effect of substrate roughness on the deformation and crater morphology in different substrates was also presented. The substrate that had a roughness lower than the particles radius (RRMS = 5 μm) was affected by jetting. With the increase of the particles radius (RRMS = 15 μm), the jetting was reduced. It became negligible for roughness values that were similar or larger to the particles radius. In the absence of jetting, the ceramic deposition was uniform in the crater for Cu substrate. For AlMg$_3$ substrates, the jetting led to localized plasticity at crater edges, followed by ejection and loss of ceramic fragments. A minor deformation, and a limited ceramic preservation influenced by thermal softening of the substrate, was observed on hard substrates such as Ti and stainless steel.
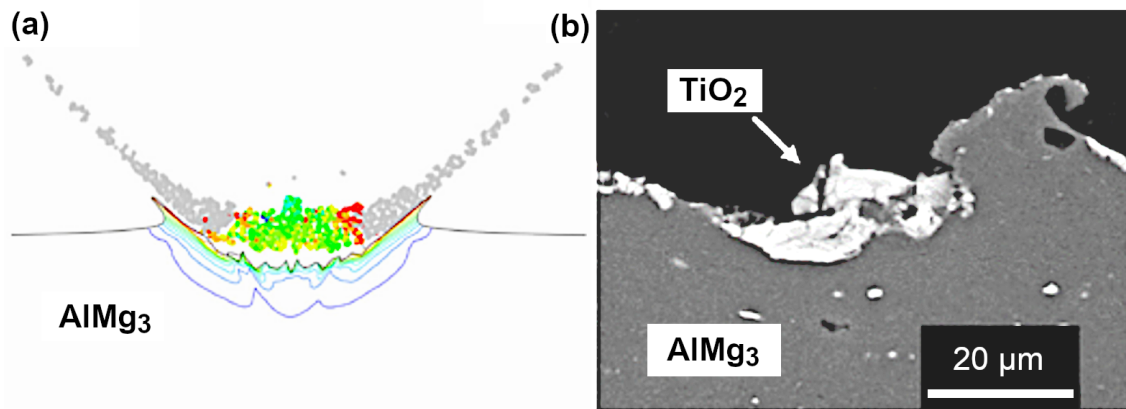
Figure 1.15 – *Simulated TiO$_2$ deposition morphology on a AlMg$_3$ substrate in (a) [12], as compared to experimentally observed deposition morphology in (b)[13].*

As reported in the literature, metals are the most investigated materials in the CS deposition process, because they are more suitable for consolidation by plastic deformation and metallic bonding [45]. However, non-metallic materials [66], such as polymers, ceramics like oxides, and a combination of these materials, have started to receive a considerable attention due to their applications, including the bio-engineering fields.

1.2.1   Ceramic coatings

Ceramics coatings were first deposited using CS by Li *et al.* [67] and J. Han *et al.* [68], as single layers. These authors more specifically studied the deposition of TiO$_2$ films with high photocatalytic activities. They showed that it was impossible to build-up relatively thick coatings. The thickness was around 15 μm and these coatings presented a porous structure formed by the stacking of nanoparticles.

M. Yamada *et al.* [69] demonstrated that it was possible to obtain thicker ceramic coatings of TiO$_2$ anatase by controlling the spraying parameters and by employing a self-designed CS equipment. They varied the gas temperature (from RT to 400°C) and observed that the deposition efficiency was enhanced by increasing the gas pressure. The maximum thickness they got was 100 μm. The obtained coatings maintained the grain size and crystal phase of the TiO$_2$ feedstock powder. For a better understanding of the influence of the gas nature (helium or nitrogen) and of the gas temperature on TiO$_2$ coatings fabrication by CS, M. Yamada *et al.* published another paper, one year later [14]. They observed that the nature of the gas did not influence the TiO$_2$ coatings and demonstrated again that the gas temperature influenced the thickness of the coatings (Figure 1.16).

J.-O. Kliemann *et al.* [13] reported on the TiO$_2$ impact on different substrates by CS. The bonding of this ceramic onto a ductile substrate was attributed to the adiabatic shear instability. In the bonding zones, only a small fraction of the brittle sprayed TiO$_2$ particles remained, due to the fracture caused by elastic rebound forces. If the effect of the elastic forces due to newly impacted particles was reaching the bond of the particles beneath already attached to the substrate, then the build-up of a coating was not possible due to the fracturing of the layer underneath. The second layer build-up, or a part of it, was however possible on AlMg$_3$. The deposition efficiency was increased when the velocity of the particles was higher and caused major deformation on the substrate till it reached a saturation limit.

K. Schmidt *et al.*[70] underlined similar conclusions about the build-up mechanism of such a TiO_2 coating on Ti substrates, in the case of CS of TiO_2 microparticles. The ceramic retention onto the substrate was attributed to the adiabatic instability and mechanical interlocking.

Finally, A. R. Toibah *et al.*[15] showed that, by adding $(NH_4)_2SO_4$ and using low-temperature hydrolysis at 120°C, they could obtain agglomerated nanocrystalline TiO_2 single-phase anatase, as confirmed by XRD (Figure 1.17). This specific feedstock formulation helped inducing plastic deformation during CS providing adequate pressure and temperature were used. As a result, the porosity of the as-obtained TiO_2 coatings was reduced due to the addition of $(NH_4)_2SO_4$. TEM images confirmed that the primary particles were nanoparticles. The coating build-up was the result of a tamping effect through slipping of nanoparticles during the particles collision. As suggested also by other authors, for dense ceramic powders, the success of the CS process is possible on hard substrates with the fracture of the particles when the Hugoniot Elastic Limit (HEL) of the ceramic is reached [71]. It is also possible on soft substrates where the first layer of ceramic particles is embedded in it. But, in this case, the second layer build-up is very difficult to obtain [72].
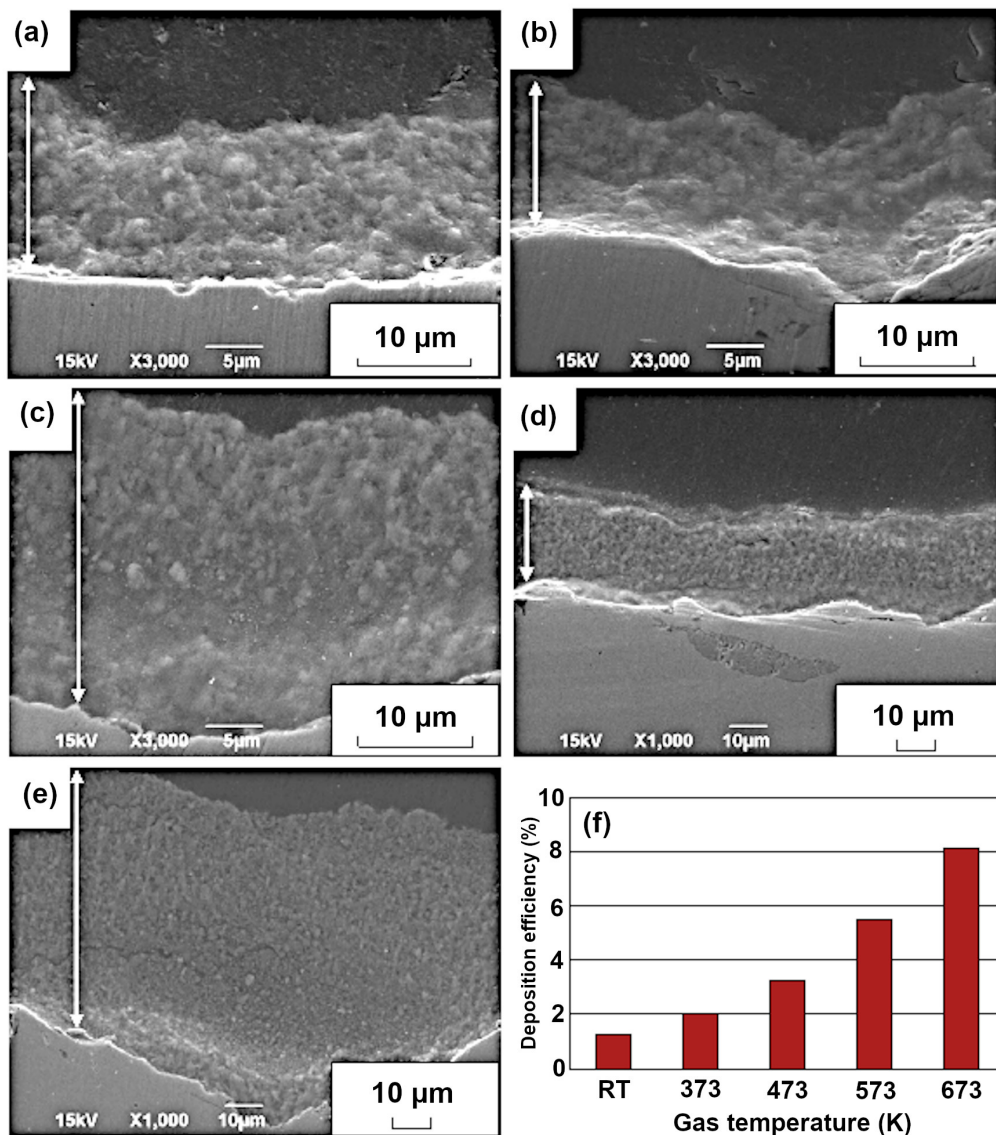
Figure 1.16 – *SEM images of TiO_2 coatings obtained at different gas temperatures: a) RT, b) 373 K, c) 473 K, d) 573 K and e) 673 K. f) Deposition efficiency for different gas temperatures [14].*

As another example, using a Low Pressure CS (LPCS) process, H. Y. Lee *et al.*[16] succeeded to deposit WO_3 on a silicon substrate (Figure 1.18). They showed that the obtained coating was adherent to the substrate and dense. There was no crater formation or plastic deformability during the LPCS process, and the build-up of the coating could be considered as ceramic on ceramic deposition. The bonding mechanism was attributed to the fragmentation of large size agglomerated particles upon their impact on the substrate. Good adhesion, great mechanical interlocking and voids reduction between the particles were attributed to the effect of surface roughness.
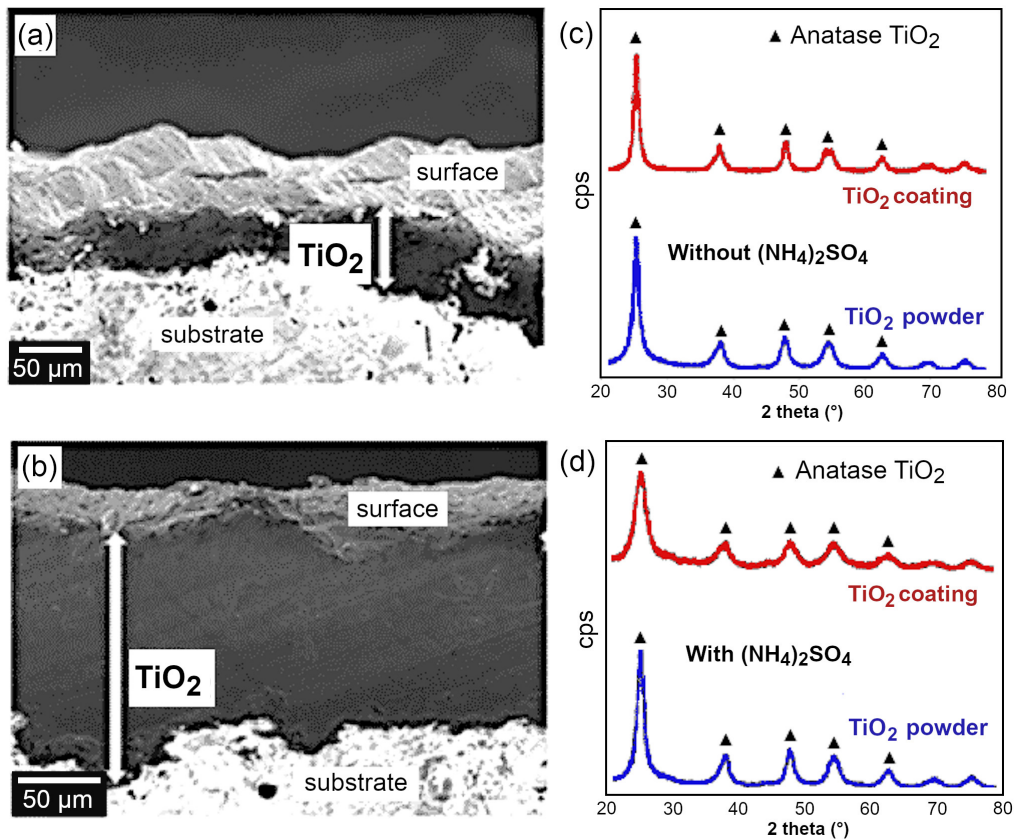
Figure 1.17 – *Cross-sectional SEM images of TiO_2 coatings on ceramic substrates and XRD patterns of as-obtained coatings using different types of TiO_2 powders: (a) and (c) TiO_2 without addition of $(NH_4)_2SO_4$, (b) and (d) TiO_2 with addition of $(NH_4)_2SO_4$ [15].*
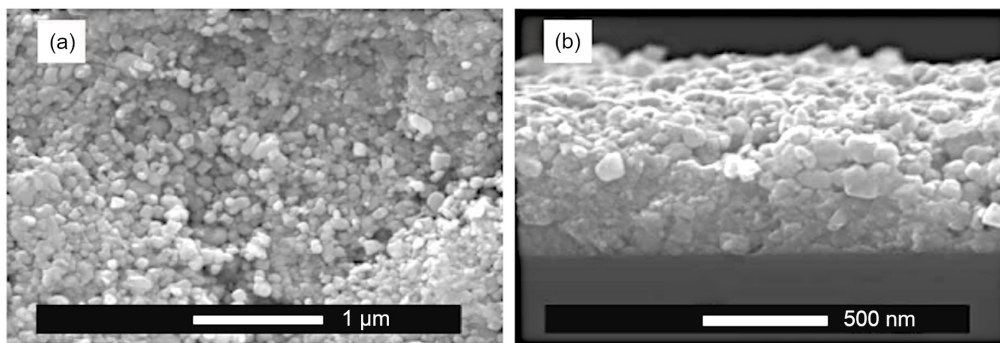
Figure 1.18 – *FE-SEM images of a WO_3 coating deposited by a Low Pressure CS process on a silicon substrate: (a) top view and (b) cross-section [16].*

1.2.2   Bioceramic coatings

Bioceramic materials made of Ca phosphates with various formulas such as hydroxyapatite (HA), sometimes doped with hetero-elements (*e.g.* Si), have been extensively studied in the literature as implants for Bone Tissue Engineering (BTE) due to their similarity in comparison to the mineral part of the bone [73]. For some applications requiring a significant mechanical strength and for which the brittleness of the ceramic is an issue, the implants can not be fabricated completely out of these Ca phosphate materials. The common consensus is to use for the core of the implant, a metal or a polymer as the main component, covered by an adherent ceramic coating exhibiting a bioactive surface. For this reason, it is key to select an appropriate technique to get coatings with a specific and controllable microstructure, together with a desired phase composition and crystallinity of the bioceramic, so that to improve cell attachment/proliferation and avoid the formation of biofilms [74].

For instance, to improve PEEK (polyetheretherketone) implants biocompatibility, J. H. Lee *et al.* covered the entire surface of the PEEK with HA by CS (Figure 1.19). It allowed preserving the mechanical properties of the PEEK while, at the same time, improving its biofunctionality [75]. In another CS study about HA deposition on PEEK, [76] the same authors prepared commercially available PEEK substrates as either a disk with a smooth surface or as a cube with periodic ridges. For disk-shaped PEEK samples, the temperature and the pressure of the carrier gas were set to 400°C and 1.4 MPa, respectively. For the cube-shaped PEEK samples, the temperature of the carrier gas was increased up to 500°C, and the pressure was set at 2.4 MPa. Mesenchymal stem cells grown on those different HA-coated PEEK implants demonstrated an increased alkaline phosphatase activity and calcium production. As for the *in vivo* tests, the authors demonstrated that the osseointegration rate and the regeneration of bone tissues were improved with those HA-coated PEEK implants.
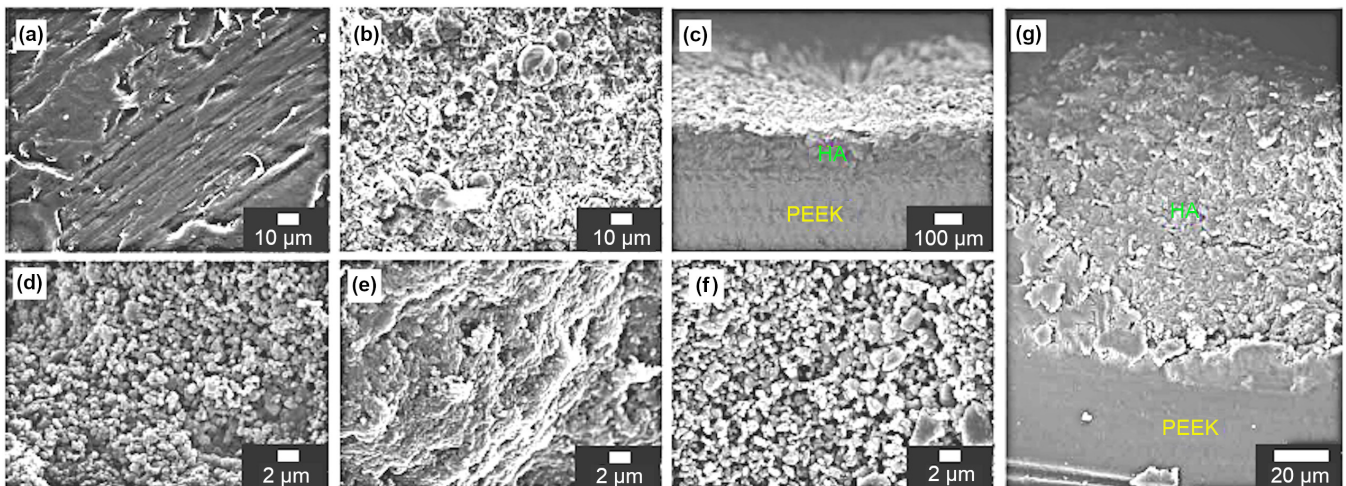
Figure 1.19 – *Top view SEM images of (a) an uncoated PEEK implant and of (b) a HA-coated disk-shaped PEEK implant by CS. (c) Cross-sectional SEM image of HA-coated disk-shaped PEEK implant by CS. SEM images of a HA-coated cube-shaped PEEK implant shown from: (d) the top, (e) the side, and (f) the bottom. (g) Cross-sectional SEM image of a HA-coated cube-shaped PEEK implant [16].*

Magnesium (Mg) is considered as a non-toxic material because it participates to the human metabolism. It is then used in implants, such as cardiovascular and orthopeadic devices [77]. Bioresorbable Mg implants have many advantages in comparison to bioresorbable polymers. They are lightweight devices and they exhibit an elastic modulus and a compressive yield strength compatible

with those of natural bone. The Mg surface must however be covered to control its *in situ* degradation rate due to corrosion. M. Hasniyati *et al.* [17] coated Mg with HA using a CS process (Figure 1.20). The surface of Mg was ground using 240 or 2000 SiC paper grits. Also, before the deposition process, the substrate was heated up between 350 and 550 °C for 1 h. The stand-off distance (SoD) for CS was varied between 20 and 60 mm. The obtained HA coatings had a uniform topography and no phase change was observed. The best coating quality was obtained for a SoD of about 60 mm, a 240 SiC paper grit substrate initial roughening and a 500 °C substrate temperature. This coating had a thickness of 46 μm, a nano-hardness of 436,5 MPa and a 43,9 GPa elastic modulus.
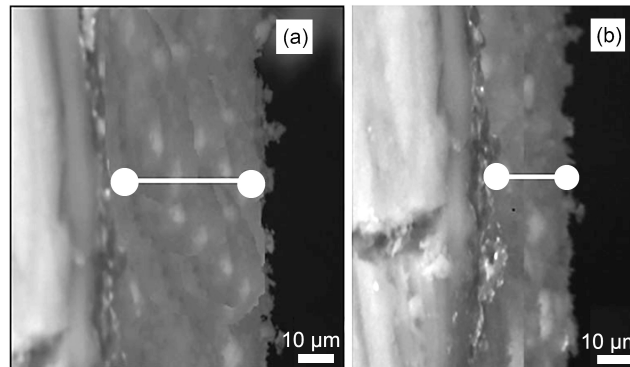
Figure 1.20 – *Cross-sectional SEM images of a HAP coating on Mg substrate sprayed at: (a) 60 mm SoD and (b) 20 mm SoD [17].*
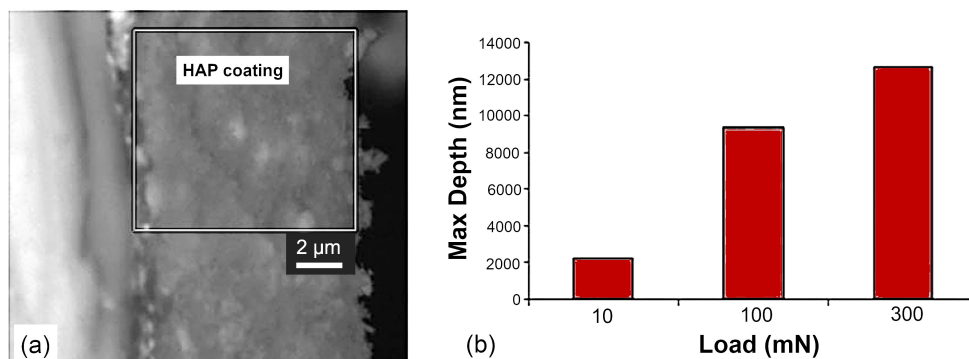
Figure 1.21 – *(a) Cross-sectional SEM image of a HAP coating on AZ51, and (b) maximum depth of penetration vs. different applied loads while measuring the hardness [18].*

A.C.W. Noorakma *et al.*[18] applied a High Pressure CS (HPCS) process to deposit HA on substrates made of AZ51 (5% Al, 1% Zn) magnesium alloy that were heated at 400°C prior to the deposition (Figure 1.21). They obtained coatings that had a thickness of 20-30 μm. The hardness of the HA coatings was uniform and had a value of 0.1 GPa for the minimum load of 10 mN, causing a penetration depth of the indenter of 2275 nm. At 300 mN, the penetration depth was 12460 nm corresponding to a hardness of 0,09 GPa. The authors underlined that the hardness slightly increased gradually towards the surface of the coating. The average of the elastic modulus of the coatings through its depth was 9 GPa, in the range of polymers and bellowed metallic lead. The biodegradation studies were conducted by immersing the HA coating in SBF solution to get the change in ion concentrations in comparison to a uncoated control sample. It was observed that the coating started dissolving after 1 day. Signs of regeneration were observed after 10 days. The Ca/P and Mg/Ca molar ratios were 1.514

and 0.535 at the beginning of the experiment and 0.956, and 37.6, respectively, after 14 days. The uncoated control sample showed degradation from the beginning of the experiment. The dissolution and re-precipitation of the apatite pointed out that the HA coatings had a good biodegradability and bioactivity on the Mg alloy.

Titanium and its alloys have also been widely used for orthopeadic and dental applications. Their biocompatibility was improved when their surface was covered with bioactive ceramic coatings, such as HA [78],[31], carbonated biomimetic nanocrystalline apatite (BNAc)[79], or a direct mixture of HA with an antibiotic, bioglasses containing SiO_2, CaO and P_2O_5 as main ingredients, and crystallized bioglasses [80].

In an ABAQUS/Explicit computational model, L, Zhang *et al.* studied the behaviour of HA particles at the impact on a Ti substrate in the CS process [81]. The authors analyzed the effect of the impact pressure, considering the size of particles and their velocity, as well as the substrate temperature. While increasing the gas pressure from 0.2 MPa to 0.6 MPa, the particles velocity increased from 150 $m \cdot s^{-1}$ to 360 $m \cdot s^{-1}$, whereas, with a significant decrease of HA particles size until a minimum of 5 μm, the particles velocity decelerated steeply. The use of agglomerated nanocrystalline HA powders was then a better option to obtain coatings promoting bio-integration .

A.M. Vilardell *et al.*[19] published a very recent research paper about the comparison of *in-vitro* tests of HA coatings on a Ti6Al4V alloy. The coatings were obtained using several thermal spray technologies: APS, HVOF and CS (Figure 1.22).
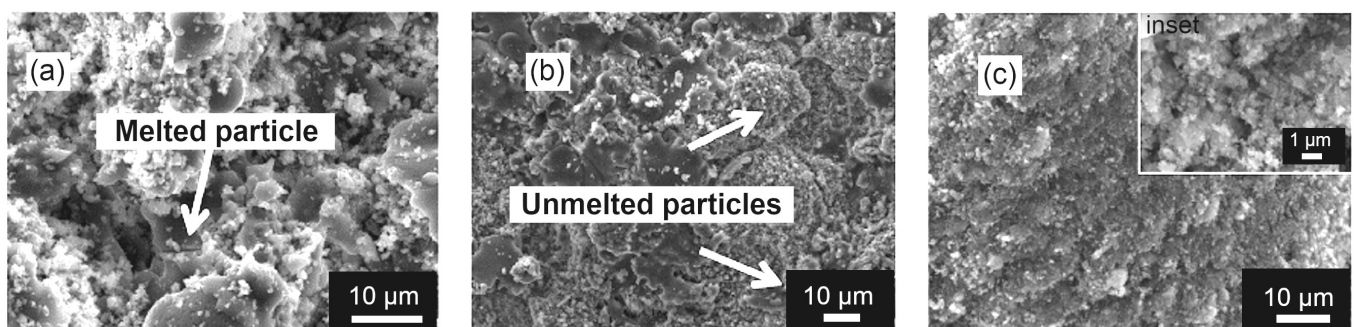
Figure 1.22 – *Top view SEM images of HA coatings obtained by: (a) APS, (b) HVOF and (c) CS [19].*

These tests were performed with primary human osteoblasts at 1, 7 and 14 days of cell culture. When decreasing the operating temperature of the thermal spray techniques (APS > HVOF > CS), the HA coatings revealed an increase of HA crystallinity from 62,4% to 89%, and higher hydrophilicity from -32° to 0°. Higher cell proliferation and differentiation were identified on HA coatings with higher crystallinity (*i.e.* obtained by HVOF and CS) after 14 days of cell culture. For coatings made by CS, the cell attachment was dependent on the surface micro-features, HA crystallinity and crystal size.

A.M. Vilardell *et al.*[11] also compared the fabrication of bioceramic coatings by LPCS and HPCS. They demonstrated that the feeding rate observed in the LPCS process was more constant as compared to the one observed at high pressure. The authors used a nanocrystalline microstructured HA powder with a specific morphology that led to the effective build-up of the coating. The substrate roughness was increased to help anchoring the first particles layer. Then, the coating was build-up as a result of the compaction mechanism, attributed to the tamping effect due to the constant impact of newly formed particles layers onto the ones already formed below. In order to activate diffusion mechanisms and improve the chemical bonding, the authors performed additional thermal post-treatments.

1.3   Conclusion - Chapter 1

In this chapter, a short description of the different thermal spray technologies is presented along with the schematic representation of each particular case. As already mentioned before, hydroxyapatite coatings are mostly elaborated by plasma spraying, but to overcome the drawbacks of such a technology (*e.g.* high thermal input which can cause thermal degradation and questionable long therm adhesion) CS is seen as an alternative since it uses kinetic energy instead of thermal energy for the consolidation.

The literature available on ceramic coatings fabricated by CS is very limited when compared to metallic coatings. Contrary to metals, ceramics rather fragment at the impact than undertake plastic deformation, which makes the deposition of ceramics by CS challenging. In order to overcome the lack of plasticity of ceramics, some researchers then apply "artifices" such as the use of soft substrates (*e.g.* PEEK, Mg), the adding of salts in the feedstock, the increase of the roughness of the substrate in order to promote the mechanical adhesion, just to name a few.

Since CS is a solid-state process, we must pay a particular attention to the feedstock and substrate characteristics (hardness, surface roughness, etc.) further described in chapter 2.

Chapter 2 : Materials, processing and characterizations

Overview ————————————————————————————————

This chapter 2 introduces the HAp-based feedstock materials we used to perform the CS experiments. For CS, and especially for CS of ceramics, the feedstock powders have to be carefully adapted in terms of size and morphology because these 2 parameters have a great influence on the in-flight velocity, as well as on the ability to get the desired fragmentation at the impact onto the substrate. Thus, we prepared different sizes of HAp powdered granules by spray-drying. The advantage of using spray-drying for granulation prior to deposition was also to overcome the safety issues and low flowability of elementary nanopowders. Before CS, some of those powdered granules were subjected to a preliminary thermal treatment of partial consolidation to adjust their mechanical response and further fragmentation ability. We also prepared polymer/ceramic (*i.e.* collagen-HAP) hybrid granules to improve the bio-activity of the as-obtained coatings. Finally, when looking at the final bio-application , we studied the possibility to functionalize the coatings with silver nanoparticles, deposited through Physical Vapor Deposition (PVD) on the feedstock powders prior to CS, to overcome potential antibiotic resistance issues.

Now dealing with the substrates based on Ti alloys, they were also adapted to CS in terms of surface preparation through laser texturing and through surface softening by titanium deposition. The idea behind was again the control of the fragmentation at the impact and mechanical anchor of the coatings.

2.1 Materials

2.1.1 TA6V substrates

Titanium and its alloys

Titanium and its alloys are widely used to manufacture implants because they fulfil the requirements for biomedical devices such as corrosion resistance, biocompatibility, bioadhesion (osseointegration), favourable mechanical properties (*i.e.* Young's Modulus close to that of the bone), good fatigue strength, and processability (casting, deformation, powder metallurgy, machinability, etc.) [82, 83, 20, 84, 85]. A significant advantage of titanium is the natural growth of an hydrated titanium oxide on its surface that can lead to direct bonding to the bone [86, 87].

Titanium (and the majority of titanium alloys) present two different crystallographic structures through an allotropic transformation occurring at about 880°C: i) an hexagonal close-packed (hcp) structure at low temperature called α-Ti (Figure.2.1) and ii) a body-centered cubic (bcc) structure at high temperature (Figure 2.1) named β-Ti [20].
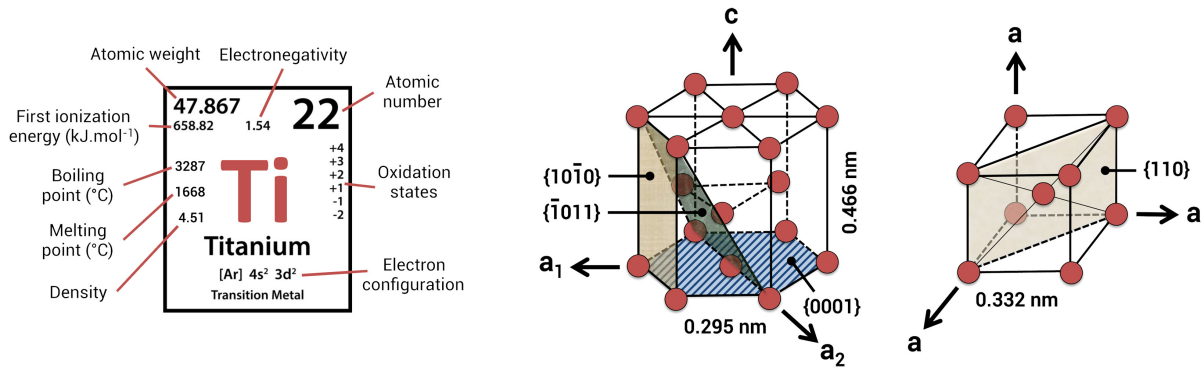
Figure 2.1 – *Ti element and its allotropic forms: hcp α (left) and bcc β (right)[20].*

The microstructure has a substantial influence on the properties of titanium alloys, which can be described by the size and arrangement of the α and β phases. More specifically, the way the material is processed (melting/solidification, hot forming/forging, etc.) controls the α/β ratio, the α grains having the specific shape of lamellae. A qualitative evaluation of the tendency as for the main properties of titanium and Ti alloys is reported in Table 2.1 as a function of the microstructure characterized by the grain size (fine or coarse) and morphology (lamellar or equiaxed) [21, 22].

Fine	Coarse	Property	Lamellar	Equiaxed
*	*	Elastic modulus	*	+/-
+	+	Strength	-	+
+	-	Ductility	-	+
-	+	Fracture toughness	+	-
+	-	Fatigue crack initiation	-	+
-	+	Fatigue crack propagation	+	-
+	-	Super-plasticity	-	+
+	-	Oxidation behaviour	+	-
-	+	Creep strength	+	-

Table 2.1 – *How the microstructure of α, $\alpha+\beta$, and β Ti alloys influences the properties [22].*

The Ti-6Al-4V alloy, generally abbreviated as TA6V, can actually contain up to 7% Al and 4.5% V. It corresponds to an $\alpha + \beta$ alloy and it is one of the most common titanium-based biomaterials used for implants [82, 83, 20, 86]. The addition of alloying elements to titanium provides a wide range of properties. Aluminium tends to stabilize the α-phase and vanadium tends to stabilize the β-phase, lowering the temperature of the transformation from α to β. Excellent strength characteristics and oxidation resistance are promoted by the α phase. Vanadium causes the higher strength of β phase and helps maintaining this phase below the transformation temperature, which results in a two-phase system as presented in Figure 2.2 [82, 22]. The main mechanical properties of different grades of commercially pure titanium (Ti CP) and TA6V titanium alloy are listed in the Table 2.2.

Properties	Grade 1	Grade 2	Grade 3	Grade 4	TA6V
Tensile strength [MPa]	240	345	450	550	860
Yield strength [MPa]	170	245	380	485	795
Elongation [%]	24	20	18	15	10

Table 2.2 – *Mechanical properties of Ti CP (ASTM F 67)[33] and TA6V (ASTM F 136)[34].*

The microstructure is affected by the cooling rate, influencing the mechanical behaviour of the titanium alloys. Figure 2.2 shows the ternary phase diagram of TA6V.
A slow cooling from the β phase-field gives lamellar microstructures as shown in Figure 2.3 a). When the cooling rate increases, it leads to a corser lamellar structure. On the contrary, a rapid quenching produces a martensitic transformation of the β phase providing a very fine needle-like microstructure (Figure 2.3 a)). In contrast with the martensitic structure identified in steels that leads to a strong distortion of the crystal lattice responsible for an increase of both the hardness and the mechanical strength, the hardening effect observed for titanium alloys upon martensitic transformation is only moderate [22, 21, 88].
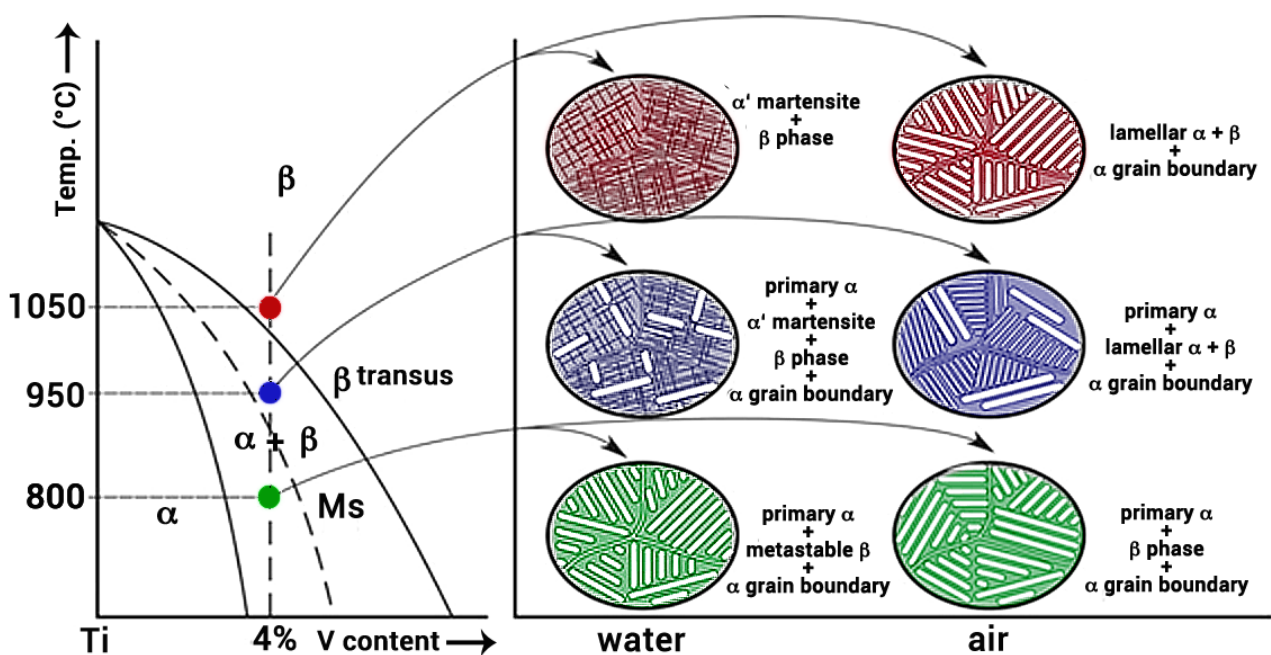
Figure 2.2 – *Schematic ternary phase diagram of TA6V alloy and representation of microstructures developed after solution treatment of casted TA6V alloy [21].*

The chemical compositions of the α and β phases change in a two-phase field when decreasing the temperature under the *liquidus* curve. Vanadium strongly enriches the β phase, thus stabilizing it at lower temperatures. The metallographic images of the microstructures of slowly cooled TA6V specimens show a small "seam" around coarse and light-coloured α lamellae (Figures 2.3 a), 2.3 c), 2.3 e)). With high cooling rates (*e.g.* after water quenching) from temperatures above the martensitic start (MS) temperature and through the two-phase field, the β phase transforms into martensite (Figure 2.3 d)). At lower temperatures, the β volume fraction further decreases and no longer transforms into martensite at temperatures below MS (Figure 2.3 f)) [22, 21, 88].
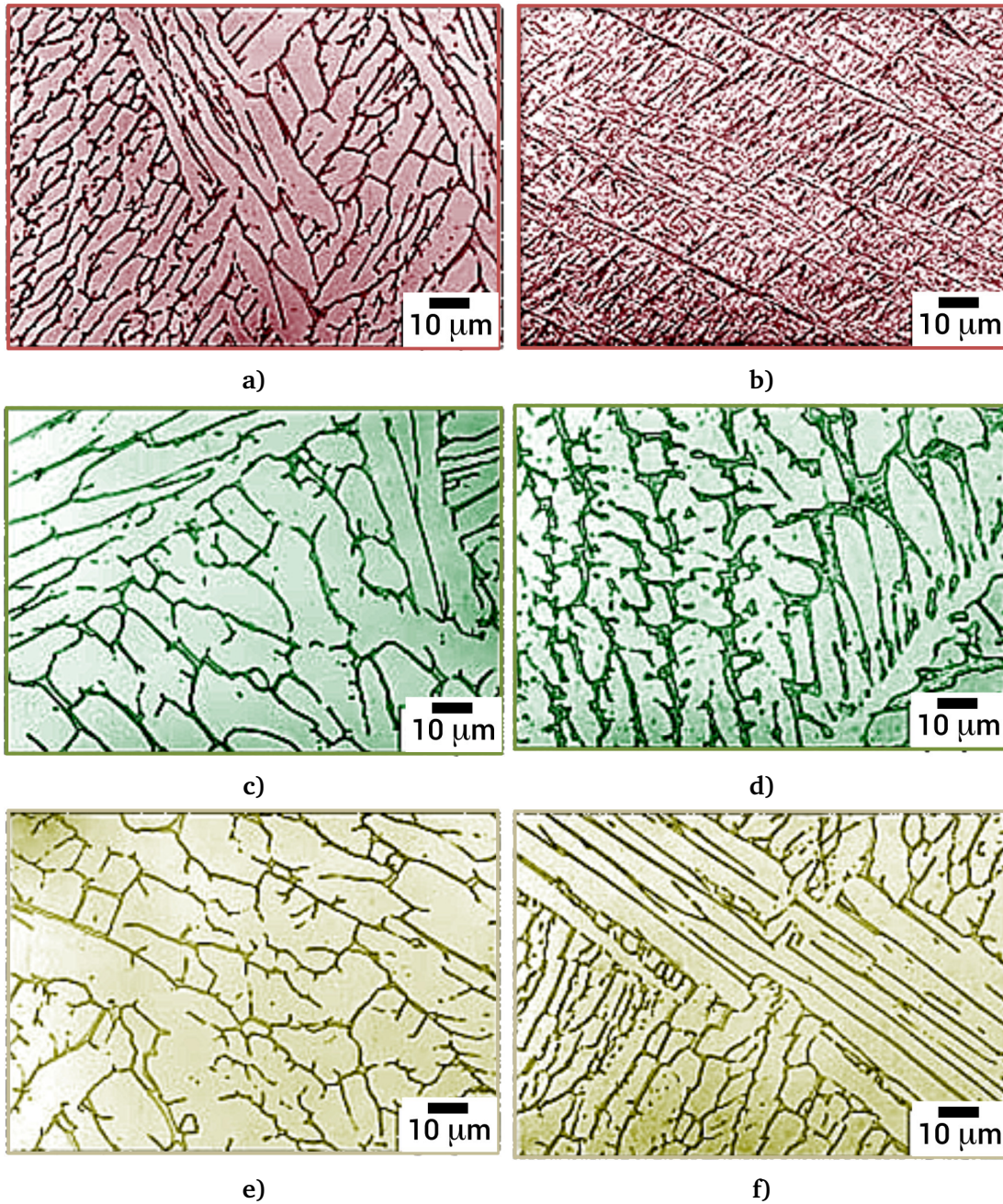
Figure 2.3 – Microstructures of TA6V alloy after a slow cooling rate (at 50°C/h in a furnace - images a,c,d) and after water quenching (images b,d,e), starting from 3 different temperatures (1050°C, 800°C and 650°C) [22].

2.1.2 Calcium phosphates

Calcium phosphates (CaPs, Figure 2.4) are the main mineral constituents of bone and teeth that contain calcium cations (Ca^{2+}) together with inorganic phosphate anions (PO_4^{3-})[35]. Since the 70's, CaPs were proposed for a broad range of Bone Tissue Engineering (BTE) applications, mostly as coatings on metallic substrates or as sintered bodies for synthetic bone graft substitutes. CaPs are known for their good biocompatibility, osseointegration and osteoconduction, being used in bone regeneration, such as orthopaedics and dentistry, and classified by their solubility and ability to degrade within the body. The calcium-to-phosphate (Ca/P) atomic ratios are between 0.5 and 2 with associated chemical formulae and solubility at 25°C given in Table 2.3.
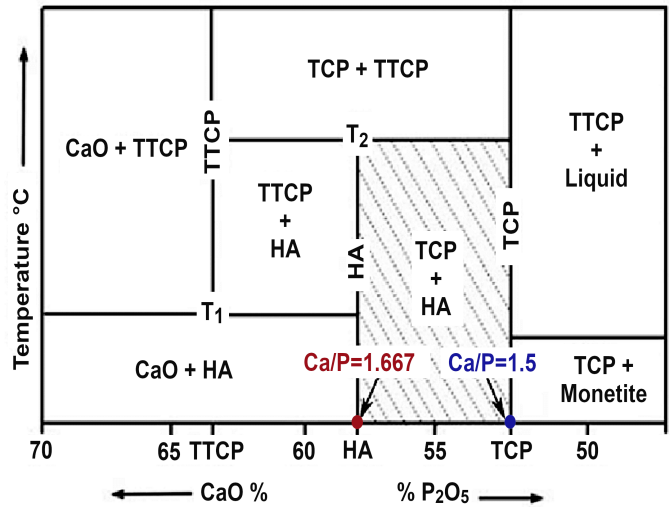
Figure 2.4 – *Phase equilibrium diagram of different calcium phosphates [23].*

Name	Chemical formula	Ca/P	Solubility [log K_{sp}]
Monocalcium phosphate monohydrate	$Ca(HPO_4)_2 \cdot 0H_2O$	0.5	Highly soluble
Monocalcium phosphate dihydrate	$Ca(H_2PO_4)2$	0.5	Highly soluble
Dicalcium phosphate dihydrate	$CaHPO_4 \cdot 2H_2O$	1	6.5
Octacalcium phosphate	$Ca_8H_2(PO_4)_6 \cdot 5H_2O$	1.33	96.6
α-tricalcium phosphate	$\alpha - Ca_3(PO_4)_2$	1.5	25.5
β-tricalcium phosphate	$\beta - Ca_3(PO_4)_2$	1.5	28.9
whitlockite (mineral)	$Ca_18(Mg,Fe)_2(Ca)(PO_4)_14$	1.36	
Hydroxyapatite	$Ca_5(PO_4)_3OH$	1.67	58.4
Fluorapatite	$Ca_5(PO_4)_3F$	1.67	60.5
Chlorapatite	$Ca_5(PO_4)_3Cl$		
Carbonated apatite	$Ca_10(PO_4)_6CO_3$		
Tetracalcium phosphate	$Ca_4(PO_4)_O$	2	

Table 2.3 – *Calcium phosphates classification, their Ca/P atomic ratios and solubility at 25°C [35].*

Hydroxyapatite

HAp is one of the most explored bioceramic due to its chemical composition similar to that of the mineral part of the bone. It has a chemical formula $Ca_5(PO_4)_3OH$, that is usually written as $Ca_{10}(PO_4)_6OH_2$ to underline the fact that the crystalline structure has two molecules. The mass percentages of Ca, P and OH are 39%, 18.5% and 3.38%, respectively [89, 90]. The general formula of the "apatite" compounds (not only of calcium phosphates) is in the form $M_{10}(XO_4)_6Z_2$, where M^{2+} is a metal and species XO_4^{3-} and Z^- are anions. In the case of stoichiometric HAp the molecular structure is formed by calcium (Ca^{2+}) as M, phosphorus (P^{5+}) as X, and hydroxyl radicals (OH^-) as Z. The atomic ratio Ca/P is 1.667 [90]. HAp presents two types of crystallographic structures (Figure 2.5): (1) hexagonal structure, space group P63/m, with lattice parameters a = b = 9.432 Å, c = 6.881 Å, and

(2) monoclinic structure with lattice parameters a = 9.421 Å, b = 2a, c = 6.881 Å, $\delta = 120°$.
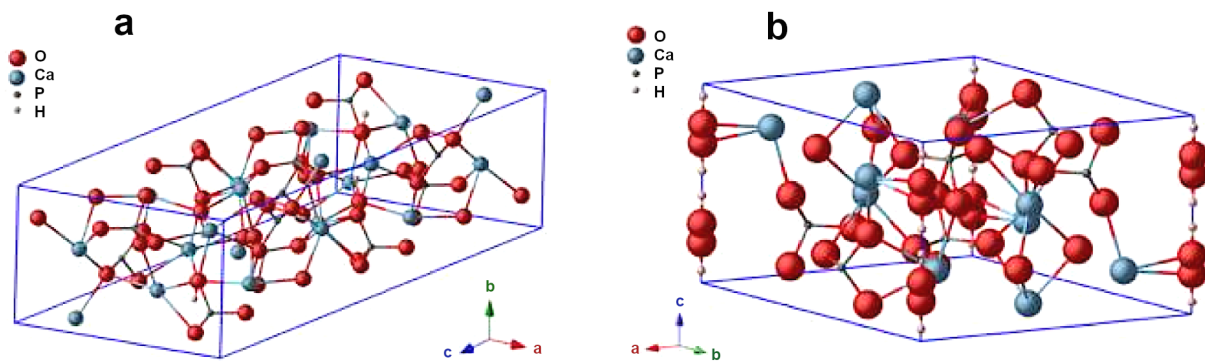
Figure 2.5 – *(a) Monoclinic and (b) hexagonal unit cell of HA [24].*

Synthesized at very high temperatures, monoclinic HAp is also expected to exist in hard tissues and it is the most stable structure from a thermodynamical point of view [24]. The HAp produced biologically has actually a more complex structure. For instance, it contains traces of CO_3, Mg, Na, F and Cl. It is also non stoichiometric with a Ca/P atomic ratio <1.67. The amount of traces can be different depending on the type of tissue and it can influence a lot the properties, especially the bioactivity. To obtain a better bioactivity, the Ca/P value must be lower than 1.67 (deficient HAp). At the opposite, a better stability of the HAP material inside the human body occurs when the Ca/P atomic ratio approaches 1.67. The crystallinity of HAp also influences its reactivity inside the human body. The crystallinity is very high for tooth enamel, but very poor for dentin and bone. As a consequence, the reactivity is greater in dentin and bone than in the tooth enamel [90]. HAp is capable of a strong chemical bonding with the host bone tissue. It exhibits bioactive, non-toxic, osteoconductive, non-immunogenic properties and it is considered as the most efficient graft synthetic bone material in the case of an adequate amount of carbonate substitution [91]. As it can be observed from Table 2.3, HAp is not highly soluble, but the surface of HAp coatings can provide nucleation sites for precipitation of apatite crystals in different culture media [92].

Hydroxyapatite feedstock characterization

Two commercially-available spray-dried HAp agglomerated powders from MEDICOAT SAS Company (France) with different crystallinity and intra-agglomerate porosity were used in this PhD work for the CS experiments and the understanding of the influence of the CS deposition parameters. We will now refer to them as: GA (green agglomerates) and SA (agglomerates sintered at 900°C). No more information on the exact production process of these agglomerates will be given in this manuscript for confidential reasons.

XRD patterns of GA and SA are shown in Figure 2.6 a). The GA powder exhibits broad peaks due to a low crystallinity and/or to a small size of the crystallites. These peaks can be attributed, according to JCPDS-9-0432, to synthetic HAp with an hexagonal lattice structure of the P63/m space group. In the case of the SA powder, it presents basically the same XRD pattern as GA but with very narrow peaks indicating a much higher degree of crystallinity, which is obviously due to the thermal treatment at 900°C. This higher degree of cristallinity is confirmed by Selected Area Electron Diffraction (SAED) analyses at the Transmission Electron Microscope (TEM), as shown in the insert at the top right corner of Figure 2.7 b).
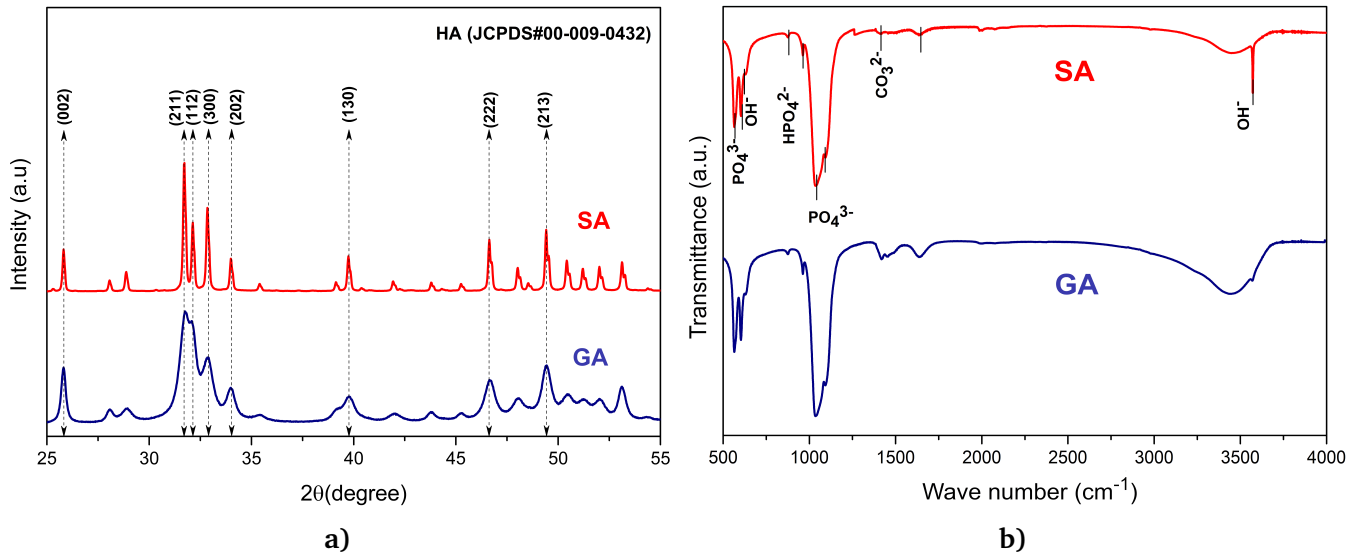
Figure 2.6 – *XRD and FTIR patterns of GA and SA HAp powders from MEDICOAT SAS (France).*

Concerning the FTIR analyses (Figure 2.6 b)), the characteristic peaks at 3558 and 667 cm^{-1} are due to the stretching and vibrational modes of the -OH groups of hydroxyapatite. The characteristic peaks of tetrahedral PO_4^{3-} are observed at 563, 603, 962 and 1033–1091 cm^{-1}. The 2 peaks at 563 and 603 cm^{-1} correspond to the PO_4^{3-} ν_4 mode. The peak at 962 cm^{-1} is for PO_4^{-3} ν_1 and the peaks at 1033–1091 cm^{-1} are due to PO_4^{3-} ν_3. The peaks at 1421 and 875 cm^{-1} result of the absorption of CO_2 molecules at the agglomerated particles surface.

The TEM images shown in Figure 2.7 a) reveal the presence of interlocked acicular (needle-like) nanoparticles for GA, whereas quasi-spherical nanoparticles of a much larger size are observed for SA (Figure 2.7 b)). It must also be noticed that, for SA, some solid necks are present at the triple points between the elementary grains due to the sintering at 900°C. The electron diffraction (SAED) highlights diffuse rings for GA and "spots" for SA, in line with the previous discussion about the crystallinity degree from the XRD results of Figure 2.6 a).

a) GA **b)** SA
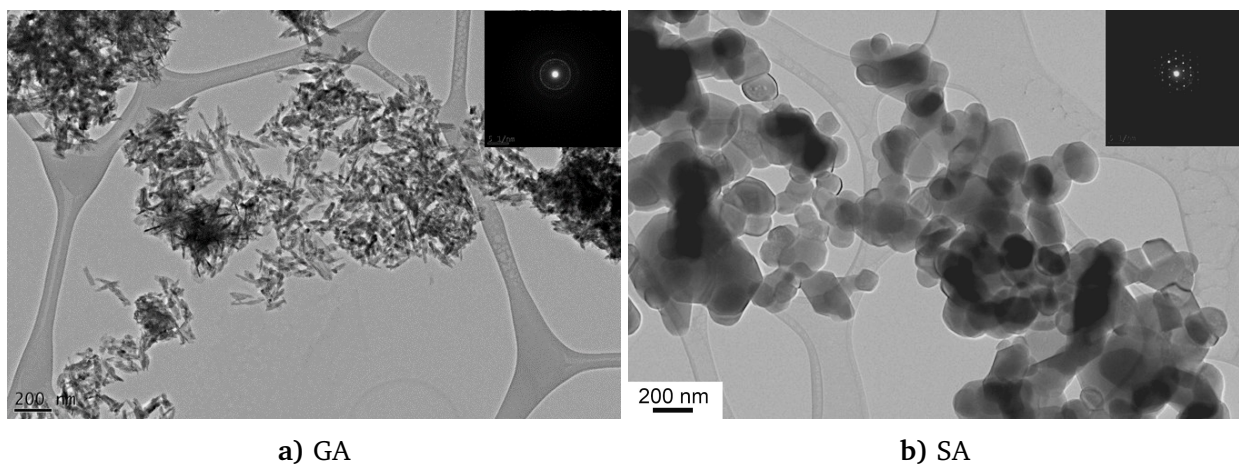
Figure 2.7 – *Bright Field TEM images of a) GA and b) SA HAp powders.*

The surface areas of GA and SA were measured by the Brauner-Emmett-Teller (BET) method, whereas their pore size and pore volume were determined by the Barrett-Joyner-Halenda (BJH) method. The measurement of the density of the solid part of the powders was performed by He pycnometry. The results are listed in Table 2.4.

The particles size distributions (measured by laser granulometry - Figure 2.8 e) and 2.8 f)) of the as-received GA and SA powders show that both powders are quite similar in terms of the average size of agglomerates. SA presents however a slightly narrower distribution with a $D_{10} \approx 31 \mu m$ and a $D_{90} \approx 64 \mu m$, compared to GA which exhibits a $D_{10} \approx 20 \mu m$ and $D_{90} \approx 65 \mu m$. The larger quantity of small agglomerates in GA in comparison to SA is evidenced when looking at low magnification SEM images (Figures 2.8 a) and 2.8 b)). At higher magnification, SEM images show also clearly the needle-like morphology of the elementary grains inside the GA agglomerates (Figure 2.8 c)), while for SA a morphological evolution and a grain coarsening due to the thermal treatment at 900°C is seen (Figure 2.8 d)). Concomitantly to these morphological change and coarsening, a decrease of the specific surface, of the pore size and of the pore volume, together with an increase of the density are logically registered (Table 2.4).
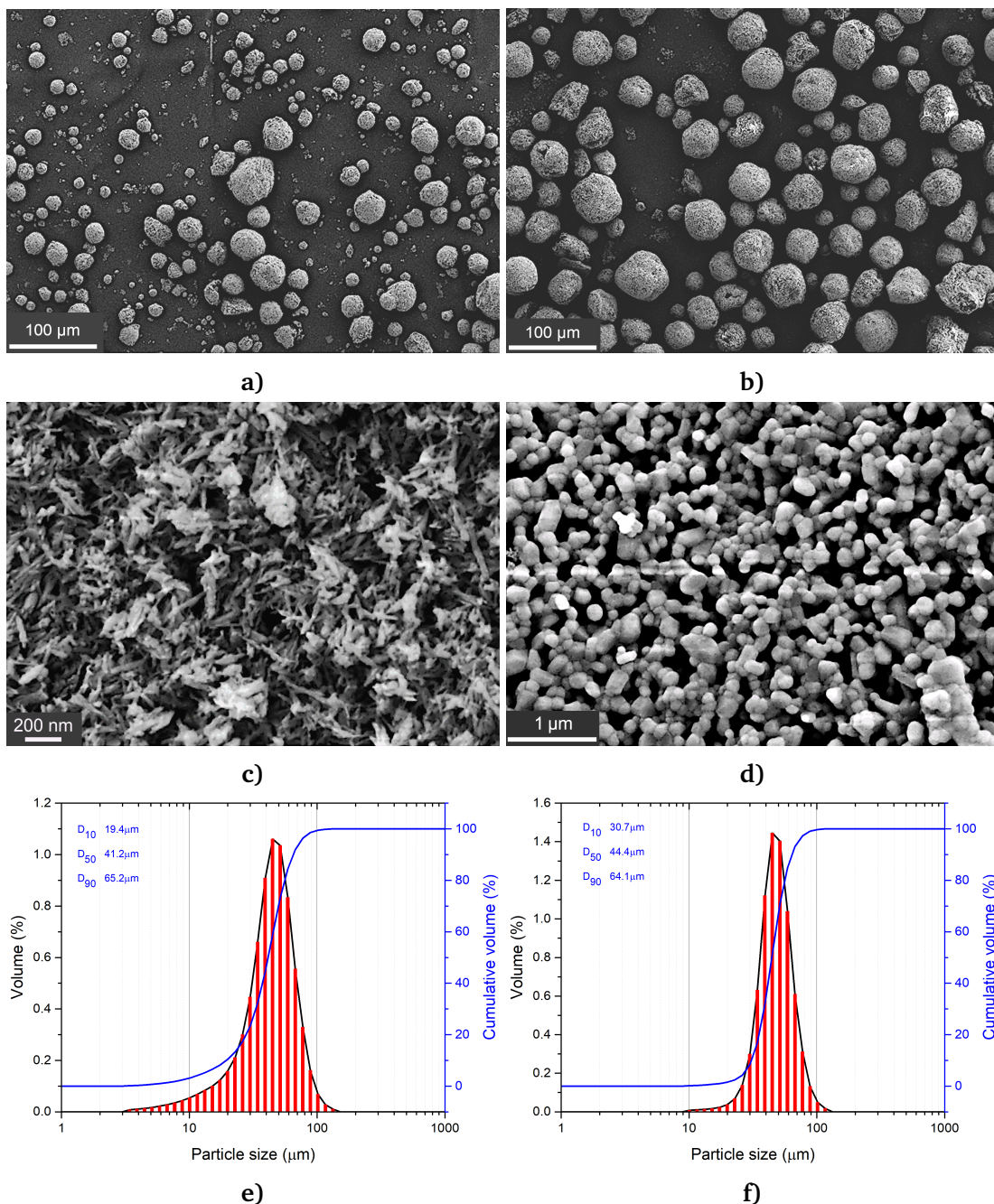
Figure 2.8 – *GA: SEM images (a,c) and particles size distribution (e) ; SA: SEM images (b,d) and particles size distribution (f).*

Sample ID	Density [g·cm⁻³]	Specific surface [m²·g⁻¹]	Pore size [nm]	Pore Volume [cm³·g⁻¹]
GA	2.81	89.3	22.8	0.485
SA	3.11	5.5	11.9	0.016

Table 2.4 – *Physical properties of GA and SA powders.*

TG-DTA analyses of GA and SA are presented in Figure 2.9. GA (Figure 2.9 a) exhibits a mass loss of about 6.5% over the temperature range which goes up to 1000°C in air. This progressive mass loss occurs in two successive stages with an inflexion point observed at about 550°C. Below 550°C, the mass loss most likely corresponds to the elimination of the physisorbed and chemically-bonded water. Above 550°C, the possibility of a release of nitrates residues cannot be excluded. These residues come actually from the HAp synthesis process upstream. On the contrary, the mass loss for SA (Figure 2.9 b) is limited to less than 1%. In this case, it can be attributed to the elimination of the physisorbed water and of the CO_2 adsorbed on the powder surface. In both cases, for GA and SA, the observed small peaks around 900°C in the DTA signals are assumed to be linked to the phase transformation into TCP.
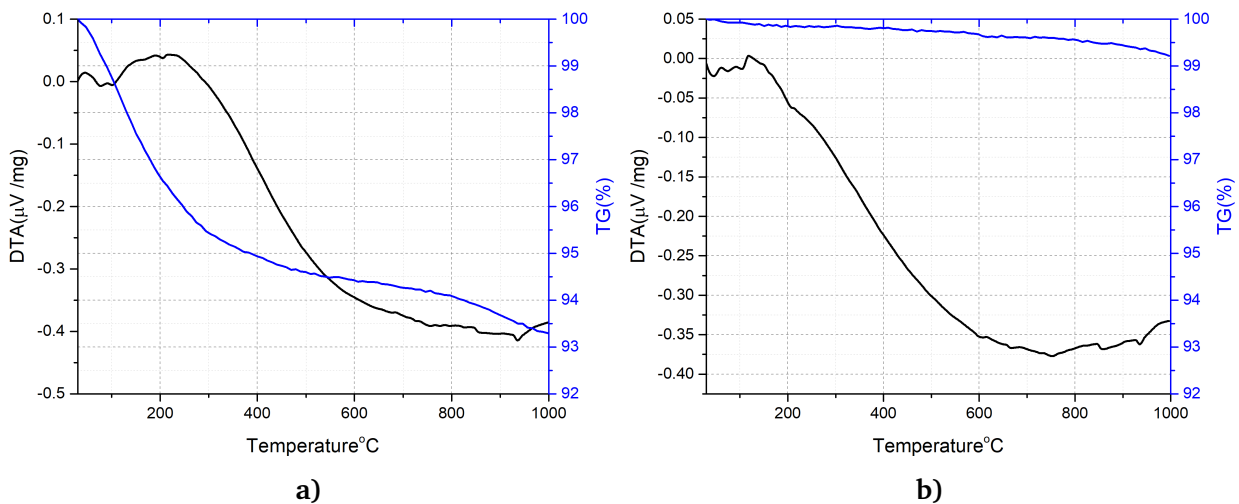
Figure 2.9 – *TG-DTA analyses of a) GA and b) SA powders.*

2.1.3 Type I Collagen

Bone is considered to be a 3D complex composite material consisting of fibrous type I collagen (COLL) scaffold onto which small crystals of carbonated hydroxyapatite are deposited. Then, synthetic collagen-hydroxyapatite-based biomaterials appear as promising candidates for BTE [93, 94]. Collagen is actually the major protein in bone (about 80 wt.%), skin, tendons, ligaments, cornea and blood vessels. Type I collagen comprises approximately 95% of the entire collagen content of bone. Types II, V and XII are also present in bone [93, 95, 96].

Compared to other types of collagen, the type I exhibits outstanding mechanical properties and it is intrinsically contained in extracellular tissues providing mechanical functions. The fact that the collagen molecules are cross-linked in the extracellular matrix helps developing the 3D scaffold necessary for the deposition of mineral crystals as previously mentioned. Type I collagen is an heterotrimer molecule assembly in the form of a triple helix as shown in Figure 2.10.

In most of the cases, it is formed by two $\alpha1$ chains and one $\alpha2$ chain, although an $\alpha1$ homotrimer exists as a minor form. The chains consist in more than 1000 amino acids. The length of a collagen type I molecule is $\approx$ 300 nm and the width is about 1–5 nm. It has three domains: an N-terminal non–triple-helical domain (N-telopeptide), a central triple-helical domain, and a C-terminal non–triple-helical domain (C-telopeptide) [96, 97, 98]. The triple helical domain is only possible due to the presence of glycine (G)-X-Y repeats, where X is often a proline and Y is a hydroxyproline. Glycine at every third position is essential for the correct formation of the structure. Hydroxyproline is also characteristic of collagen offering stability through intramolecular hydrogen bonds [96, 97, 98].
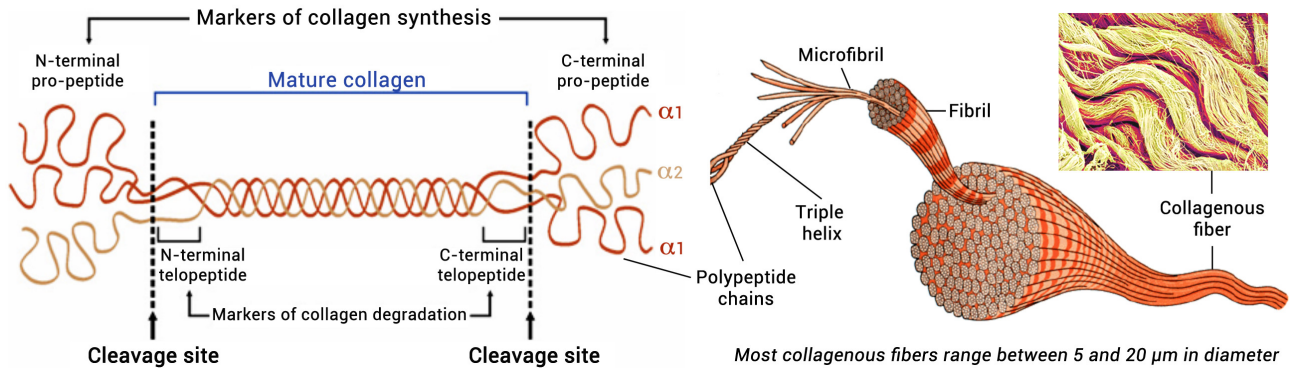
Figure 2.10 – *Structure of collagen molecules.*

In this PhD research work, Type I fibrillar collagen was extracted in the form of a gelatin (Figure 2.11) from calf hide by the technology currently used at the Leather and Footwear Research Institute, Collagen Department, Bucharest, Romania (actually, the extraction work was done in direct collaboration with that institute using its facilities - we thank Romanian colleagues for that). The method is described in details in a paper published by Albu *et al.* [96].
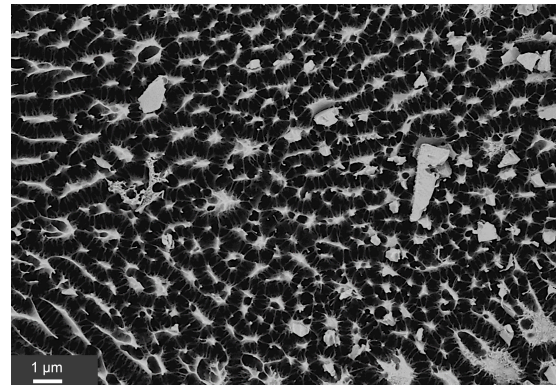
Figure 2.11 – *SEM image of collagen gelatin.*

2.1.4 Bioglass

For a long time, HAp was considered as the best possible coating for biocompatible implants, till L. Hench developed a reactive material, 45S5 bioglass (Bioglass), that could bond to mineralized bone tissue in a physiological environment. This bioglass is a silica-based material as host material (45 wt.%), in which calcium oxide (24.5 wt.%), sodium oxide (24.5 wt.%) and phosphorous oxide (6.0 wt.%) are incorporated. It can form strong bonds with the bone and soft tissues preventing the body from inflammatory response. In the ternary diagram given Figure 2.12, Hench *et al.* emphasized that relatively small changes in the bioglass composition could lead to a wide range of properties: resorbable, bioactive or bioinert material. Due to its biocompatibility, osteoproductive, osteoconductive and osteoinductive properties, it is known as "bioactive glass-bioglass". The bond between the implant and the surrounding tissue, acknowledged as the level of the bioactivity, is measured by the index, IB = 100/t0.5bb, where "t0.5bb" is the duration necessary to achieve at least 50% of the coating to bond

to the bone. The A region is represented by the bioactive glasses that have a constant 6 wt.% P_2O_5 and bond to soft tissues and bone, inside the central dashed line, where IB > 8 (45S5 Bioglass, Ceravital®). Apatite/wollastonite (A/W) glasses have higher P_2O_5 contents. The B region is represented by nearly bioinert glasses. Bioresorbable glasses are presented in the C region. The D region corresponds to non-glass-forming compositions [25].

The 45S5 bioglass reacts with the surrounding physiological fluid to generate the formation of an hydroxyl carbonated apatite (HCA) layer at the materials surface and allows for a strong interaction and bond with the bone. This quality of the HCA layer is due to its composition similar to that of the hydroxyapatite. The 45S5 bioglass was first used as a medical device in 1984, to help restoring the hearing of a deaf patient who had two out of the three bones in his middle ear degraded [99]. The osteogenesis and bioactivity of the bioactive glass

Figure 2.12 – *Phase diagram of bioactive glasses and composition dependence as for the bonding with bone and soft tissues [25].*

depend on the HCA layer formation and reaction rate at the glass/bone interface. This 45S5 bioglass was initially produced by a melt-derived process with a maximum SiO_2 content of 60 mol.%. In a second step, other bioactive glass powders in the ternary system $CaO-P_2O_5-SiO_2$ were produced using sol-gel methods allowing for an increase of the bioactivity and resorbability rate in comparison to the standard melt-derived 45S5 bioglass. These characteristics are due to the greater specific surface area achieved, resulting from a nanometer-size textural porosity [100]. In addition, since Na_2O is not a critical component in the bioactive glass composition, by utilizing the sol-gel techniques, the SiO_2 content range can be expanded from 60 mol.% to 85 mol.% [101].

Figure 2.13 – *SCHOTT Vitryxx® bioglass powder.*

A disadvantage that bioactive glasses possess in a porous form is their low fracture toughness (and consequently poor mechanical behaviour) which gives rise to limited applications in load-bearing situations [102]. The mechanical properties can be improved by a heat treatment of partial re-crystallisation usually at about 870-900°C [103] (*e.g.* development of A/W bioglasses like Ceravital® and Bioverit®). The partially crystallised microstructure increases the crack growth resistance [104]. A even higher bending strength and fracture toughness can be obtained while developing β-wollastonite

($CaSiO_3$) as reinforcement in apatite phases, making of these tailored bioglasses better candidates for load-bearing applications [104, 105].

In this PhD, a commercially available bioglass powder (Vitryxx®, Schott AG, Germany - Figure 2.13) was used to develop hybrid bioglass-hydroxyapatite agglomerates. Its composition in wt.% is 24.5 CaO / 6.0 P_2O_5 / 45.0 SiO_2 / 24.5 Na_2O, with a granulometry from a few microns to 25 μm.

2.2 Processing

2.2.1 Powder granulation by spray drying

Nanohydroxyapatite (n-HAp) presents some advantages in comparison to conventional micrometer-size HAp with regards to the promotion of osteoblast adhesion, proliferation, and osseointegration [106]. However, the main drawbacks concern the safety manipulation [107] and flowability of powder, which is a crucial factor when it comes to CS. In the aim to overcome the low flowability issue of nanoparticles and submicron particles, spray-drying can be an effective method [108, 109].

The spray-drying process is presented in Figure 2.14. It is a process that transforms a suspension or an emulsion into dried agglomerates formed by spraying the feed into a hot drying environment (air or inert gas such as argon or nitrogen) [109, 110, 94]. It is basically a granulation process.
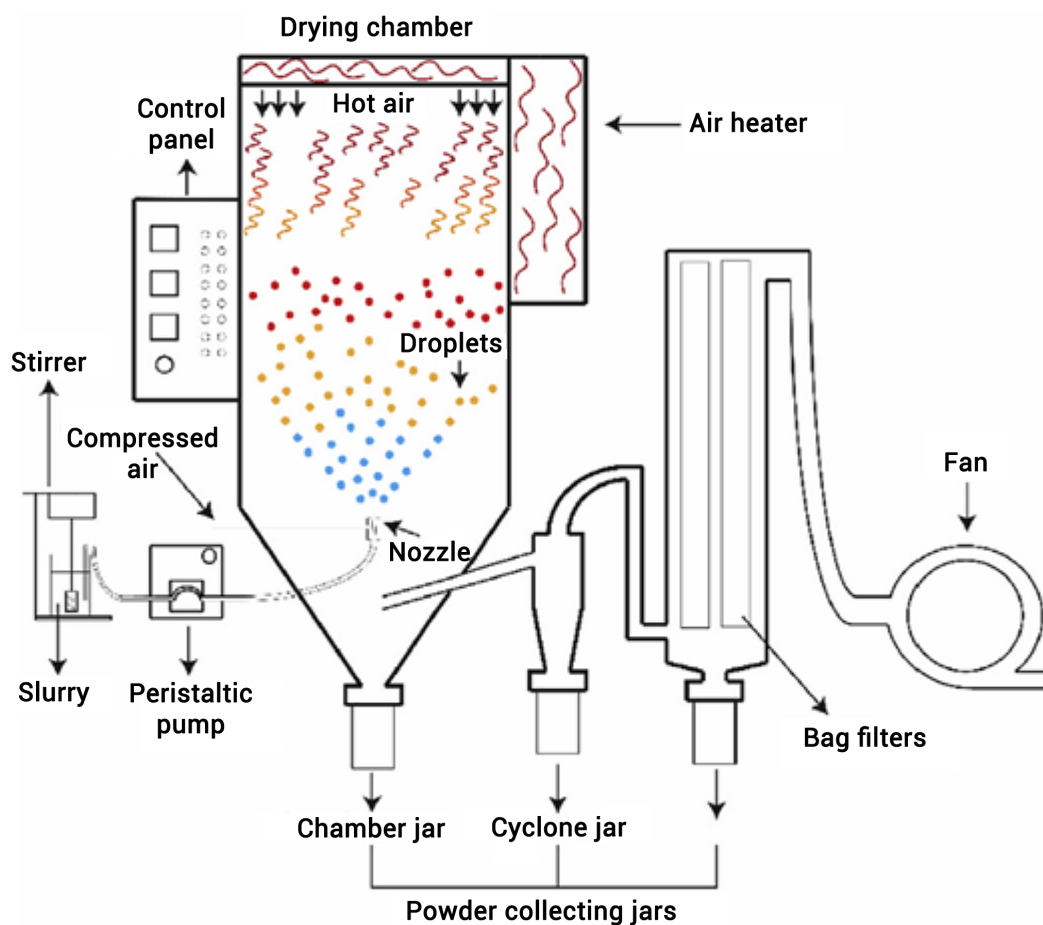
Figure 2.14 – *Schematic representation of a spray-dryer [26].*

There are lots of benefits of the spray-drying technique including the ability to produce agglomerates of a specific size, while maintaining the elementary particles size [110, 111, 112]. Moreover, spray-drying represents an excellent way to improve the physico-chemical stability of polymers [113, 111]. Another advantage is the ability to obtain hybrid powders such as polymer/ceramic, metal/ceramic, etc., with a considerable possibility to customize them depending on individual needs [94]. The spray-drying process is generally influenced by several parameters such as: feed formulation, feed rate, inlet air temperature, drying air velocity and atomizer specifications [26, 110, 112].

Spray-drying process mechanism

The spray-drying mechanism is based on the moisture evaporation of the feed in the drying environment. The spray-drying process can be described straightforwardly in three steps [114]:

- atomization

- droplet-to-powder conversion

- powder collection

Atomization: In this first step, a suspension of elementary particles in a solvent (usually water plus eventually some additives like a dispersing agent, a binder and a plasticizer) is supplied to an atomizer, disintegrating the liquid feed into fine droplets. The atomization process can be carried out in different ways such as pressurized, electrostatic or centrifugal ones. The heat and mass transfers are maximized due to the high specific surface area of the droplets. The typical dimension of formed droplets is closely related to the energy provided. For the same amount of energy, the size of the formed droplets increases with a higher feed rate. The size of droplets also increases when both the viscosity and surface tension of the initial liquid are high.

Droplet-to-powder conversion: After atomization, the spray-drying mechanism proceeds with the granulated powder formation phase marked by two events: droplet – hot air contact and droplet drying (*i.e.* moisture evaporation).

<u>Droplet – hot air contact</u> : In this step, atomized droplets are exposed to a hot gas (air, nitrogen, argon) inside the drying chamber, resulting in preliminary moisture evaporation. Mostly due to economic aspects, atmospheric air is usually used as the drying gas, although in some particular cases it is necessary to use an inert gas to avoid potential instabilities between the gas and the aerosol droplets. There are many types of atomizers on the market allowing to obtain a wide range of granulated powder granulometries (Figure 2.16). For instance, among the most conventional atomizers, there are three different drying chamber configurations, in which the flow direction between the hot gas and the droplets are manifesting their dynamics: co-current flow, counter-current flow and mixed configuration as shown in Figure 2.15.
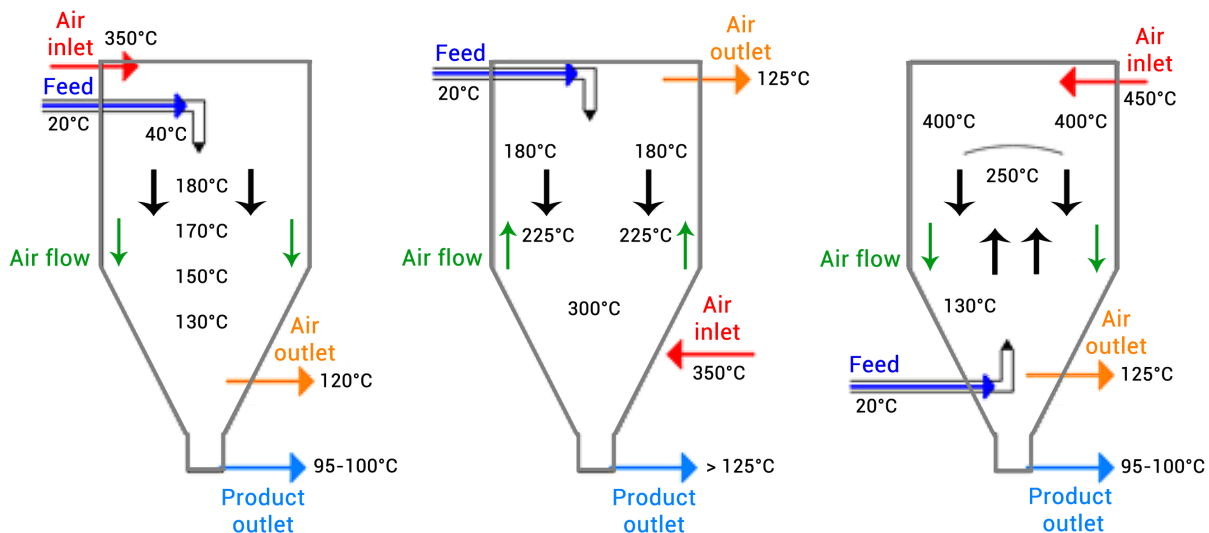
Figure 2.15 – *Air-droplet flow configurations within the atomizer chamber, adapted from [26]*

In the co-current configuration, the atomized droplets and the heated gas are supplied through the drying chamber in the same direction. The dried heavy particles are dropped by gravity at the bottom of the chamber, where they can be collected. Due to the short residence time, the drying gas does not exchange the heat with the surroundings, and consequently, the atomized droplets meet the highest temperatures inside the drying chamber. This configuration implies a high rate of solvent evaporation in a short time, which avoids undesirable thermal degradation.

In the counter-current configuration, the atomized droplets and hot gas are flowing in opposite directions, the atomizer being situated at the top of the chamber and the hot gas being introduced from the bottom. This flow configuration is considered to be the most efficient configuration since the hot gas reduces the velocity of the falling atomized droplets, resulting in an increased of their residence time inside the chamber. Contrary to the co-current flow, the hot gas starts to release a part of its heat to the surroundings. A drawback of the counter-current configuration is that it is limited to heat resistant materials since, at the beginning, the droplets are in contact with the gas at the the top of the chamber, so at a lower temperature. However, towards the end of this process, the dried particles reach higher temperatures due to the hot gas coming from the bottom of the chamber.

The mixed configuration combines both co-current and counter-current flows, where the atomized droplets are supplied from the bottom of the drying chamber in counter-current to the drying gas which is flowing from the top. In this case, both the dried particles and the drying gas are discharged at the bottom of the chamber. As long as the residence time of droplets inside the chamber is maximized, this configuration is more adapted in the case of coarse droplets, without any prominent effect of the size of the chamber itself. Like the counter-current configuration, this method is limited to heat resistant materials.

Figure 2.16 – *Particle size distributions for different atomization systems under comparable conditions.*

Droplet drying - moisture evaporation: As it was described above, when the aerosol droplets are in contact with the drying medium within the chamber, the solvent starts to evaporate. After the liquid-solid phase equilibrium is established due to the vapour pressure, the water transfer starts to occur in the opposite direction. The drying kinetics then comprises several steps with different durations (usually, drying times are of the order of 5–100 s).

The granule shape is strongly influenced by the spray-drying conditions and droplets properties such as their viscosity, surface tension etc. In order to obtain the desired granule size and morphology, the evaporation kinetics must be controlled. The drying process starts on the surface and propagates to the core. Thus, during the drying, the droplets form a "core-shell" structure, the surface (shell) being "dry", whereas the core remains wet for some time (Figure 2.17 a)). In the case of small droplets, the moisture vaporization is completed almost instantly, resulting in spherical particles suitable for a good flowability. In contrast, for big droplets, the solvent remaining at the core may generate, while evaporating, an increased internal pressure that can fracture the already formed "dry" shell (Figure 2.17 b)).

Figure 2.17 – *Effect of drying kinetics on the granulated powder formation during atomization.*

Powder collection: After the droplets are transformed into granules, it is necessary to collect the spray-dried powder. There are two ways to recover the dry product: most dense granules are recovered at the base of the drying chamber, while the finest granules are separated through a cyclone placed outside the dryer. Depending on the processing parameters, the obtained powder can exihbit different morphologies, porosities and sizes, but most of the time, the desired shape is the spherical one. All of these steps play a significant role in the yield and agglomerates properties.

Procedure used in this work to produce hybrid granules containing bioglass or collagen
Four different slurries were prepared using planetary milling. Their formulations are listed in Table 2.5. They contained from 5 to 10 wt.% of bioglass or collagen with respect to the HAp GA content. Each of the blends was introduced at 40 % (w/w) in distilled water together with 1.1 % (w/w) of dispersing agent (Darvan C-N, R. T. Vanderbilt Company Inc., USA) with respect to the overall mass. The mix was then milled for 24h at 45 rpm in an alumina jar with 3 alumina balls dimensions of 10-19-25mm (Ceradel, France). The obtained slurries were then fed into the spray dryer nozzle to form aerosol droplets that were dried in an air gas flow of 20 $m^3.h^{-1}$ at 190°C (inlet temperature). Finally, the dry granules were sieved and the fraction between 15 μm and 63 μm was collected for further CS deposition. The SEM images (Figures 2.18 a), 2.18 b), 2.19 a) and 2.19 b)) of the granules show rather spherical shapes with quite broad size distributions in the 10-40 μm range. Although the granules containing collagen appeared to be a bit smaller than those with bioglass, in both cases they were fulfilling the requirements for CS. The TG-DTA analyses (Figures 2.20 a) and 2.20 b)) of the granules containing collagen pointed out a mass loss slightly lower than expected, suggesting that collagen was effectively introduced but at 3-4 % and 6-8 % rather than the 5 and 10 % initially targeted (to be compared with the mass loss of pure HAp GA which was around 6 % - Figure 2.9 a)).

Sample name	Powder[40% w/w]	Dispersant [% w/w]	Water [% w/w]
Coll5@HA	95HA+5Collagen		
Coll10@HA	90HA+10Collagen	1.1	58.9
HA@BG5	95HA+5Bioglass		
HA@BG10	90HA+10Bioglass		

Table 2.5 – *Slurry formulation for spray drying of hybrid granules.*
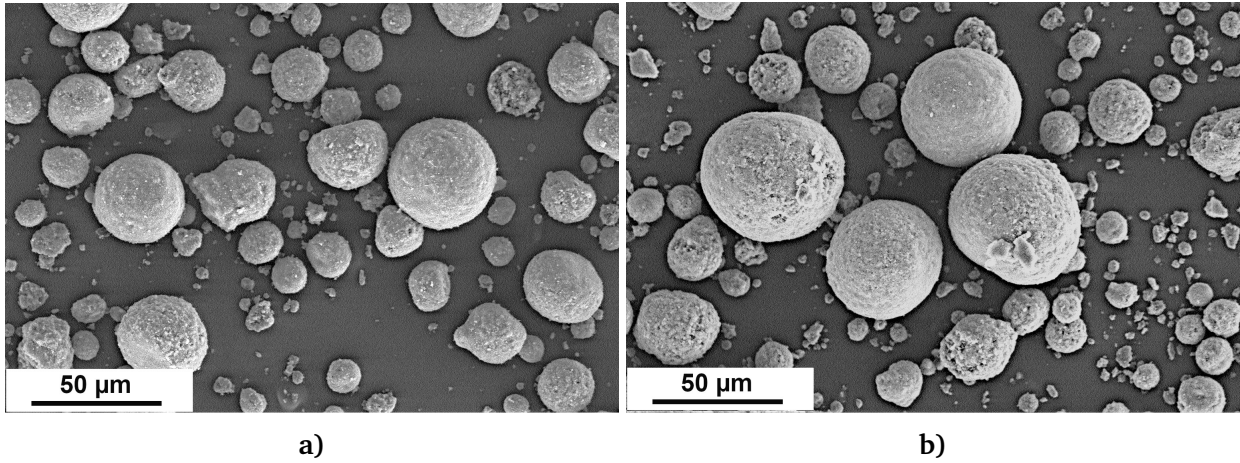
Figure 2.18 – *SEM images of spray-dried granules: a) BG5@HA and b) BG10@HA.*
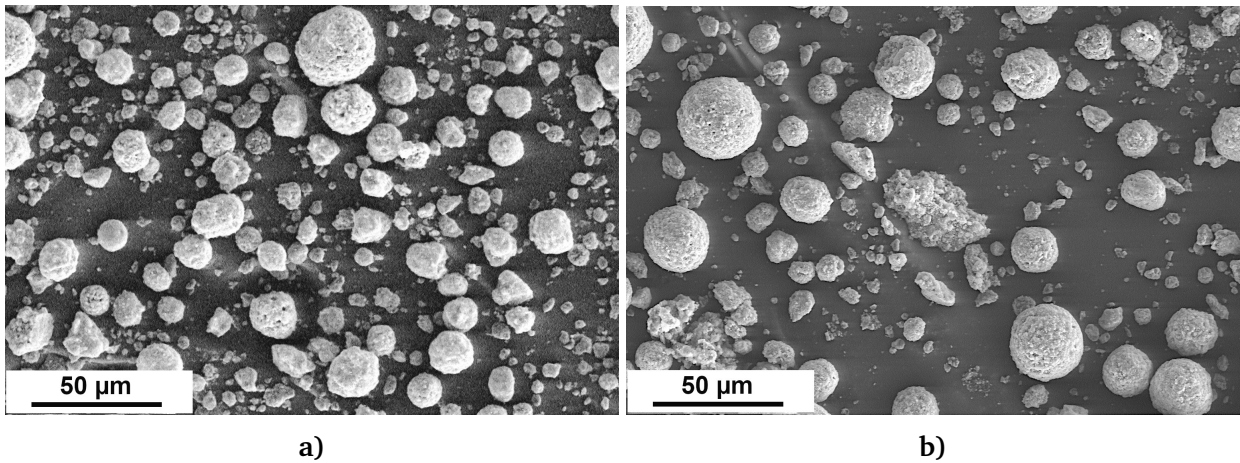
Figure 2.19 – *SEM images of spray-dried granules: a) Coll5@HA and b) Coll10@HA.*
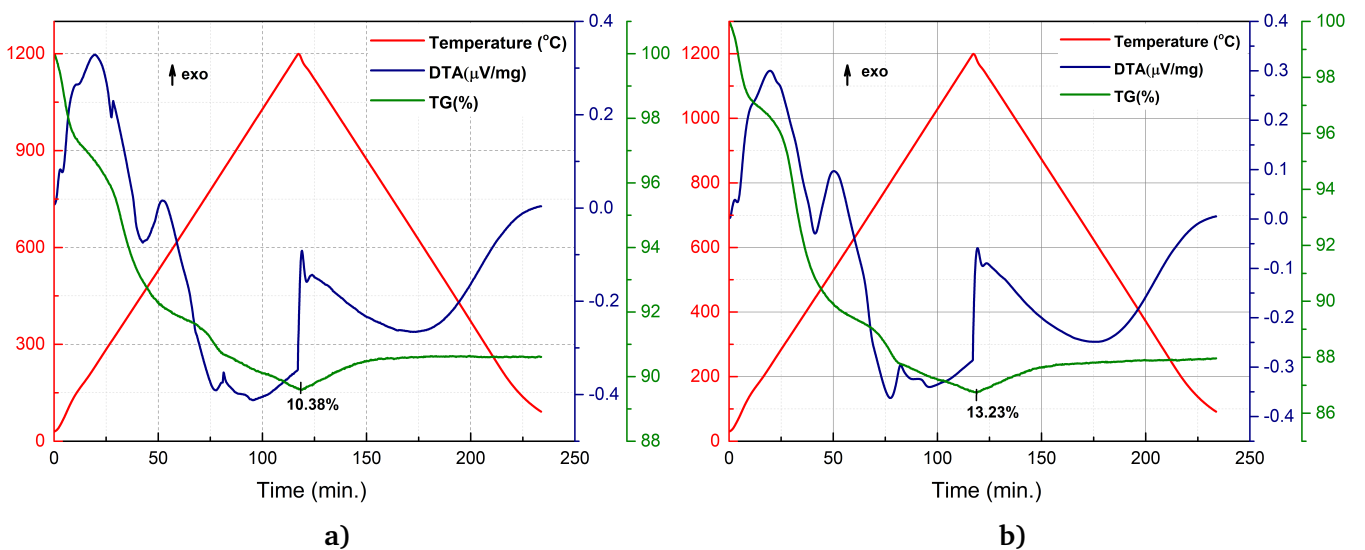
Figure 2.20 – *TG-DTA analyses of spray-dried granules: a) Coll5@HA and b) Coll10@HA.*

2.2.2 Surface functionalization by magnetron sputtering of silver

In the last decade, bacteria became more and more resistant to conventional antibiotics due to excessive use and misuse of those antibiotics in medicine, food industry and agriculture. Infections of orthopaedic implants are associated with a high morbidity, especially because the bacteria tend to generate biofilms on orthopaedic devices and, once biofilms are formed, microbes resist immune attack and antibiotics. As a result, antibiotic-resistant microorganisms have pushed the development of novel antimicrobial agents such as antimicrobial peptides or metallic nanoparticles (NPs), which are stable and provide a large surface area for contact with bacteria [115, 116, 117].

Silver nanoparticles (Ag-NPs) represent an interesting example of such NPs. The antimicrobial properties of silver have been exploited since the ancient times, mostly empirically, long before people realized that microbes were at the origin of the infection [118]. Ag-NPs exhibit a bactericidal activity against Gram-positive and Gram-negative bacteria and are also effective against antibiotic-resistant strains [119].

It has long been known that silver NPs are useful in wound management, and they have been used since the 18$^{\text{th}}$ century to treat ulcers. In the 1920s, the use of Ag was regulated for wound management by the U.S. Food and Drug Administration (FDA)[115]. On these bases, orthopaedic implants coated with Ag-NPs were developed and some of them were utilized in clinical trials [119].

Antimicrobial activity of Ag NPs

The antimicrobial mechanisms of Ag NPs and associated ionic species are still not yet fully understood in details. However, it is now well-accepted that the interactions between Ag NPs and the surface membrane of bacteria play an essential role in the antimicrobial mechanisms (Gram-negative bacteria present a membrane made of layers of lipopolysaccharides, whereas Gram-positive bacteria exhibit layers of peptidoglycans). Various models are proposed in the literature. Three of them are presented in Figure 2.21 [27]:

1. Uptake of free silver ions followed by the disruption of adenosine triphosphate (ATP) production and deoxyribonucleic acid (DNA) replication ;

2. Reactive Oxygen Species (ROS) generation by silver nanoparticles and silver ions ;

3. Direct damage to the bacteria membrane by the silver nanoparticles.
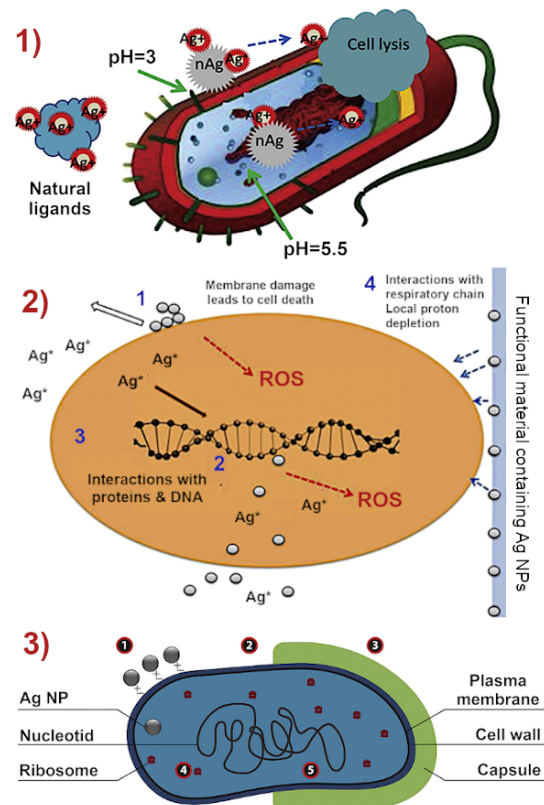
Figure 2.21 – *Known mechanisms of antibacterial action of Ag NPs and Ag^{+} [27].*

Ag deposition by magnetron sputtering

Magnetron Sputtering (MS) is a flexible and widespread coating technique used in many industrial fields, due to its stability, efficiency and up-scaling capability. Regarding biomedical applications, MS offers the possibility to elaborate tailored coatings with different functionalizations that improve the biocompatibility [120].

The MS process starts by applying an electric field (DC, RF or MW) between two electrodes in a chamber at low pressure. The gas (typically Ar) contained in the chamber is then ionized and the ions bombard the target cathode. When the ions

Figure 2.22 – *Schematic representation of a diode sputter system [28].*

have sufficient energy, they induce shocks and momentum transfers with the atoms of the target surface producing their ejection toward the substrate as shown in Figure 2.22 [28].
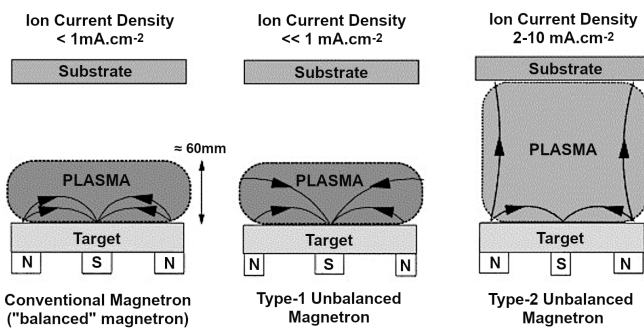
Figure 2.23 – *Schematic representation of the plasma confinement configurations observed in "balanced" and unbalanced magnetrons [28].*

As a function of the magnetic field configuration, various MS techniques can be distinguished: unbalanced and "balanced" magnetrons (Figure 2.23). The main difference lies in the fact that the plasma is more or less confined, which influences the quality of the as-obtained coatings, the yield and the deposition area. Closed-field unbalanced magnetron sputtering (CFUBMS) is currently the most used set-up due to the coating adherence and quality, and the area of deposition. It is the most suitable for multicomponents fabrication and reactive deposition [28].

There are different models (Figure 2.24) that describe the thin film growth modes in MS. These growth modes are mostly influenced by surface tension and materials properties [29]:

1. Volmer–Weber or island growth

2. Frank-Van der Merwe or layer-by-layer growth

3. Stranski–Krastanov growth
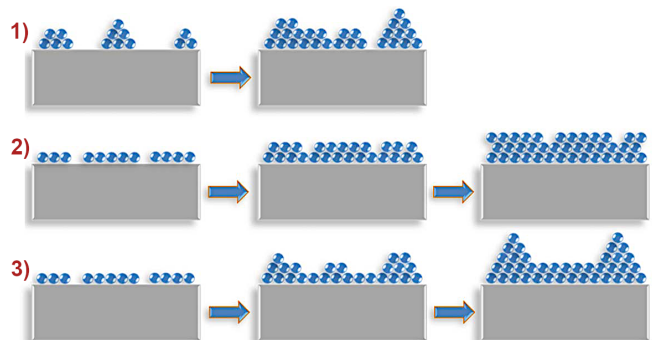
Figure 2.24 – *MS growth modes: 1) Volmer–Weber (island), 2) Frank–Van der Merwe (layer-by-layer) and 3) Stranski–Krastanov growth [29].*

The Volmer–Weber mode corresponds to a growth occuring when the smallest stable clusters nucleate on the substrate and evolve into 3D island features. It results from the fact that deposited atoms or molecules are more strongly bonded to each other than to the substrate. For example, such behaviour is typical of metals deposited onto oxide substrates (which is our case). It can also be observed for oxide-oxide systems.

The Frank–Van der Merwe mode, or "layer-by-layer growth", occurs when the extension of the smallest nuclei appears in 2D resulting in the formation of planar sheets. This mode can be applied to semiconductors on oxide substrates.

The Stranski–Krastanov mode is a combination of the layer-by-layer (Frank–Van der Merwe) and island growth (Volmer–Weber). In this growth mode, in the first step, one or more monolayers are formed following the Frank–Van der Merwe mode, then growing in 3D islands. This is especially the case in metal-metal and metal-semiconductor systems.

Experimental procedure used in this work

All our experiments were carried out using conventional MS in a cylindrical stainless steel chamber. The pressure in the chamber was decreased to 10^{-6} Torr. The system was equipped with a K.J. Lesker Torus magnetron cathode. A silver target having a size of 5 cm in diameter was sputtered in argon. The Ag target was placed at a distance of 15 cm from the GA HAp powder. The cathode was oriented towards the powder. The powder container formed an angle of 45 degrees with the normal to the surface. The target was sputtered in direct current (DC) mode, while the Ar pressure and the power were kept constant at 10 mTorr and 300 W, respectively. The total gas flow of Ar was maintained constant at 40 mL·min^{-1}. As the GA HAp powder showed better CS results than SA HAp (see chapter III), it was used for Ag surface functionalization. Three depositions were carried out for 60, 90 and 120 minutes. Quantitative analyses using Rietveld refinement (HighScore Plus software) from XRD were performed to evaluate the deposited Ag quantity. For a deposition time of 60 minutes, the Ag amount was only 2.9 at. %, whereas for 90 and 120 min the quantities reached 5.4 and 8.4 at.%, respectively. A comparison of the XRD patterns after Ag deposition for 60 and 120 minutes and pattern of naked GA HAp is shown in Figure 2.25 a). These patterns are in agreement with JCPDS 09-0432 and 04-0783, which correspond to HAp (hexagonal P63/m lattice) and Ag (face-centered cubic), respectively. No significant modification of the crystalline structure occurred during the surface functionalization.

The surface morphology of the Ag NPs deposited on the GA HAp powder was investigated using SEM (BSE mode). The results, in the case of a 120 min MS presented in Figure 2.25 b), show that Ag NPs were uniformly distributed onto the GA HAp surface. For 120 min MS, their size distribution was quite narrow with an average diameter around 25 nm.
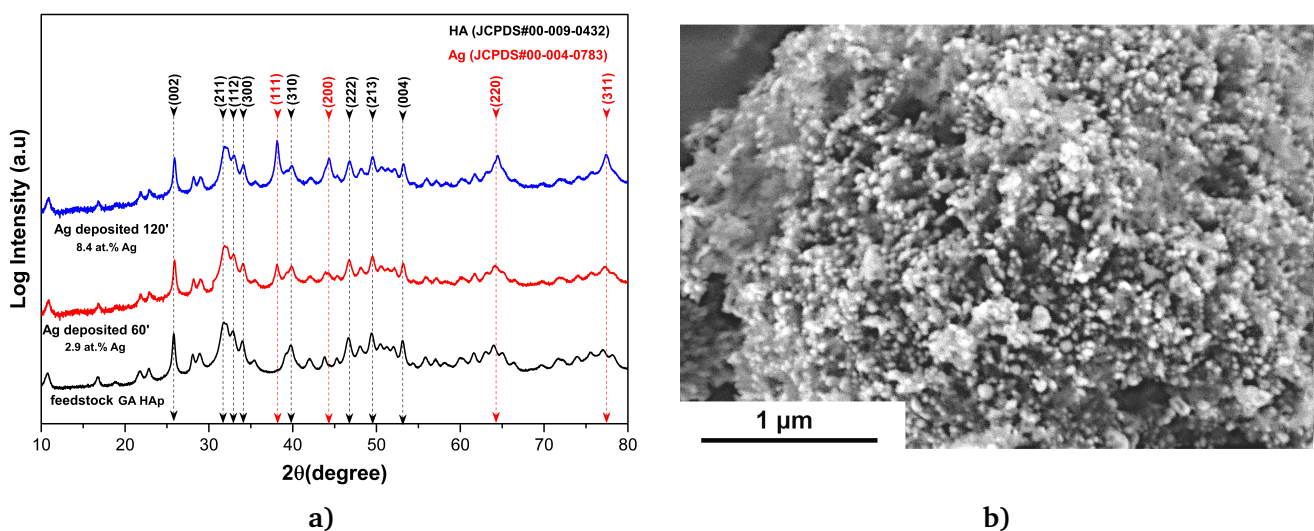
Figure 2.25 – *a) XRD patterns of naked GA HAp powder and after 60' and 120' of Ag deposition by MS ; b) SEM image (BSE) of GA HAp covered with Ag NPs after 120 min MS.*

2.2.3 Chemical and morphological modification of substrates

2.2.3.1 Surface texturing of substrates

The bonding strength of thermal spray coatings is influenced by the substrate surface state, the temperature, the substrate nature with respect to the coating and its topography [121, 122, 123]. Since CS is a solid-state process, the mechanical properties of the substrate must be well-adapted to the coated material [45]. The standard surface preparation for thermal spraying involves the following steps: degreasing, grit-blasting and preheating to get a chemically clean and rough surface with temperatures close to the temperatures of splats [124, 125]. Grit blasting is a cost-effective method for surface topography modification, but grit inclusions can lead to a decrease of the adherence of the coating [121, 122, 123]. The laser surface texturing is a fast, non-contact and clean method for texturing at room temperature. Ion beam and electron beam etching can also be alternative texturing techniques with control over complex shapes but their cost and dimension limits are major drawbacks.

Surface texturing by laser ablation (LST)

Lasers can provide a controlled amount of energy into confined regions of material to achieve the desired response. In metals, optical absorption is dominated by the free electrons through mechanisms such as inverse backscattering. Through phonons collision, the energy is transferred to the lattice. However, specific absorption mechanisms depend on the type of material. In general, photons interact with the available electronic or vibrational states in the material depending on the photon energy. The time from excited electronic states to the fundamental state depends on the specific material properties and is made by phonons thermal conversion. In the case of metals, this thermalization process is of the order of 10^{-12}-10^{-10}s, whereas in non-metals, the time is significantly higher due to different absorption mechanisms. It can be as long as 10^{-6}s [125, 126, 127, 128].
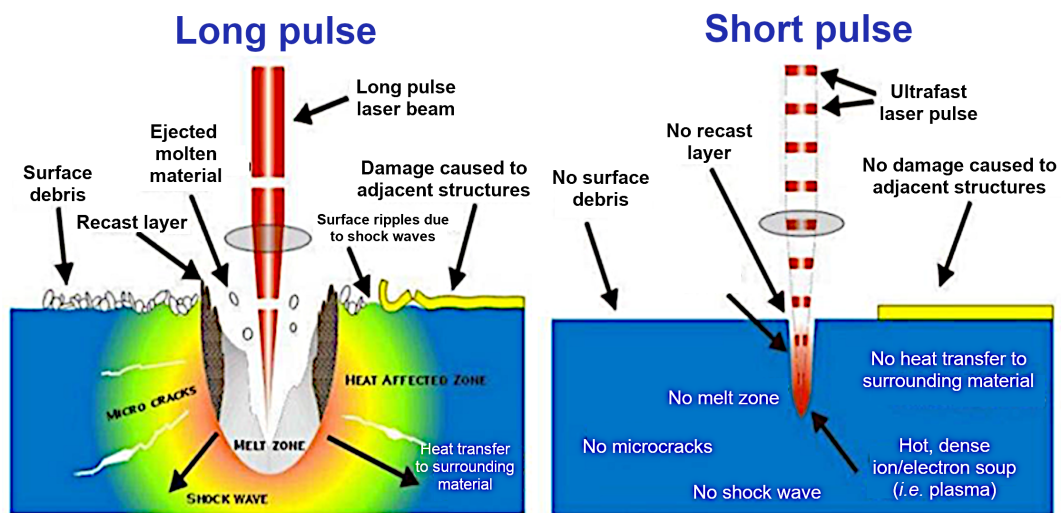
Figure 2.26 – *Long-pulse and short-pulse laser interaction with target material.*

When the excitation rate induced by the laser is low compared to the thermalization rate, the effects of electronically excited transient states are not significant. Instead, the absorbed laser energy can be directly transformed into heat. These processes are called photothermal or pyrolytic, and the response of the material can, therefore, be treated just thermally. For example, the laser treatment of metals or semiconductors with short laser pulses (< ns) is generally characterized by photothermal mechanisms [125, 126, 127, 128].

Laser ablation is the removal of material from the surface by direct absorption of laser energy (Figure 2.26). With multiple pulses, the ablation threshold may slightly decrease due to the build-up of defects. Above the ablation threshold, the thickness or volume of material removed by a single pulse generally shows a logarithmic increase with fluence, *i.e.* following the Beer-Lambert law. A variety of mechanisms may be involved in the laser ablation process, depending on the material and laser parameters, *i.e.* wavelength, laser fluence and pulse duration [124, 126, 127, 128].

Experimental procedure used in this work

LST experiments were conducted using a pulsed fibre laser (Laseo, Ylia M20, Quantel, France). The laser operated at a nominal wavelength of 1.06 μm with a pulse duration of 100 ns, a maximum power of 20 W, and a variable frequency between 10 and 100 kHz. The laser beam was circular with a diameter of 60 μm at the focal point and with a Gaussian energy distribution. The laser patterning consisted of a series of equidistant lines covered with several holes (*i.e.* spotted surface). The scanner stopped the laser beam to form the holes.

a) 5 pulses   **b)** 10 pulses   **c)** 15 pulses

d) 30 pulses   **e)** 40 pulses   **f)** 50 pulses
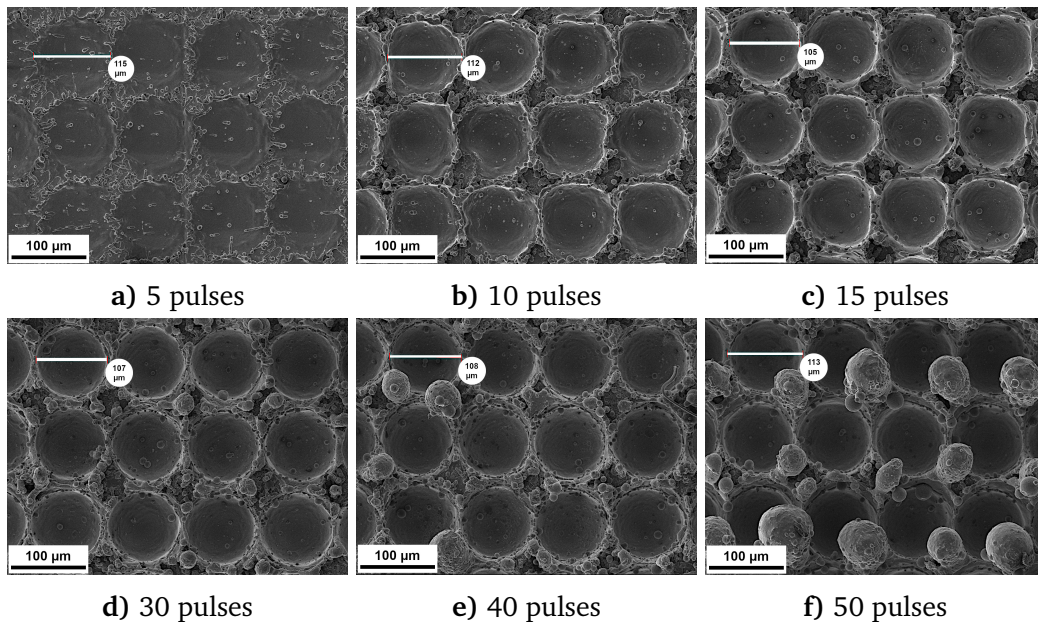
Figure 2.27 – Influence of the pulse number at a constant energy density 28 J/cm

The topography changed strongly with the pulse number, due to local thermalization and material ejection induced by the laser shock wave (Figure 2.27). The "craters" maintained a diameter of $\approx 110 \mu$m regardless the pulse number, but with a depth increase up to 120 μm for 50 pulses. The affected zones were characterized in microhardness on cross-sections. As shown in Figure 2.28, the microhardness increases toward the surface due the rapid cooling as a function of the penetration of the laser, with higher values for ejected and re-crystallized nodules located at the edges of craters.
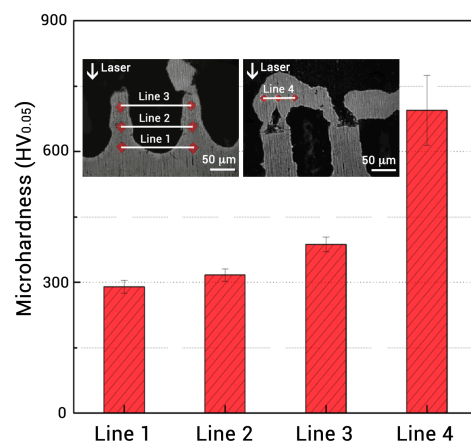
Figure 2.28 – *Microhardness of TA6V after LST (20W, 50kHz, 50 pulses, distance 90μm - 2.27 f)*.

2.2.3.2 Softening by titanium deposition using HPCS

Pure titanium has a higher level of biocompatibility than titanium alloys, but its mechanical properties make it unsuitable for use as a bulk implant. So, many bone implants devoted to withstand high mechanical loads are currently produced using TA6V substrates covered by an HAp coating supported by a sub-layer of Ti [84].

Procedure used in this work

In this PhD, we used a commercially-available pure Ti Grade 2 feedstock powder (>99 wt.% Ti, Metco 4027 series, Oerlikon-Metco, USA - labelled as "CP Ti Grade 2" in this document) for our HPCS experiments. Figure 2.29 shows the particles size distribution combined with SEM observations of this CP Ti Grade 2 gas atomized powder. The distribution is well-adapted to CS. It is quite narrow with highly spherical particles of a diameter ranging from 5 to 20 μm and an average diameter value of about 10 μm.

Concerning the substrates, a TA6V alloy (> 99%, Harald Pihl AB, Sweden) was used. In order to carry out various analyses after coating, two different types of substrates with a disk shape were machined: i) substrates having a diameter

Figure 2.29 – *Particles size distribution and SEM images of the CP Ti Grade 2 feedstock powder used for HPCS experiments.*

of 25 mm dedicated to perform, *a posteriori*, microstructure and phase analyses, as well as mechanical tests, and ii) substrates with a diameter of 8 mm devoted *in fine* to biological tests. The surfaces of those substrates were preliminary prepared through grinding with a SiC paper grit (P120) to remove the natural oxide layer and control the surface roughness. The substrates were also cleaned up in acetone followed by ethanol in an ultrasonic bath prior to deposition.

Three different deposition conditions in terms of gas pressure and temperature were used, corresponding to particles in-flight velocities ranging from 795 m·s^{-1} to 855 m·s^{-1}. All these conditions and associated samples labelling are summarized in Table 2.6. The methodology used to measure in-flight particles velocities is described in Chapter 3, subsection 3.1.2. Figure 2.30 shows the 3D profiles of TA6V substrate and CP Ti Grade 2 coatings, acquired by laser confocal scanning microscopy (LCSM). The roughness parameters calculated from LCSM images are listed in Table 2.7. The significant decrease of coating roughness (Ra) at highest particles velocity is likely due to a more efficient tamping effect.

	Gas pressure [bar]	Gas Temperature [°C]	Velocity [m·s^{-1}]
Sample 1	40	700	795 ± 98
Sample 2	40	900	825 ± 96
Sample 3	50	900	855 ±99

* SoD 20 mm, feed 15 g/min, traverse speed 0.2 mm·s^{-1}, scan step 2 mm.

Table 2.6 – *HPCS deposition conditions of the CP Ti Grade 2 powder*.

a) Substrate

b) Sample 1
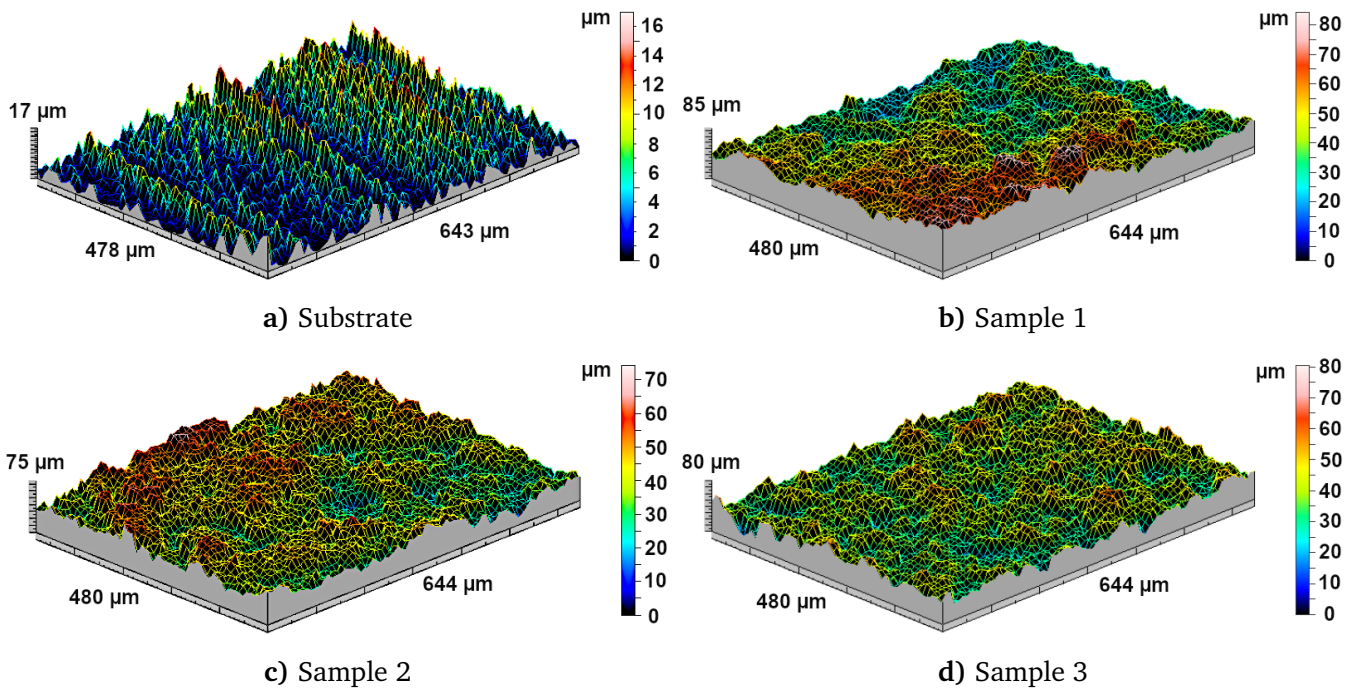
c) Sample 2

d) Sample 3

Figure 2.30 – *3D LCSM images of: a) TA6V substrate, b) sample 1, c) sample 2 and d) sample 3.*

	Ra [μm]	Rq [μm]	Rv [μm]	Rp [μm]	Rt [μm]
Substrate	1.4	1.6	-7.1	4.4	11.5
Sample 1	8.1	10.7	-27.4	35.9	63.3
Sample 2	9.4	12.2	-36.2	35.3	63.3
Sample 3	6.5	8.3	-24.9	18.2	43.1

Table 2.7 – *Roughness parameters of the three different CP Ti Grade 2 coatings and of the TA6V substrate - Calculated from the 3D LCSM images of Figure 2.30.*

The X-ray diffraction (XRD) patterns of the feedstock powder and three different Ti coatings are reported in Figure 2.31. They are in agreement with the data provided by the International Centre for Diffraction Data (ICDD) number 44-1294, showing that no crystallographic modification occurred during the deposition process, the Ti coatings keeping the same hcp crystal structure as the feedstock powder. However, the detection limit of XRD does not allow to accurately account for the potential presence of oxygen. This very important issue concerning the oxygen content will be discussed later in this subsection on the basis of HR-XPS measurements.

Since the HPCS process is extremely dynamic, the energy involved during the impact is essentially released by plastic deformation in the case of titanium, but not by grain growth. The microstructural changes induced by HPCS due to the ballistic impact can be estimated by XRD. More specifically, the diffraction peaks shall exhibit a broadening and/or a shift as a function of the velocity at the impact, highlighting a refinement of the microstructure and/or internal induced strains linked to the dislocation density.

The crystallite size (D) could be evaluated from the Scherrer equation 2.1. The results summarized in Table 2.8 show the effective refinement of the microstructure by applying HPCS (the crystallite size was calculated using the "100% peak", N.A. stands for not available). The crystallite size decreases from

133 nm for the feedstock powder down to 30-40 nm for the CP Ti Grade 2 coatings. However, it is impossible on the basis of our data to give a clear conclusion as for the influence of the initial particles velocity on the level of refinement. In particular, sample 2 corresponding to an intermediate particles velocity should exhibit an intermediate crystallite size. This is not what is observed, likely because we do not have enough sensitivity. HR-XRD would be needed for a better understanding.

$$D = \frac{K \times \beta}{\lambda \times \cos(\theta)} \tag{2.1}$$

Where 'K' is the Scherrer constant, 'λ' is the average wavelength of Cu Kα radiation, 'β' is the full-width-at-half-maximum (FWHM) of the diffraction peak, and 'θ' is the Bragg diffraction angle.

The cell lattice parameters, a and c for hcp structure, were determined according to equation 2.2 for (hkl):(100) Miller indices. Once again, the data do not allow a clear conclusion as for the evolution of the cell volume and microstrain (analysis performed used using PANalytical X'Pert HighScore Plus)level with the particles velocity. Deeper investigations are necessary.

$$\frac{1}{(d_{hkl})^2} = [\frac{4}{3}(h^2 + k^2 + hk) + l^2(\frac{a}{c})^2)]\frac{1}{a^2} \tag{2.2}$$

	a [Å]	c [Å]	Cell volume [Å³]	D [nm]	Microstrain [%]
Theoretical	2.9505	4.6826	N.A	N.A	N.A
Feedstock	2.9517	4.6872	35.368	133.4	0.194
Sample 1	2.9517	4.6835	35.339	41.2	0.271
Sample 2	2.9533	4.6866	35.401	29.8	0.174
Sample 3	2.9514	4.6835	35.332	34.7	0.192

Table 2.8 – *Unit cell parameters, crystallite size and % of microstrain in CP Ti grade 2 coatings.*

As evidenced in Figure 2.32, the CP Ti grade 2 coatings elaborated by HPCS exhibits a relatively dense structure, with some intergranular porosity but mostly with no apparent splat boundaries. In addition, the coatings, whatever the HPCS conditions, show two distinctive regions: a porous top layer, and a dense bottom layer which can be linked to the tamping effect on the particles at the bottom by the successive impacts of the following particles stacking. No morphological features associated with the successive nozzle passes are observed. Similar microstructures are reported in the literature for spherical and irregular powder morphologies [129, 130, 131].

Figure 2.31 – *XRD patterns of the CP Ti Grade 2 powder and Ti coatings deposited by HPCS.*

Finally, the interfaces between the substrates and coatings are well-bonded along their entire span. As already mentioned, a higher particles velocity leads to a more significant deformation and

therefore, coating structure becomes denser due to the softening caused by local shear instabilities [54].
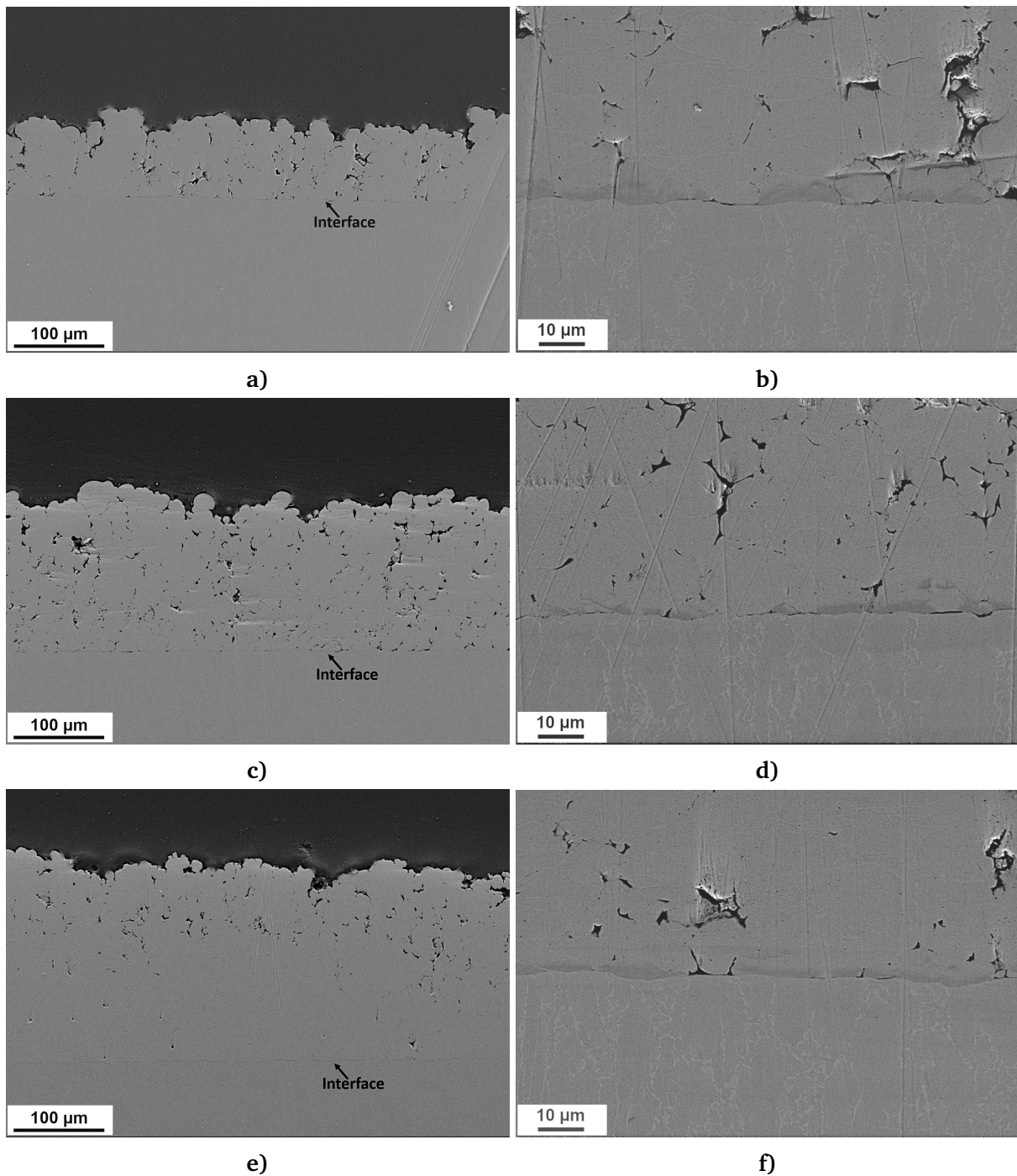
Figure 2.32 – *SEM cross-sections of CP Ti Grade 2 coatings at low and high magnifications: a) and b) sample 1, c) and d) sample 2, e) and f) sample 3.*

The intergranular porosity was quantitatively estimated by image processing (10 images per sample) using Image J, a free software developed at the NIH (National Institute of Health). Assadi *et al.* [132] studied in their work an empirical parameter called η corresponding to the ratio between v_p and v_{cr} (*where 'v$_p$' is the particles velocity, and 'v$_{cr}$' the critical velocity which represents the minimum theoretical velocity to adhere to the substrate*). If the value of η is lower than 1, the deposition efficiency is low, and the adhesion of the particles to the substrate is weak. Moreover, the deposition efficiency (DE) and adhesion exponentially increase till η reaches 2, followed by an erosion phenomenon when η exceeds this value of 2.

The adhesion strength was measured by pull-off tests using an HTK ultra-bond epoxy glue as described in ASTM 633-13 which is especially adapted for thermal spray coatings. In this ASTM standard, the sample, a disk of 25 mm in diameter, is glued between 2 metallic bars with the epoxy and cured at 150°C for 2h for consolidation. Then, a tensile load is applied at a constant speed of 0.02 mm·s⁻¹ up to the rupture. The validity of the test requires to systematically verify that the rupture occurs in the coating zone, at or near the interface with the substrate. The adhesion strength is evaluated from the following simple formula 2.3:

$$Adhesion \quad strength = \frac{rupture \quad load}{loaded \quad area} \tag{2.3}$$

The measured or calculated v_p, v_{cr}, η, DE, thickness, porosity and adhesion strength are listed in Table 2.9. The results are logical. The increase of the initial in-flight particles velocity conducts to an increase of thickness for a fixed coating time and to a significant decrease of porosity. The other parameters, like DE, adhesion strength and η remain rather stables. This suggests that no specific chemical mechanisms are activated with the particles velocity, at least in the range of velocities studied. The consolidation is only due to a physical phenomenon linked to shear instabilities at the impact that promotes the mechanical anchor through the resorption of porosity. It must also be noticed that the value of η is exactly in the good range for an efficient CS process as predicted by Assadi *et al.* [132].

	v_p [m.s⁻¹]	v_{cr} [m.s⁻¹]	η [a]	Deposition efficency [%]	Thickness [μm]	Porosity [%]	Adhesion strength [MPa]
Sample 1	≈795		1.22	89	80±30	7.1	54±6
Sample 2	≈815	650	1.25	90	170±25	3.1	59±5
Sample 3	≈855		1.31	91	200±35	2.1	62±8

Table 2.9 – *CP Ti Grade 2 coating properties as a function of the initial in-flight particles velocity in HPCS.*

In order to better understand the surface chemistry of titanium coatings made by HPCS, X-ray photoelectron spectroscopy (XPS) analyses were conducted more specifically to detect the extreme surface elemental compositions and chemical states. The Figure 2.33 shows the XPS wide scan spectra of as-sprayed Ti coatings, and the same coatings after etching with Ar ions for 10 minutes. The results emphasize that titanium (Ti) and oxygen (O) are the major elements, whereas C, N, and Ca are present in low quantities.

When looking at a higher resolution on the specific Ti $2p_{3/2}$ and Ti $2p_{1/2}$ core-level spectra of as-sprayed coatings, it appears that the Ti $2p_{3/2}$ and Ti $2p_{1/2}$ peaks are located at 459.7 eV and 464.4 eV, respectively. These peaks can be attributed to Ti^{4+}. No Ti^{3+} shoulder at lower binding energy on the Ti $2p_{3/2}$ peak is detected, suggesting that all samples present a stoichiometric TiO_2 surface. As it can be seen in wide scan, Ti 2p spectra consist of high-energy shake-up satellites at 477.8 eV and 472.4 eV which are typical of TiO_2. It is in agreement with the thermodynamics, which specifies that the free energy of formation of TiO_2 is favoured over other titanium oxide forms.

The Ti 2p spectra of as-sprayed CP Ti Grade 2 and Ar^+ etched coatings are found to be quite different. It can be observed that the near-surface region of as sprayed CP Ti Grade 2 is mainly composed of TiO_2 peaks with low-intensity Ti-metal peaks. In comparison, only Ti metal element can

be identified at the extreme surface of the etched coatings. This result indicates that TiO_2 is present just at the surface of the as-sprayed coatings as a passive layer formed by the reaction between the CP Ti and the O_2 coming from the surrounding atmosphere during HPCS.
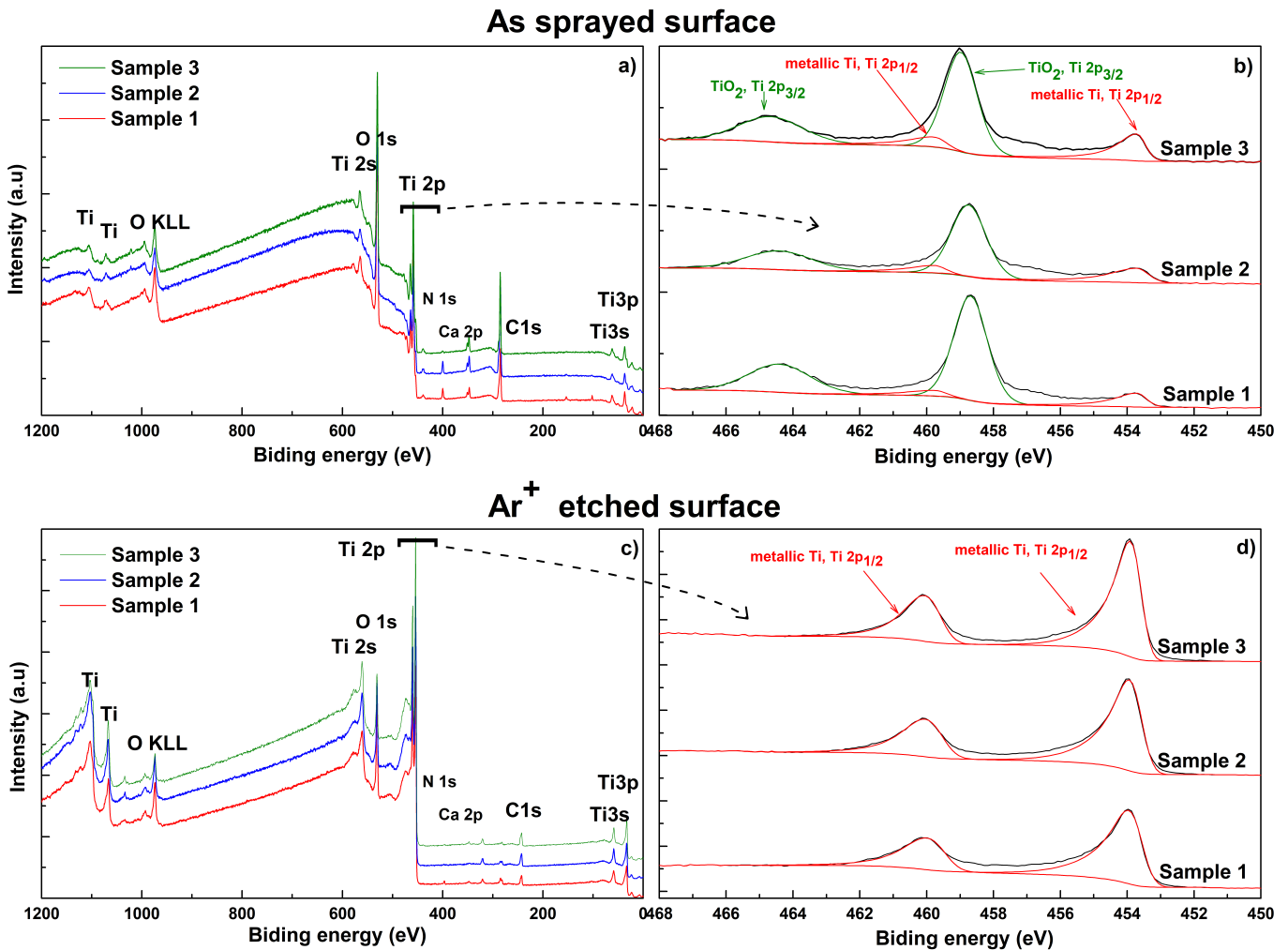
Figure 2.33 – *HR-XPS spectra of as-sprayed Ti coatings and after 10 min of Ar^+ etching.*

The atomic concentrations of O 1s, Ti 2p and C 1s were calculated from the HR-XPS spectra. They are listed in Table 2.10. The results show clearly the effect of Ar^+ etching, which reduces a bit the O 1s concentration but increases quite significantly the Ti 2p concentration. Please notice also the drastic reduction upon etching of C1s that may occur by the result of the elimination of organic pollutants present at the surface.

	Before etching			After etching		
	O 1s [at.%]	Ti 2p [at.%]	C 1s [at.%]	O 1s [at.%]	Ti 2p [at.%]	C 1s [at.%]
Sample 1	45.3	16.4	37.1	41.2	46.8	12.1
Sample 2	35.1	11.1	52.0	34.1	57.1	8.8
Sample 3	40.5	17.3	40.5	25.7	25.7	5

Table 2.10 – *Atomic concentrations of O 1s, Ti 2p and C 1s determined from HR-XPS spectra for as-sprayed CP Ti Grade 2 coatings and after 10 min of Ar^+ etching.*

2.3 Cold spray facility description

The coating deposition by CS was performed in this work using a high-pressure Impact Innovations equipment (Germany), namely the Impact Spray System 5/11.

This high-pressure CS equipment can operate at a maximum gas temperature of 1100°C and a pressure of 50 bar. The maximum heating power is 40 kW. It exhibits a control cabinet with an integrated power supply and gas control, 2 high-pressure powder feeders, and an integrated heating gun as shown in Figure 2.35. The qualitative geometry of the SiC (or WC) nozzle

Figure 2.34 – *Geometry of a SiC nozzle obtained by X-ray micro-tomography*.

(5.6 expansion ratio) obtained by X-ray micro-tomography is presented in Figure 2.34. The exact dimensions of the nozzle cannot be given being the property of Impact Innovations Company.
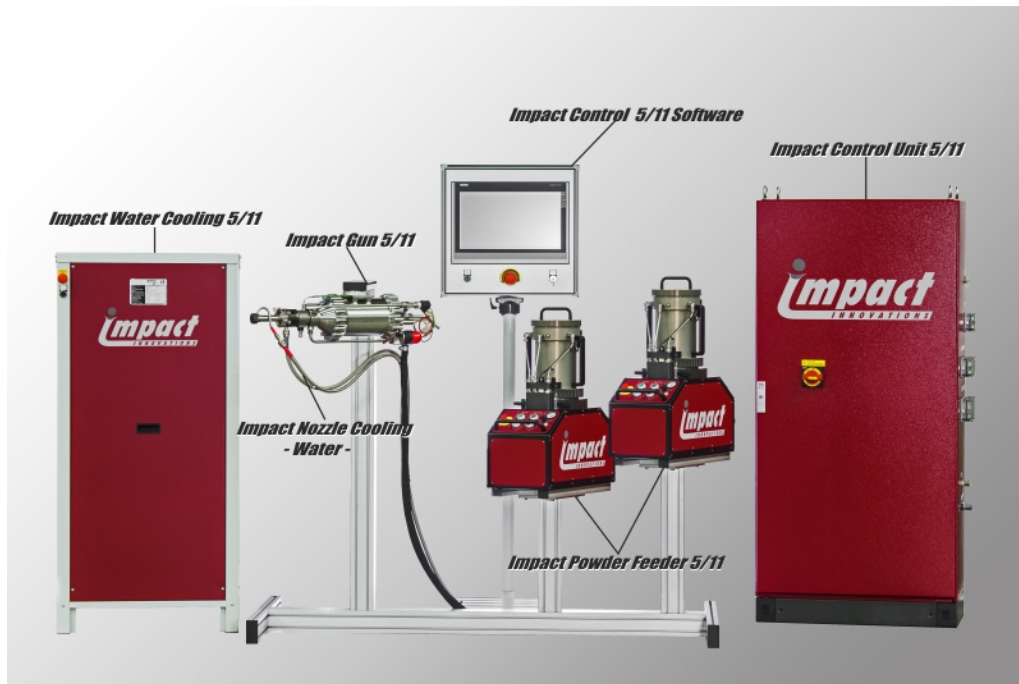
Figure 2.35 – *The Impact Spray System 5/11 from Impact Innovations Company*.

The convergent-divergent, or de Laval nozzle, is a key component in the CS system. In such a nozzle, the flow can be accelerated or decelerated by changing the flow areas. At the nozzle inlet (convergent part) the gas flow is in the subsonic regime followed by a progressive increase to the sonic regime after the throat. The gas velocity at the nozzle outlet can be expressed by equation 2.4. It affected by the type of gas, its pressure and temperature, and the nozzle design [133, 134, 53].

$$v_e = \sqrt{\frac{TR}{M} \cdot \frac{2\gamma}{\gamma - 1} \cdot \left[1 - \left(\frac{p_e}{p} \right)^{\frac{\gamma - 1}{\gamma}} \right]} \tag{2.4}$$

Where 'v$_e$' is the gas velocity at the nozzle exit, 'T' the absolute temperature of the inlet gas, 'R' the ideal gas constant, 'M' the gas molecular weight, 'γ' the adiabatic coefficient, 'p$_e$' the absolute gas pressure at the nozzle exit, and 'p' the absolute pressure of the inlet gas.

According to the law of mass conservation of mass, the mass flow rate of the gas throughout the nozzle remains the same regardless of the cross-sectional area (Equation 2.5).

$$\dot{m} = \frac{A}{\sqrt{T_t}} \cdot \sqrt{\frac{\gamma}{R}} M \cdot \left(1 + \frac{\gamma - 1}{2} Ma^2\right)^{-\frac{\gamma+1}{2(\gamma-1)}}$$

(2.5)

Where 'ṁ' is the mass flow rate, 'A' the cross-sectional area of the throat, 'T_t' the total temperature, 'R' the ideal gas constant, 'M' the gas molecular weight, 'γ' the adiabatic coefficient, 'M_a' the Mach number and 'p' the absolute pressure of inlet gas.

For the purpose of this PhD work, our CS was equipped with an axial powder injector presented in Figure 2.36. Such an injector offers the possibility to adjust the powder injection point, and allows for a better flowability compared with the classical radial powder injector (Figure 2.36). Additionally to this, the upstream injection position maintains the benefit of the powder preheating effect, especially for high temperature alloys and ceramic powders. It must be mentioned that the powders, especially ceramics or hard metals, can significantly erode the de Laval nozzles even though they are made out of SiC (or WC). Another important point is the cooling of the nozzle by water or air which helps preventing from its clogging.

Radial Injector
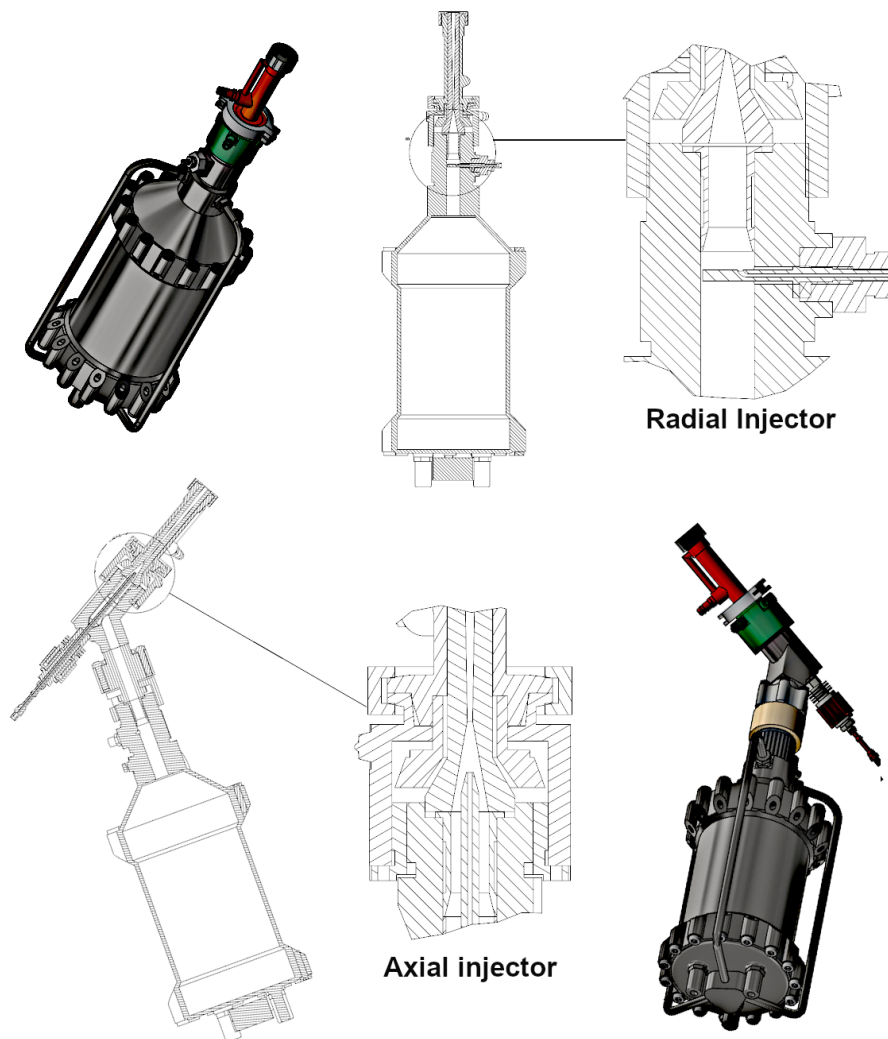
Axial injector

Figure 2.36 – *Standard radial powder injector and axial powder injector of the Impact 5/11 system.*

2.4 Conclusion - Chapter 2

After a brief description of the different characteristics of the studied materials (hydroxyapatite, collagen, bioglass), the synthesis of agglomerated powders (*i.e.* granules) by atomization has been presented. Collagen has been added to the granules to promote both i) a pseudo-plastic behaviour of projected granules at the impact during the CS process and ii) a biological activity of the as-obtained deposits. Specific preparations of the substrates (grit-blasting, laser texturing, softening through Ti grade 2 deposition as a sub-layer) have also been performed to increase the deposition efficiency and/or the mechanical adhesion. Finally, the CS system we have used to elaborate HAP-based deposits further presented in Chapter 3 has been described in details. An emphasis has more specifically been made on the configuration of the feedstock injectors that may affect the stability of the powder jet and thus the quality of the coatings at the end.

Chapter 3 : Build-up of hydroxyapatite-based coatings by CS

Overview ────────────────────────────────

To date, the bonding phenomena leading to the consolidation of ceramic coatings deposited by CS are not completely elucidated and remain under debate. Often, researchers discuss the CS bonding mechanisms while comparing to what happens in aerosol deposition method (ADM), also named as vacuum cold spray. Indeed, the only differences between CS and ADM are that for ADM the deposition is performed under vacuum and the feedstock is in the form of a micron size powder. As mentioned in Chapter 1, CS is a solid-state kinetic process. Therefore, a significant importance should be given to the particles size distribution, and to the mechanical properties and velocity of the particles. Large size distributions are translated to different velocities resulting in different kinetic energy at the impact, which influences the deposition efficiency, especially for ceramic feedstocks. Since ceramics exhibit an intrinsic brittle nature, the ability to fragmentation and post-consolidation also plays an essential role in the build-up of the coating. The cold-sprayed ceramic coatings quality depends not only on the CS process parameters, but also on the feedstock powder and substrate characteristics.

The Section 3.1 is dedicated to the understanding of the powder behaviour by the study of the intrinsic mechanical properties of elementary agglomerates, their in-flight velocity and the phenomenology of a single agglomerate impact on the substrate. For metallic coatings, different deposition models have been developed. Although not fully adapted to the case of ceramics, these inspiring models allow for a better understanding of the bonding mechanism and the calculation of the minimum velocity, called critical velocity, that has to be reached to build-up a coating.

The section 3.2 presents the deposition parametric range we used to deposit HAp coatings by CS, as well as the microstructural, phase composition and mechanical characterisations. All these results are linked in an attempt to propose a bonding mechanism responsible for the coating consolidation.

Finally, in the section 3.3, novel functional HAp hybrid coatings, with potentially enhanced bio-activity through the addition of bioglass or collagen are presented for the first time.

3.1 Characterization of properties of single agglomerates

When compared to conventional thermal spraying techniques such as plasma or flame spraying, CS is a solid-state process. The particles remain unmelted during the deposition. As a consequence, the intrinsic mechanical behaviour of feedstocks plays a key role in the coating formation. Contrary to metals, the deposition of ceramics by CS is difficult to achieve due to the lack of plasticity of the particles at the impact. In order to better understand the impact behaviour, here dynamic micromechanical measurements have been performed in-situ in a SEM on single agglomerates to determine their intrinsic mechanical behaviour. Even if the sollicitation speed involved during CS (further presented in section 3.1.2) is much higher than that of the set-up installed in the SEM, these very original measurements can provide useful data allowing to etablish correlations to better understand the deposition mechanisms.

3.1.1 *In-situ* SEM micromechanical testing

In situ experiments in a SEM have gained significant attention in recent years due to their ability to accurately observe the failure mechanisms of very small specimens. In addition, observing the deformation of the tested specimen at a local scale and monitoring the mechanical response in the same time are very useful for the understanding of materials properties.

In our case, compression tests were carried out at Imperial College London using an Alemnis nanoindenter (Figure 3.1 a)) mounted in a FEI Quanta 450 FESEM, with a conospherical indenter tip having 20 μm flat punch (Figure 3.1 b) - Tests were also done with Berkovich and Cube Corner indenters, but with no significant differences so that they are not shown here). The nanoindenter was composed of a load cell (500 mN maximum load), which measured the force at the mN scale, and of a piezo-actuator which permitted to apply precise displacements in the range of a few nm up to 35μm. The microcantilever was aligned with the loading axis parallel to the SEM stage and with the cantilever side surface inclined at 52° for in-situ SEM observation. These components were combined in a rigid frame with stick/slip positioners allowing the sample to be moved in the X-Y axes relative to the sample surface and the indenter to be moved in the Z-axis.

a)   b)
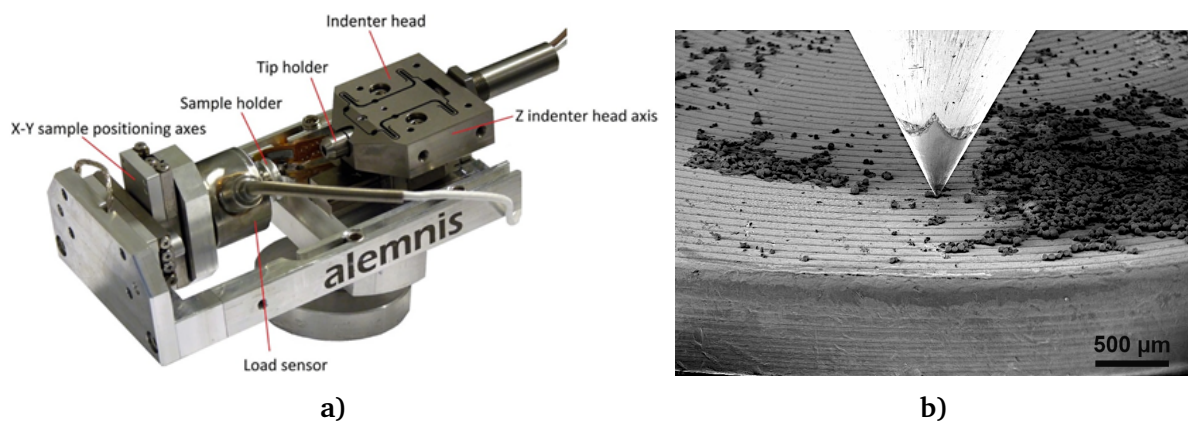
Figure 3.1 – *a) Alemnis indenter and b) SEM image of the powder and conospherical indenter tip.*

Each tested agglomerate was considered to be a perfect sphere. The contact between the agglomerate and the tip could evolve during a compression tests, so that the applied stress evolved also significantly (Hertz contact theory [135]). However, the nominal rupture stress could be evaluated

using the following formula [136, 137]:

$$\sigma_f = \frac{4F_f}{\pi D^2} \tag{3.1}$$

Where: 'F$_f$' corresponds to the maximum fracture load of the particle and 'D' is the diameter of the particle.

Sample preparation

Two drops of a low concentrated HAp acetone suspension were dropped cast on a SEM stub, followed by 30 seconds of gold coating after the acetone vaporisation. Two types of experiments were carried out. Firstly, SA agglomerates were compressed up to burst at 0.5, 1 and 5 μm·s^{-1}, in order to check the influence of the loading rate. For GA the compression till burst was performed only at 1μm·s^{-1}. Secondly, load-reload sequential tests were performed for GA and SA at 0.5 μm·s^{-1}.

It must be noticed that, in all cases, the loading rates we applied were very low in comparison to what is actually encountered in CS. So, we just have an indication of the activated fracture mechanisms that may differ significantly from what really happens in ballistic conditions. Being aware of that, Figure 3.2 presents a typical force-displacement curve for SA compressed at 0.5 μm·s^{-1}. The shape of the curve is highly characteristic and actually similar whatever the materials (SA or GA) and loading rates tested. At point A, the indenter begins to touch the agglomerate. The force increases then linearly as the particle is compressed (segment AB) traducing the elastic response of the agglomerate. The point B corresponds to the first crack initiated, followed by a catastrophic rupture highlighted by point C. The DE part of the curve results from the recovery of load due to debris under compression. The agglomerate exhibits a multiple rupture mode by splitting into many fragments, the larger ones at the periphery opening like "flower petals". Such typical fragments can be observed in Figure 3.3. The peak of compression load (at B in Figure 3.2) is used to calculate the compressive strength (nominal rupture stress) with the equation 3.1. The reproducibility upon multiple tests is rather satisfying for qualitative comparisons (Figure 3.2 (right)), especially when taking into account the fact that our agglomerates are far from being model particles. The calculated compressive strength is around 5 to 6 MPa for the tests reported in Figure 3.2.
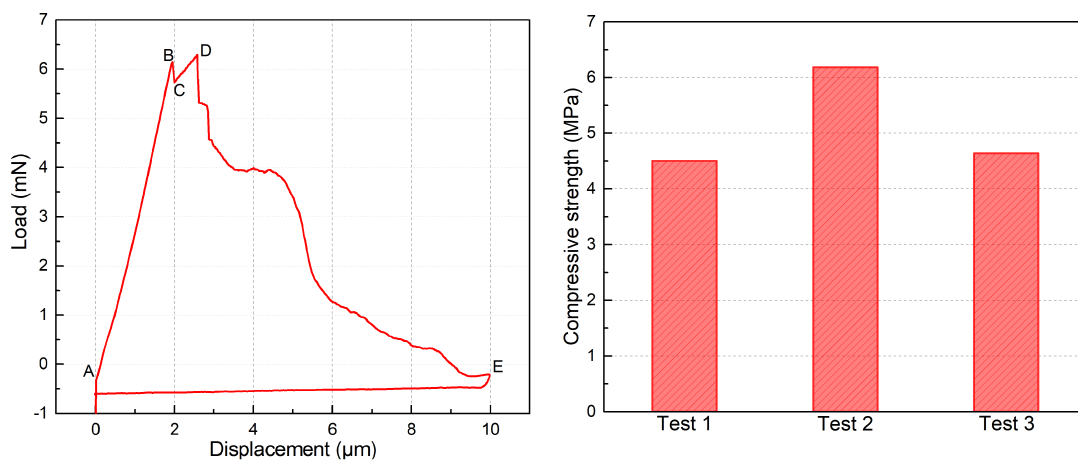
Figure 3.2 – A typical force-displacement curve for a SA agglomerate compressed at 0.5 μm·s^{-1} (left) and reproducibility of the results upon 3 experimental tests (right).

For the sake of comparing qualitatively and quantitatively the different samples, the results of
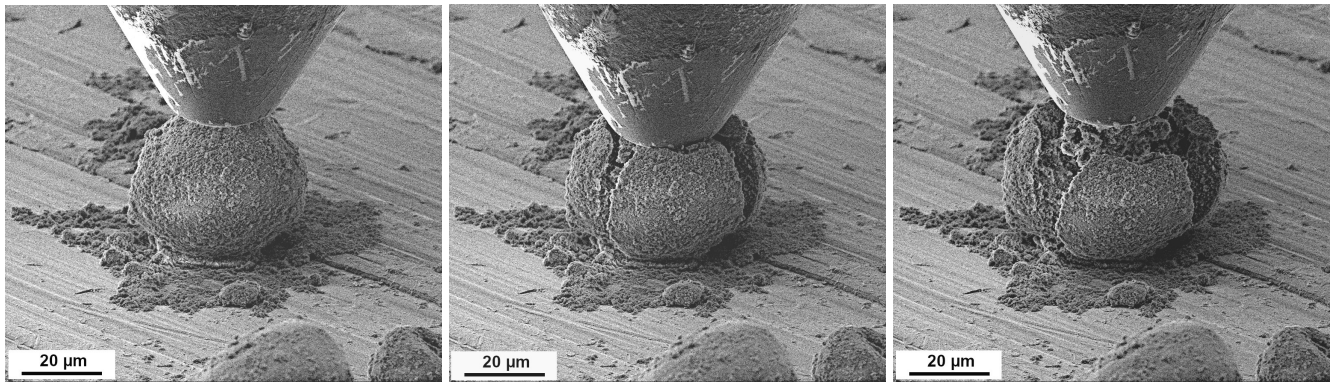
a) Before compression (A point)   **b)** During compression(A-D)   **c)** After compression (E point)

Figure 3.3 – *SEM images of a single SA agglomerate compressed at 0.5 $\mu m \cdot s^{-1}$.*
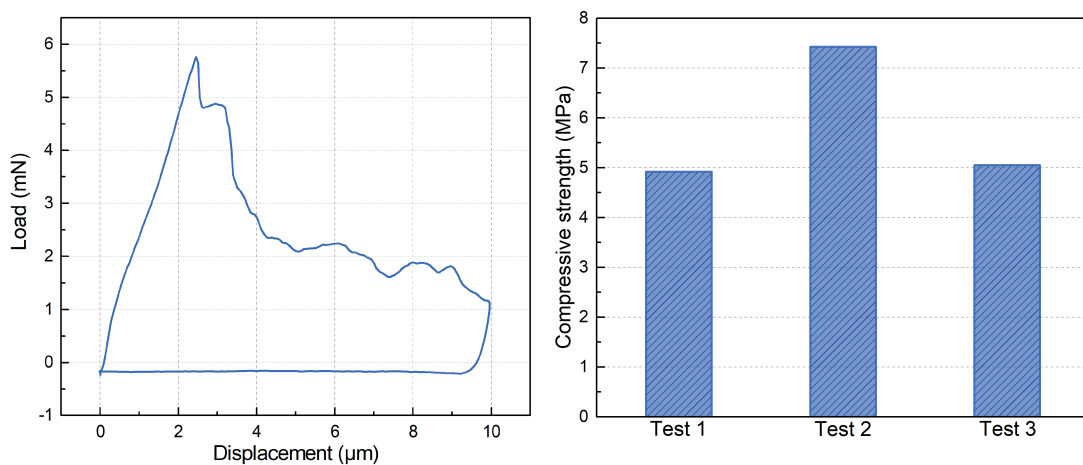
Figure 3.4 – A typical force-displacement curve for a SA agglomerate compressed at 1 μm·s^{-1} (left) and reproducibility of the results upon 3 experimental tests (right)

the other testing conditions for SA and of the test for GA at 1 μm·s^{-1} are reported in Figure 3.4 to Figure 3.8. For even better in-depth analyses, both the energy stored by the tested agglomerates before failure (E_{AB}) and the total energy consumed during the overall compression test (E_{AE}) were evaluated. E_{AB} corresponds to the area below the almost elastic part of the curve (from point A to point B), whereas E_{AE} corresponds to the area below the entire curve (from A to E). The different energy values can be simply calculated multiplying the load by the displacement with respect to the frontiers previously defined. To be representative of the variability of the agglomerates behaviour, at least five tests on five different agglomerates were performed for a given experimental condition and material. The values for E_{AB} and E_{AE} are not reported here simply because they are rather close to each other in both cases for the various samples and testing conditions. They do not allow to conclude as for a potential difference of failure mechanisms between SA and GA. The only thing we observe is a significantly higher variation for E_{AE} due to the random formation of fragments and the way they sustain the load afterwards. The conclusion is that, even if highly relevant, *in-situ* SEM experiments are not sensitive enough in our case (*i.e.* non model particles). We then decided to switch to a new more sensitive testing configuration, namely sequential loading-unloading tests with small displacements involved each time.

a) Before compression   **b)** During compression   **c)** After compression
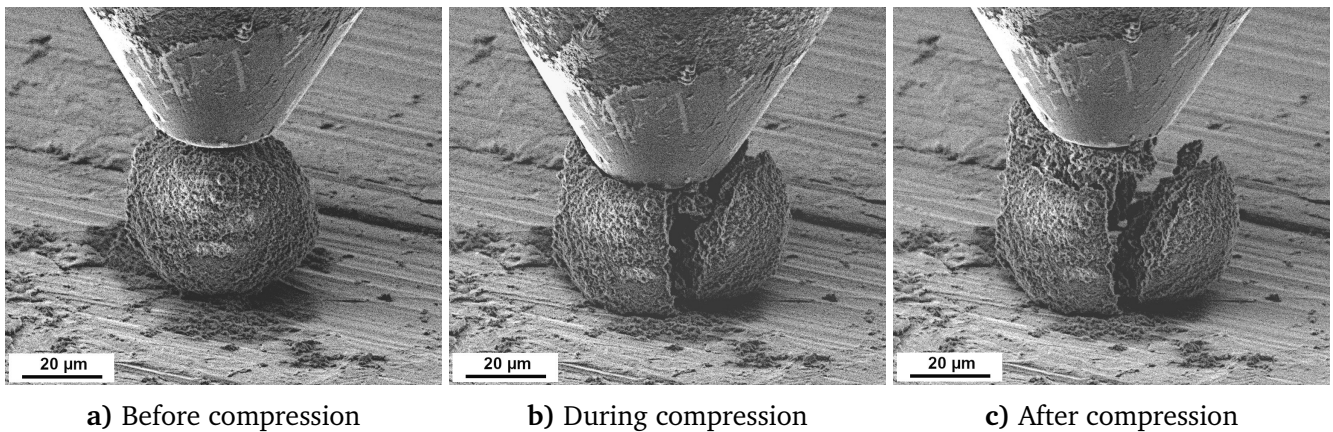
Figure 3.5 – *SEM images of a single SA agglomerate compressed at 1 μm·s^{-1}.*
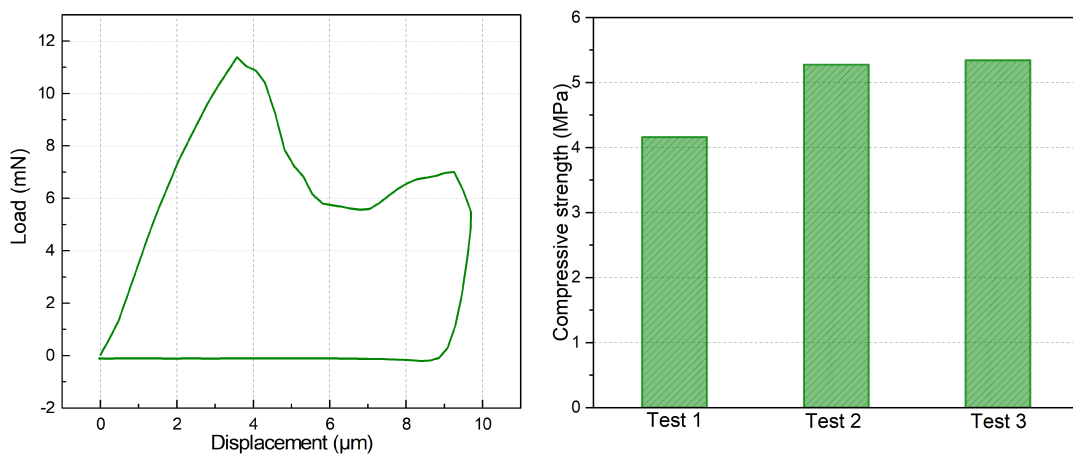
Figure 3.6 – A typical force-displacement curve for a SA agglomerate compressed at 5 μm·s^{-1} (left) and reproducibility of the results upon 3 experimental tests (right)

Figure 3.9 and Figure 3.10 show the results of cyclic compression on GA and SA. These cyclic tests are more representative of the multiple impacts occurring during CS. As a result, the trends in terms

a) Before compression   **b)** During compression   **c)** After compression
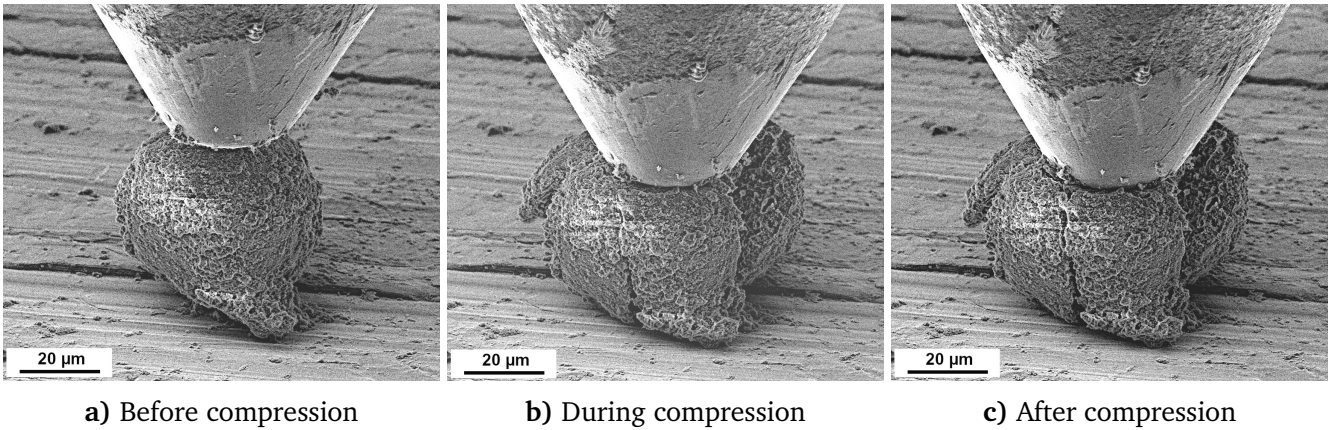
Figure 3.7 – *SEM images of a single SA agglomerate compressed at 5 µm·s⁻¹.*
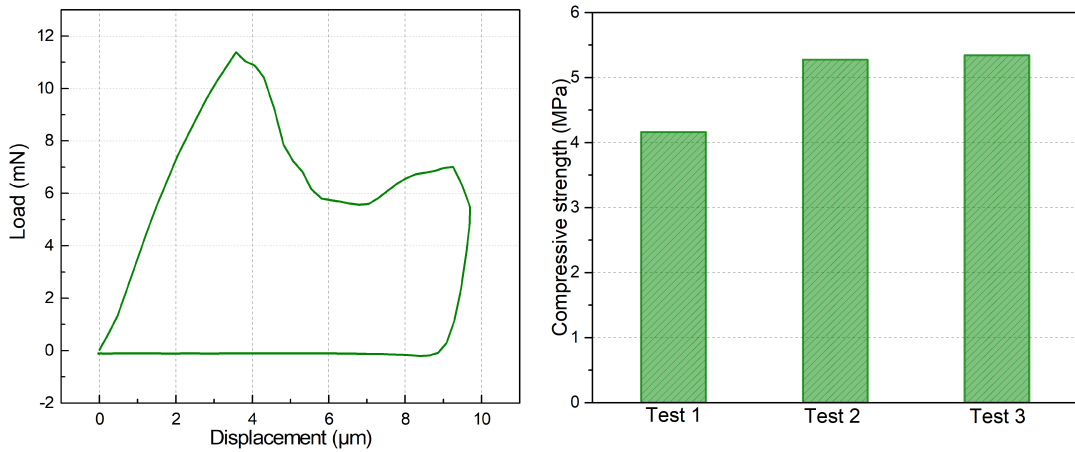
Figure 3.8 – *A typical force-displacement curve for a GA agglomerate compressed at 5 µm·s⁻¹ (left) and reproducibility of the results upon 3 experimental tests (right)*

a)   **b)**
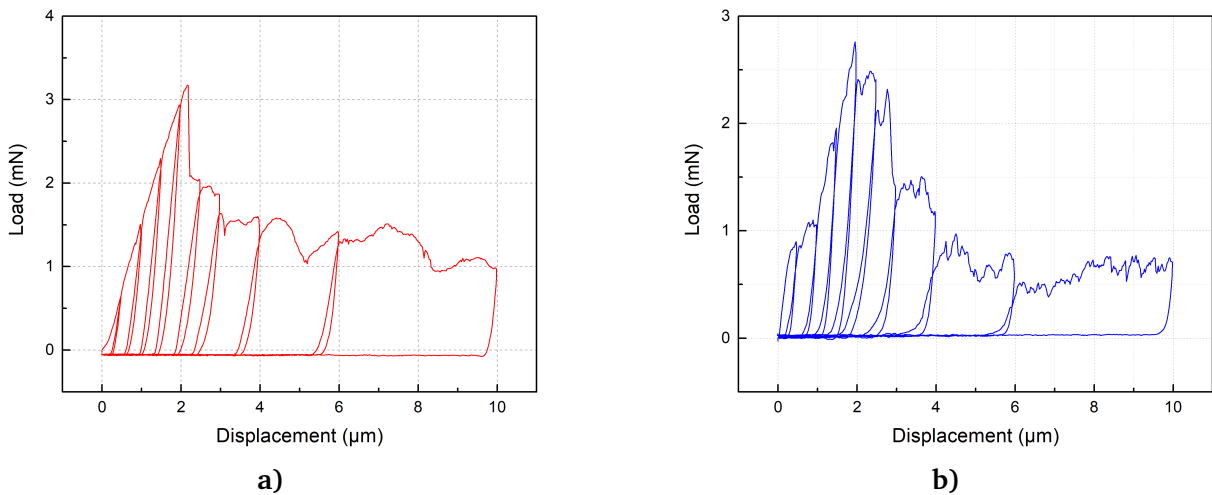
Figure 3.9 – *Loading-unloading cyclic compression: a) on GA and b) on SA*

a)   b)
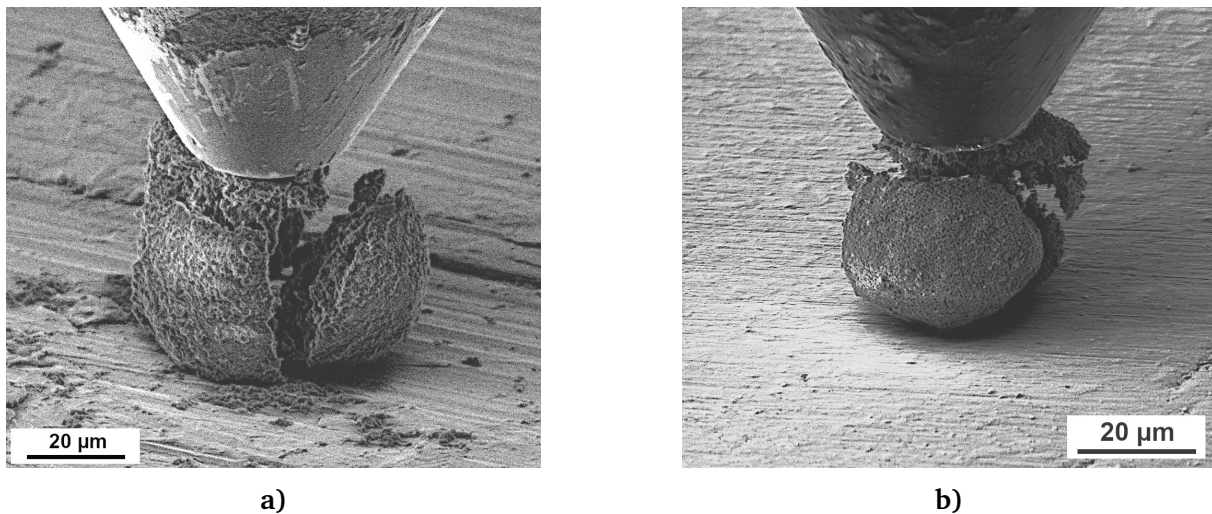
Figure 3.10 – *SEM images of 9 cycles of compression for a) GA and b) SA.*

rupture mechanisms between GA and SA are clearer. More specifically, the mobility of the elementary particles in GA is higher and more energy is consumed through deformation after the initiation of the failure. In the case of SA, the more cohesive (brittle) nature appears clearly in Figure 3.9 through many oscillations observed during the progressive fracture of the debris. These oscillations correspond to the strong bonds and frictional forces needed to be counterbalanced to promote the mobility of elementary particles. This will have obviously an impact on the elementary particles compaction during CS, GA-based coatings being expected to be more compacts upon tapping effects. At this stage, we need also to mention that there is a fundamental difference between our cyclic tests and what happens in the reality for CS. In CS, the tapping effect occurs in a more or less confined environment due to the presence of surrounding particles. In cyclic tests, the lateral mobility is not blocked by the presence of matter.

3.1.2   Analysis of the in-flight particles velocity

As cold spray is a solid-state coating process involving kinetic energy, the amount of motion is a key parameter including the contributions of velocity and density of particles in combination with the process parameters.

Since the particles are "cold" and then keep their integrity before reaching the substrate, Particle Image Velocimetry (PIV) can be used to measure the in-flight particles velocity. The HiWatch CS2 system (Oseir Ltd., Tampere, Finland) used for the velocity measurements is a backlight-illuminated imaging sensor with an integrated invisible NIR laser diode sheet dedicated to illuminate the cold particles. The HiWatch camera detects the scattering phenomena due to particles passing in front of the laser beam as shown in Figure 3.11. The particles velocity is determined by the trace method: distance of the identified particle traces in a single triplet divided by the laser pulse duration, as shown in Figure 3.12. This technique also enables the particles size measurement in a same way as laser granulometry method.

Oseir HiWatch-CS2 capabilities:
- Particle velocity, position, diameter
- Measurement area: ~ 8x6 mm²
- Measurement depth: ~ 1 mm
- Particle velocity range: 0-2000 m.s⁻¹
- Particle diameter range: 5-1000 μm
- Capture speed > 10 fps
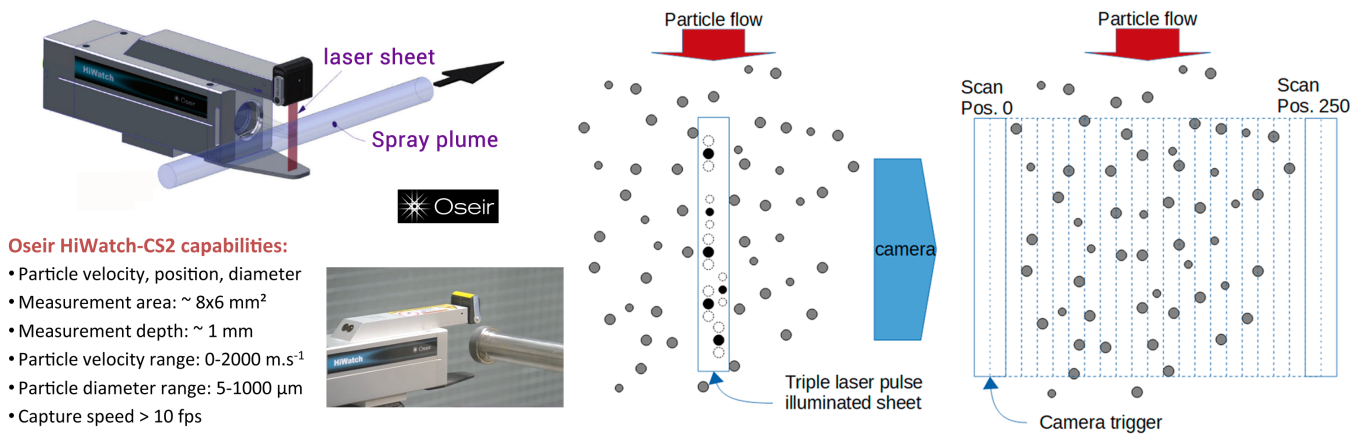
Figure 3.11 – *Particles velocity measurement using the Oseir HiWatch CS2 camera [30]*

A single particle motion in a jet with a high energy stream is influenced mostly by the inertia forces, F_i, and the viscous drag forces, F_D:

$$F_i = \frac{\pi d_p^3}{6} \cdot \rho_p \cdot \frac{du_p}{dt} \qquad (3.2)$$

$$F_D = \frac{\pi d_p^2}{4} \cdot \frac{1}{2} \rho_p \cdot u_R^2 \qquad (3.3)$$

Where 'd_p' (m) is the particle diameter, 'ρ_p' (kg/m³) the particle density, 'ρ' (kg/m3) the plasma density, 'C_D' the drag coefficient, 'u_p' (m/s) the particle velocity, u_R (m/s) the relative velocity between the plasma and the particle and t (s) the time.
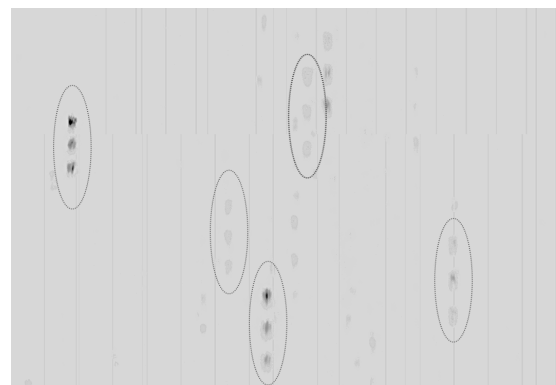
Figure 3.12 – *Processed image which shows particled triplets detected using HiWatch CS2.*

As mentioned in subchapter 1.1.3.4, each material has a specific critical velocity V_{cr}. Above V_{cr}, the particles adhere to the substrate, causing plastic deformation and/or fragmentation and formation of the coating, whereas at velocities lower than V_{cr} only erosion and particle rebound occur without any coating build-up. Therefore, it is important to understand the in-flight velocities of particles [54].

In-flight particles velocity measurement

The chosen spraying conditions made it possible to study the influence of the stand-off distance SoD (*i.e.* distance between the nozzle outlet and the substrate) and pressure on the average particles velocity. The gas temperature, carrier gas and feed rate were maintained constants. The SoD varied from 10 mm to 90 mm. The results are based on 500 images with 0.5 ns exposure time. Particles velocity and size measurement are based on stroboscopic image analysis (see Figure 3.12). Captured images are analysed by the Oseir HiWatch software upon the contrast variation between the particles and the surrounding background. The images with particles outside of the focus plane are systematically excluded to promote the accuracy of the measurements.

Figure 3.13 – *Mean particles velocity measured with HiWatch at various stand-off distances and pressures.*

As illustrated in Figure 3.13 and as expected, the particles velocity increases with the pressure for a given SoD. In addition, for a given pressure, the particles velocity decreases when the SoD increases. This decrease with SoD can be simply explained by the hydrodynamic interactions between the particles jet and the surrounding atmosphere conducting to a damping effect. Interestingly, the damping seems to evolve almost linearly with SoD at low pressure, while it is less pronounced, at least for low SoD, at high pressure. This can be interpreted by a more efficient transfer of energy in terms of amount of motion between the gas flow and the particles at high pressure delaying the damping effect by the surrounding atmosphere. All together, in the parametric field we studied, the accessible velocities ranged from 250 m·s^{-1} to 600 m·s^{-1}. Concerning GA and SA powders, we could not observe any significant differences of the damping effect, except at high pressure and high SoD for which the damping seemed to be more important for SA. However, it remained difficult to be interpreted since, due to the rather wide particles size distribution (the average size of particles were 65 μm with a standard deviation of 15 μm), the error on particles velocity was ≈100 m·s^{-1} given by the mass difference of the agglomerates.

3.1.3   Single agglomerate impact studied on FIB-SEM cross-sections

In order to understand the behaviour of single HAp agglomerates (GA and SA) at the impact, the gas temperature was kept constant at 250°C and different pressures were applied by a wipe-test on mirror-polished TA6V substrates. For these wipe-test spray experiments, low particles feeding rates (0.5 g ·m^{-1}) and high traverse speed (1 m·s^{-1}) were used.

As seen in Figure 3.14, all the elementary "splats" present similar particle–substrate behaviour despite the differences of velocities and granules nature. The particles seem to compact onto the surface due to the shock loading under high-strain rates, which can be correlated with the pores collapsing. For GA, which is a less cohesive powder, the pores collapsing is more obvious. It should be mentioned that the focus ion beam can alter the microstructure, especially in the case of GA, since GA presents a
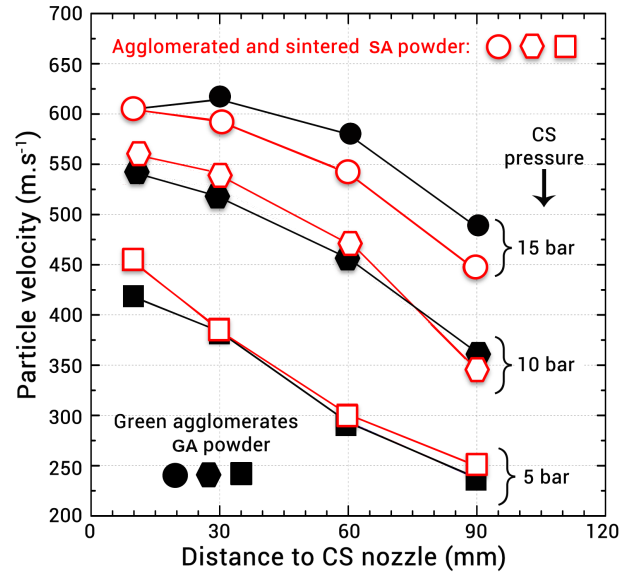
a) GA at $\approx$450m·s^{-1} **b)** GA at $\approx$550m·s^{-1} **c)** GA at $\approx$600m·s^{-1}

d) GA at $\approx$450m·s^{-1} interface   **e)** GA at $\approx$550m·s^{-1} interface   **f)** GA at $\approx$600m·s^{-1} interface

g) AS at $\approx$450m·s^{-1} **h)** AS at $\approx$550m·s^{-1} **i)** AS at $\approx$600m·s^{-1}

j) AS at $\approx$450m·s^{-1} interface   **k)** AS at $\approx$550m·s^{-1} interface   **l)** AS at $\approx$600m·s^{-1} interface
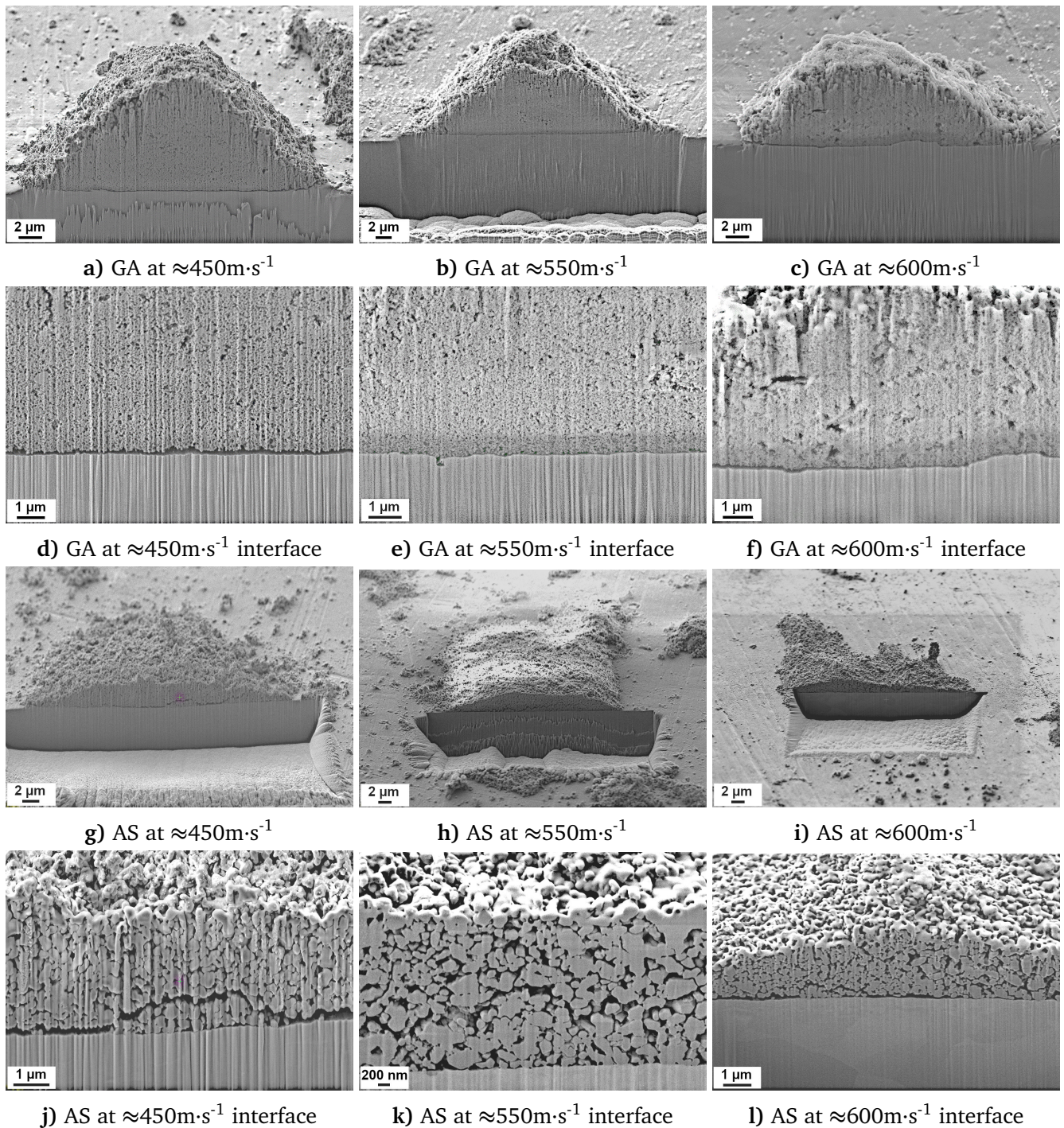
Figure 3.14 – *FIB-SEM cross-sectional images of : GA at a),b),c) low magnification and d),e),f) high magnification and SA at g),h),i) low magnification and j),k),l) high magnification on mirror-polished TA6V substrates.*

low crystallinity. However, most of the "splats" dimensions remain in the same order magnitude as the feedstock powders, with some fragments scattered around. In most cases, no cracks are visible except for SA at $\approx$550 m·s^{-1} for which the "slat" probably hit an area were some fragments were previously scattered. In this case, the splat followed the shape of the fragments.

In conclusion, both GA and SA agglomerates present similar consolidation mechanisms at the impact. The elementary particles included in the agglomerates are compacted upon shock loading but they do not really fragment themselves. The compaction ability is logically higher for the less cohesive GA powder, allowing for a greater mobility of the elementary particles of the agglomerates at the impact.
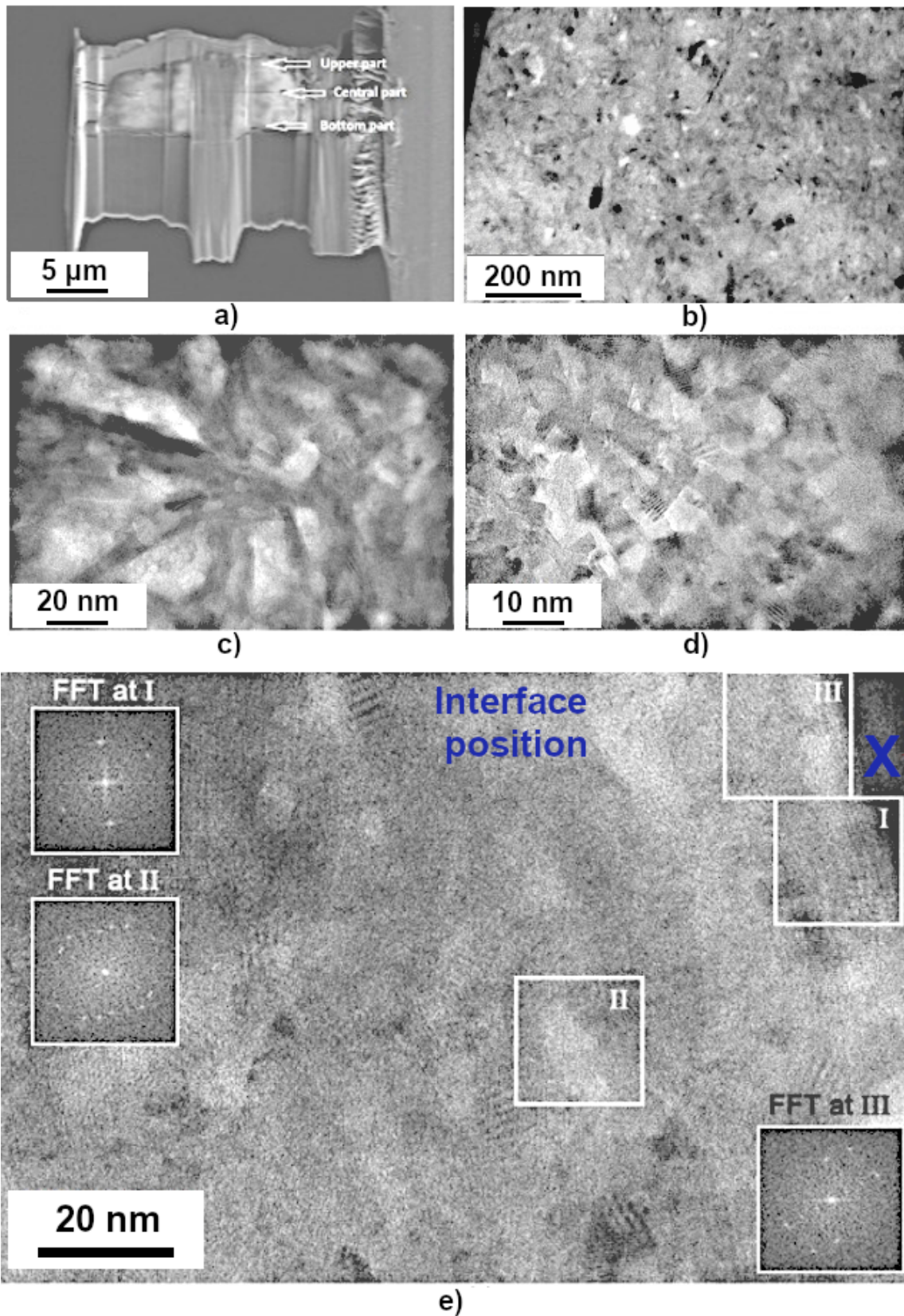
Figure 3.15 – *(a) FIB preparation of HAp splat on TA6V substrates. (b) TEM image representative of the whole splat, (c) upper, (d) central and (e) bottom part of the HAp splat [31].*

This trend was already observed during the loading-unloading cyclic compression tests performed on single agglomerates *in situ* in a SEM (Figure 3.10).

Our results were similar to what was reported in the literature. Cinca *et al.*[31] and Vilardell *et al.*[138] studied HAp "splats" at the impact under high-strain rates by TEM (Figure 3.15). Their studies showed that Moiré patterns were observed in the upper part of the coating, while the bottom part of coatings presented more effective consolidation due to the tamping effect produced by continuous impact of incoming particles. The powder and coating characterization confirmed that there was no amorphization of HAp and the microstructure was preserved. No size changes in nano-sized grains were detected by TEM.

3.2 Cold spray deposition of HAp coatings

Compared to other thermal spray techniques, in CS the feedstock powder remains in a solid-state phase as a consequence of low thermal input and high velocities. CS retains feedstock material properties in the coatings allowing to derive benefit of nanostructuration, crystallinity and phase composition [139]. To date, CS starts to be extensively studied and even industrially used for metals which undergo high strain-rate plastic deformation during the high-velocity impact and bond mainly by adiabatic shear instabilities (ASI) at the interfaces. Metallurgical bonds are confirmed by high electrical conduction [54]. In most cases, CS allows obtaining thick coatings and even additive manufacturing is possible [45]. In the case of ceramics, due to their inherent brittleness, their deposition remains a challenge and the bonding mechanism are still under debate. Some researchers suggests that the ceramic particles are mechanically anchored onto the substrate mainly by the plastic deformation of the metallic substrate with particles fracturing [67, 68]. Yamada *et al.*[14] them reported on the elaboration of thick TiO_2 coatings onto metallic substrates, highlighting the chemical bonding rather than mechanical anchoring. Various factors come into play regarding the bonding mechanisms such as the feedstock powder, the particle-substrate hardness ratio and the substrate topography. These factors are already well recognised to drive the deposition mechanisms for metals as shown in Figure 1.12. However, in the specific case of brittle ceramics, in most cases the build-up of thick and highly adherent coatings fails, resulting in only a single monolayer of particles embedded into the substrate surface, or in thicker coatings but with low adherence.

So far, "soft" ceramics can be successfully deposited by LP-CP. This is mostly due to the powder feeding injection system which is axial and downstream compared with HP-CS for which the powder injection is generally radial and upstream as shown in Fig.2.36. In our study, different trials were firt done with classical HP-CS using a radial injection (schematic show in figure**??**), without real success (data not presented), mostly due to the interrupted (pulsed) feeding and fast injector clogging even at low feeding rates (nozzle clogging after less than 5 minutes). We then switched to axial injection for which the feeding rate can be more stable. As a result, the coatings become more homogeneous, and the injector can operate for 20 to 30 minutes. The nozzle with an axial injection system is also easier to clean up in comparison with a radial injection). All the HAp coatings presented hereafter were fabricated using an axial injection system, as shown in section 2.3 Figure **??**. Since the CS ceramic coatings depend not only on the process parameters but also on the feedstock powder and substrate characteristics, we considered all these parameters in our experiments. In order to understand the effect of the feedstock powder on CS, two types of hydroxyapatite powders were chosen: green and sintered agglomerates (GA and SA as presented in the subsection 2.1.2) and deposited onto 3 types of TA6V substrates with different surface properties: substrates preliminary grit blasted (TA6V), laser surface textured substrates (LST-TA6V described in subsection 2.2.3.1) and substrates exhibiting a CP Ti Grade 2 sublayer (Ti grade 2). The CS conditions were first optimised with grit-blasted TA6V substrates. The grit blasting was performed in 2 steps with F16 ($\approx$1.2mm) followed by F80($\approx$0.18mm) alumina. The primary purpose was to create macro and micro craters that could help mechanical anchoring. All the substrates were ultrasonically cleaned up in acetone followed by ethanol prior to deposition. The substrates were fixed on a holder and the gun was moved by a KUKA robot on X–Y directions at a typical traverse speed of 0.01 m·s^{-1}. Several individual tracks with different separation distances between them were used to cover homogeneously the substrates surface. Nitrogen was employed as the carrier gas.

Since our CS Impact 5/11 system was designed to operate at high pressure, the minimum stable pressure we could practically use was 0.5 MPa together with a maximum carrier gas temperature of 250°C. Also, to obtain homogeneous coatings, the particles velocity had to be lower than 550 $m \cdot s^{-1}$ which required, for a pressure of 0.5 MPa and a temperature of 250°C, to work at a 200 mm SoD. This way homogeneous coatings could be obtained. Due to the divergence of the jet, the particles velocity was impossible to measure at 200 mm. We estimated it to be below $100 m \cdot s^{-1}$.

Chen *et al.*[32] suggested a possible HA deposition mechanism (Figure 3.18). After the first agglomerate covers the substrate by crushing/deformation, the second deposition step leads to the further compacting of the first HAp layer in the impact direction. It fills the voids of the first layer resulting in a compact deposition with a reduction of the porosity through tamping effect.

a) GA on TA6V   **b) GA on LST TA6V**   **c) GA on Ti grade 2**

d) AS on TA6V   **e) AS on LST TA6V**   **f) AS on Ti grade 2**

g) GA on TA6V   **h) GA on LST TA6V**   **i) GA on Ti grade 2**

j) SA on TA6V   **k) SA on LST TA6V**   **l) SA on Ti grade 2**
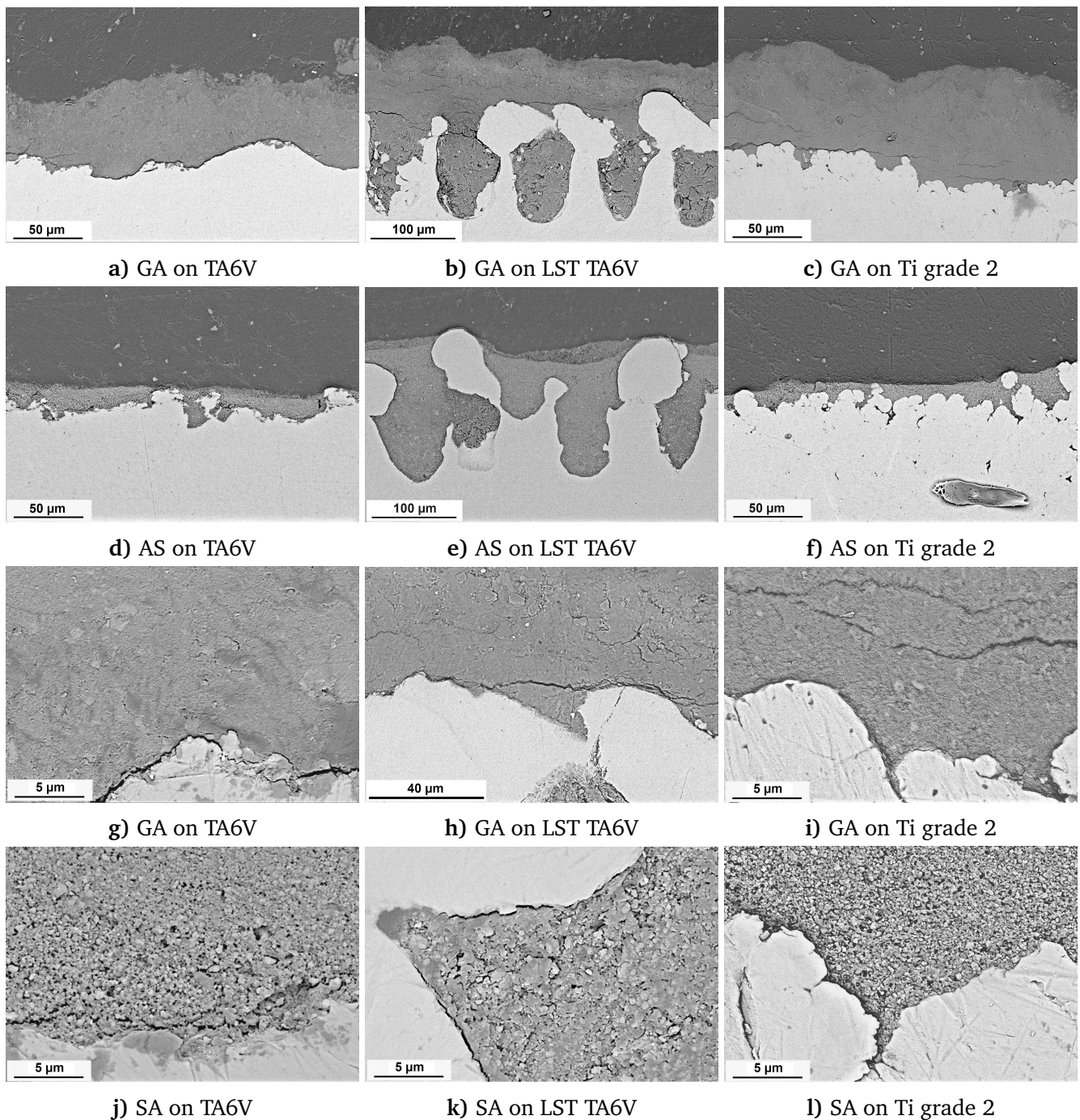
Figure 3.16 – *Cross-sectional BSE-SEM images of GA and SA coatings on various substrates.*

a) top view GA on TA6V   **b)** top view GA on LST TA6V   **c)** top view GA on Ti grade 2

d) top viewAS on TA6V   **e)** top view SA on LST TA6V   **f)** top view SA on Ti grade 2

g) top view GA on TA6V   **h)** top view GA on LST TA6V   **i)** top view GA on Ti grade 2

j) top view SA on TA6V   **k)** top view SA on LST TA6V   **l)** top view SA on Ti grade 2
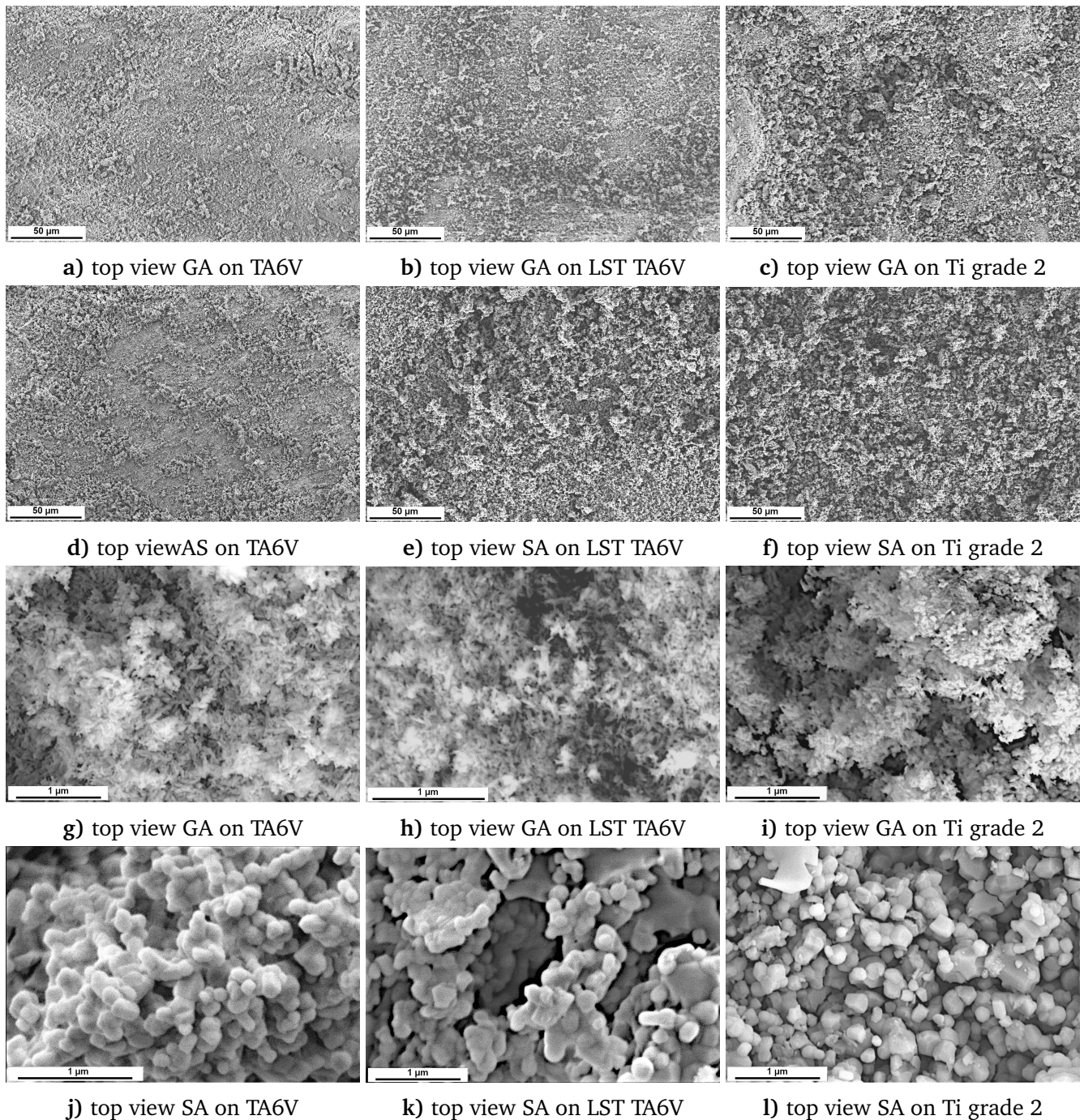
Figure 3.17 – *Top view SEM images of GA and SA coatings on various substrates.*

Figures 3.16 and 3.17 present the SEM images of cross-sections and surface morphologies, respectively, of HAp coatings elaborated by CS of GA and SA. GA being a less cohesive powder with a better compaction ability, the better resorption of the porosity of GA upon tamping is clearly observed in Figure 3.16, together with the ability to get thicker coatings for a given surface state.

The cross-sectional BSE-SEM images (3.16) show homogeneous microstructures with intimate coating-substrate interfaces and no apparent splat boundaries. The porosity initially observed in the feedstocks, especially for SA (see Figure 2.8 d)) is significantly reduced. This fact indicates a high compaction due to the tamping effect. Similar coating microstructures were reported in different papers [32]. The coatings based on GA present transverse cracks that can be attributed to the layer formation, that supports the affirmation of Chen *et al.* [32]. It supports the idea that the building-up process continues after the first layer is deposited by striking or hammering.

The deposition on laser textured substrates is a particular case. The coatings are the thickest obtained ones for a given powder feedstock. The texture seems to promote the mechanical anchor. Moreover some hidden substrate spots in the spraying direction are well-filled traducing the particles lateral mobility during the compaction and likely some rebound effects. So, compared to plasma spraying, CS allows covering complex surfaces regardless of their topography.
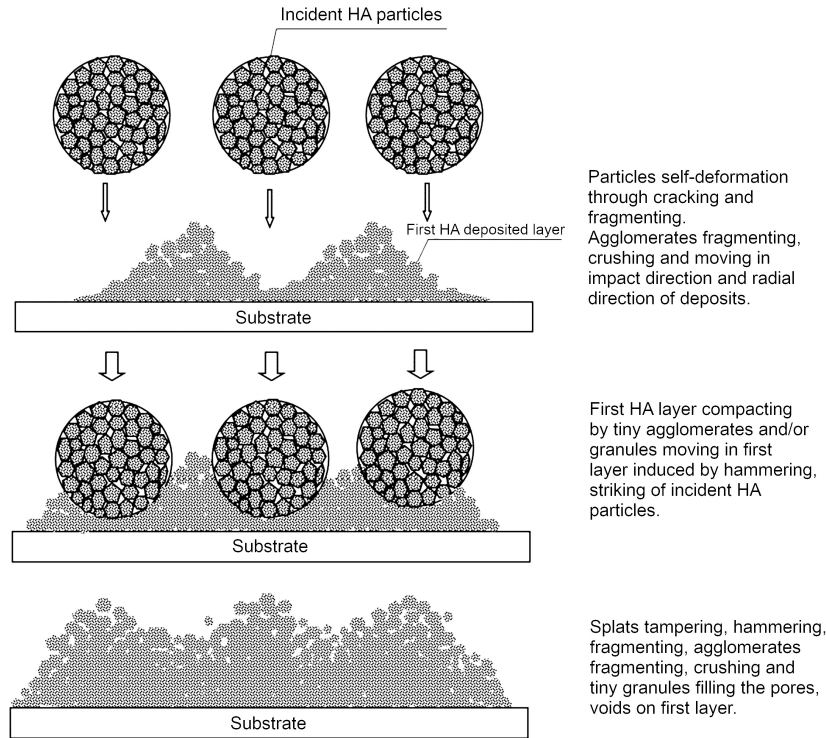
Figure 3.18 – *Schematic representation of HA coating formation by CS[32].*

As already mentioned, due to its compaction ability, GA leads to thicker coatings. For SA, the lower thickness can sometimes conduct only to a partial coverage of the substrates like those being laser textured. As illustrated by TEM images, GA agglomerates (Figure 2.7 a)) exhibit acicular grains (needle-like morphology), while SA agglomerates contain quasi-spherical particles (Figure 2.7 b)) with local triple boundaries. Even if the force and the displacement at rupture are quite similar between GA and SA, the triple boundaries in SA affect negatively the compaction ability, decreasing the thickness and the deposition

Figure 3.19 – *Macrophotos before and after compressed air cleaning of GA coatings on Ti Grade 2 for 200 mm SoD (0.5 MPa and 250 °C).*

efficiency from ≈12% for GA to ≈5% for SA. The Figures 3.17 a-f) show that the substrates are well covered. High magnification images point out that the coatings retained 100 % of the morphology of the feedstock powders. As a result, we can conclude that no significant thermal effects are activated during CS. At the SoD of 200 mm, the coatings are very homogeneous at the macroscopic level (Figure 3.19-left). Unfortunately, they exhibit a very poor adhesion since they cannot withstand compressed air cleaning (Figure 3.19-right). Again, this is a proof that the coatings are just mechanically anchored on the substrates through a close-packing of elementary grains, those grains having no chemical bonds in between them. The cohesion is only linked to the intergranular frictional forces.

Phase analyses of the HAp coatings by XRD

The comparative analyses of phase composition of the feedstock powders and associated coatings on various substrates were performed by XRD in the 25-55° 2θ range with a scan step of 0.19 °. The Figure 3.20 a) and Figure 3.20 b) show the XRD patterns of GA and SA feedstock powders and CS coatings. Both for GA and SA, the XRD patterns of coatings maintain similar peaks broadness as the corresponding feedstocks. Those peaks are however slightly shifted towards higher angular positions due to the presence of residual compressive stresses in the coatings. The peaks can be attributed, according to ICDD-9-0432, to synthetic HAp with an hexagonal lattice structure corresponding to the P63/m space group. Due to the low thickness of SA coatings, their XRD patterns show also a peak around 41° that is characteristic of the substrate.
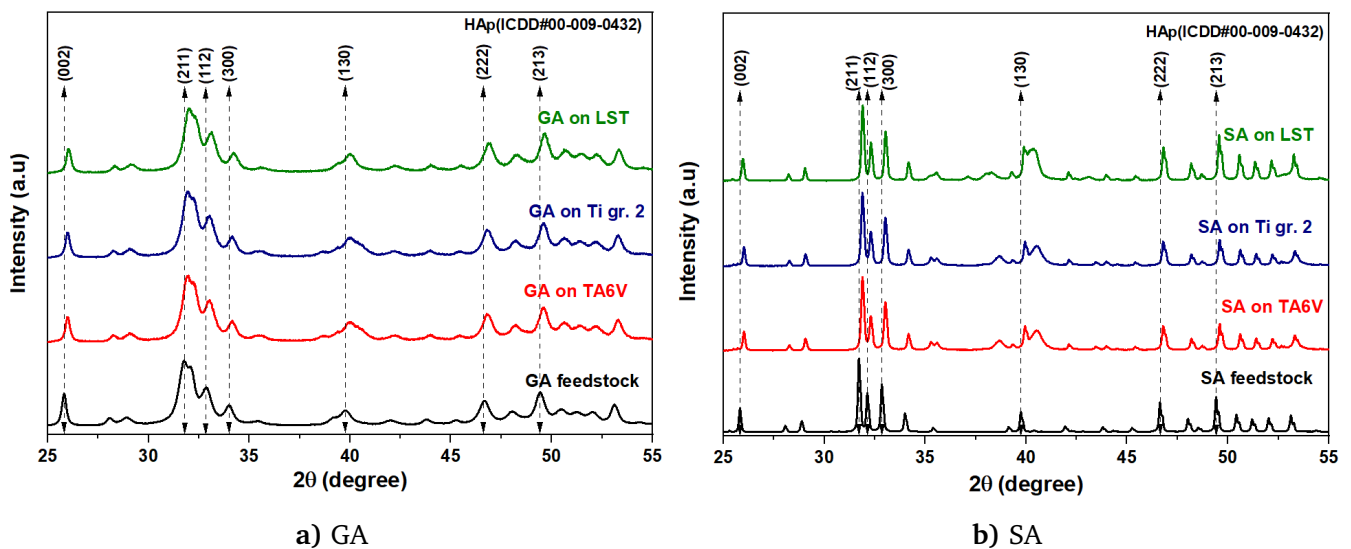
Figure 3.20 – *XRD patterns of a) GA and b) SA feedstock powders and associated coatings on various substrates (30 mm SoD, ≈450m·s⁻¹).*

The Table 3.1 summarizes the mean crystallite size (calculated using the highest intensity peaks indexed as 211, 112 and 300) of the feedstock powder and corresponding coatings on different substrates. It was calculated using the Scherrer equation 2.1. FWHM was obtained by gaussian fitting. Both GA and SA show a slight crystallite size decrease when coated, which can be linked to the effect of the substrate hardness. Consequently the highest decrease can be observed on the laser textured substrate which exhibits the highest hardness of 700 HV among the different types of substrates used, followed by TA6V and Ti grade 2 substrates.

Sample	SA feedstock	SA-LST	SA-TA6V	SA-Ti	GA feedstock	GA-LST	GA-TA6V	GA- Ti
D[nm]	49.8	41.5	44.1	44.2	14.4	9.9	10.5	10.9

Table 3.1 – *Crystallite size calculated for a) GA and b) SA feedstock powders and associated coatings on various substrates (30 mm SoD, ≈450m·s⁻¹).*

Characterization by attenuated total reflectance ATR-FTIR

Fourier transform infrared (FTIR) spectra were recorded in attenuated total reflectance (ATR) mode using germanium crystal (Nicolet Nexus, Thermo electron corporation, U.S.A.), with the idea to see if there was any significant thermal effect during the CS coating process. The ATR-FTIR spectra (Figure 3.21) of the feedstock powders (GA and SA) show the characteristic bands due to PO_4^{3-} ions (ν_1 963 cm^{-1}, $\nu3$—1036 and 1095 cm^{-1}, ν_4—568 and 600 cm^{-1}) and OH^{-1} groups (vibration mode at 630 cm^{-1}). Additionally, low intensity peaks at about 1400 cm^{-1} (ν_3) and 870 cm^{-1} (ν_2) can be linked to the absorbed CO_2 molecules at the agglomerates surface (more visible in the case of SA powder). No real change in the ATR-FTIR peaks are observed in the case of coatings suggesting that no significant thermal effect occurs at the impact at high velocity. Even if, at this stage, it is still difficult to tell exactly what the temperature elevation in the impact zone is, it is likely of the order of several hundreds of degrees Celsius. Deeper analyses would be necessary to get an exact value of this temperature elevation.
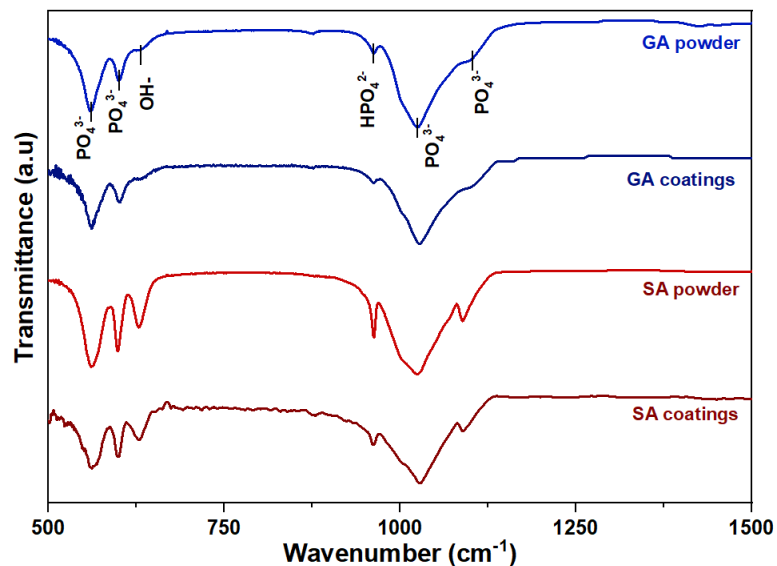
Figure 3.21 – *ATR-FTIR spectra of GA and SA powders and associated coatings deposited on Ti grade 2 at 200 mm SoD.*

Surface topography of the GA and SA coatings

The roughness of the coatings was measured by optical interferometry and 2 roughness parameters were determined, namely Ra and Rt (Table 3.2). In most of the cases, the HAp coatings follow the topography of the substrates making of CS a conformal deposition process, except for the laser textured substrates for which the large craters are completely filled. All together, the roughness differences between the various coatings elaborated are quite low with Ra values around 6 to 7 μm. The Figure 3.22 presents a few examples of the typical topography of as-sprayed coatings on different substrates.

	TA6V		LST		Ti gr.2	
	Ra(μm)	Rt(μm)	Ra(μm)	Rt(μm)	Ra(μm)	Rt(μm)
GA coatings	6.1	40.6	6.3	42.5	7.1	56.6
SA coatings	6.0	39.4	7.4	44.1	6.6	43.2

Table 3.2 – *As-sprayed coatings topography parameters.*

a) 2D Profile of GA on Ti grade 2

b) 2D Waviness of GA on Ti grade 2

c) 2D Profile of SA on Ti grade 2

d) 2D Waviness of SA on Ti grade 2

e) 2D Profile of GA on TA6V

f) 2D Waviness of GA on TA6V

g) 2D Profile of SA on TA6V

h) 2D Waviness of GA on Ti grade 2
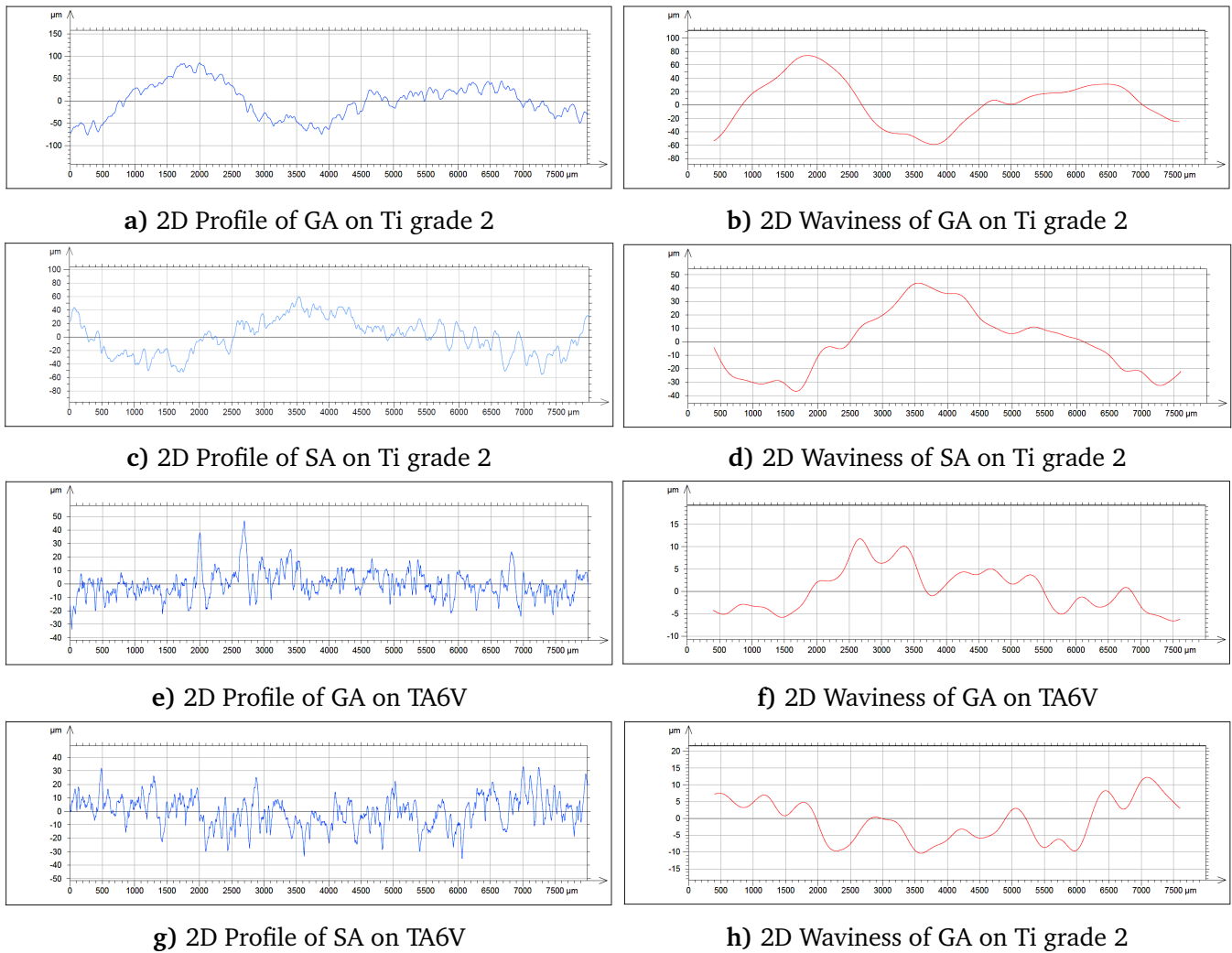
Figure 3.22 – *Typical topography of as-sprayed coatings on different substrates.*

Thermal post-treatment effects

Heat treatments can potentially mitigate the low coating adhesion (main drawback of CS ceramic coatings), as well as allow controlling the microstructure. The Figure 3.23 shows the 2 heat treatments we performed at 600°C and 1000°C with a 1°C·min⁻¹ heating rate and 1h dwell time, in Ar atmosphere to avoid the substrate oxidation. The GA coating exhibits small microcracks after the heat treatment at 600°C (Figure 3.28 a)), that are much more accentuated at 1000°C (Figure 3.28 c)) due to the initiation of sintering shrinkage. At higher magnification we see clearly the sintering of GA. At 600°C the GA coating maintains the same acicular grain morphology as the feedstock (Figure 3.28 b)) whereas grain are similar to SA at 1000°C (Figure 3.28 d)). The SA coating is much more stable upon the heat treatment at 1000°C with no cracks and no microstructure evolution (Figure 3.27).
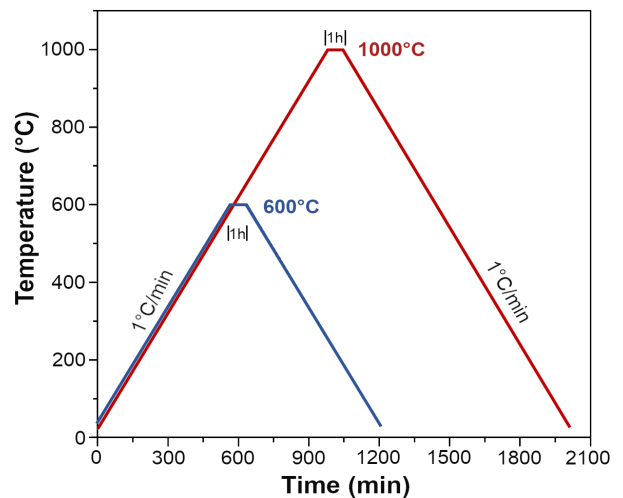
Figure 3.23 – *Thermal post-treatments in Ar used to improve the HAp coatings performance.*
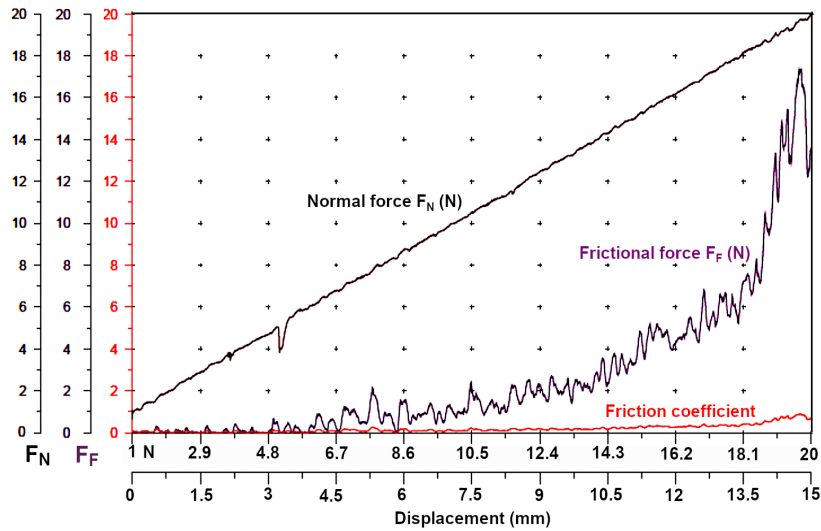
Figure 3.25 – *A typical scratch test data plot.*
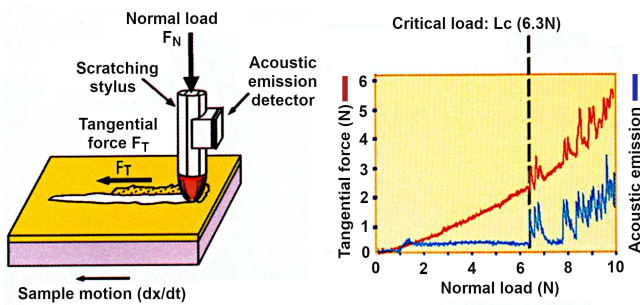
Figure 3.24 – *Principle of the scratch test.*

Scratch tests were carried out using a CSM micro-scratch tester in ambient atmosphere according to the ASTM C1624 standard. The scratch test principle is presented in Figure 3.24 and a typical data plot in Figure 3.25. It must be mentioned that this characterization technique does not allow a real measurement of the fundamental adhesion strength of the coating. It rather gives an extrinsic value, of interest on the practical point of view of the engineer, representative of that adhesion strength. The following scratch test parameters were used : progressive loading from 1 N up to 20 N at a loading rate 20 N·min⁻¹, total scratch length of 15 mm, 200 μm indenter (diamond stylus of Rockwell type). Five scratch tests were performed on each sample. The average results are given in Table 3.3. the standard deviations are not indicated in the table, but the results show that the adhesion strength is very low in all cases (a few Newtons), even if it increases a bit, as expected, when laser textured substrates are used or when a post heat treatment is applied. Anyway, the low level of adhesion remains really the major drawback of our CS coatings. This is actually the main issue to be solved in the future for potential applications.

a) Initial point   **b)** Intermediate point   **c)** Final point
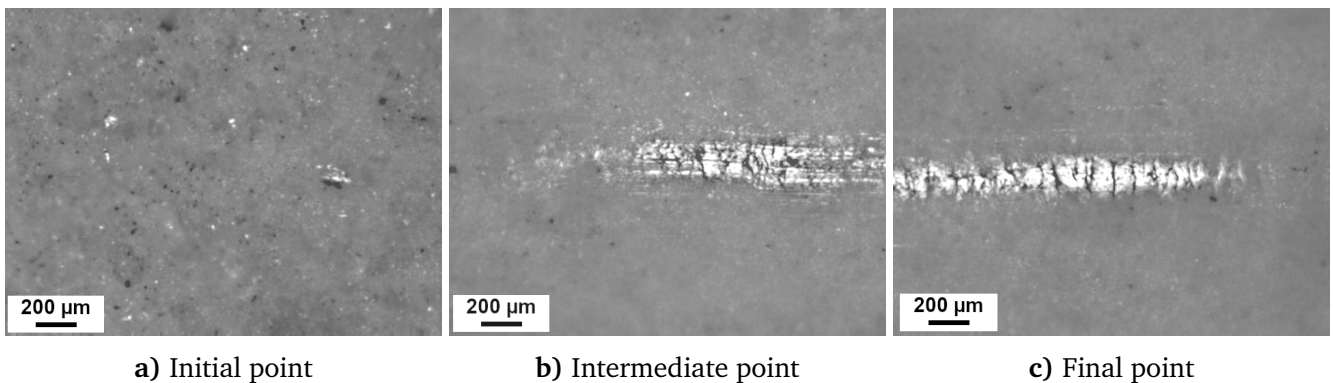
Figure 3.26 – *Typical SEM images of a path of a scratch on a GA coating at a displacement rate of 0.5 μm·s⁻¹: (a) before compression, (b) during compression and (c) after compression.*

	Critical load Lc (N)			
	Substrate	SoD(mm)	GA	SA
As-sprayed	Ti grade 2	3	<1 N	<1 N
	LST	3	1.2 N	1.1 N
Heat treated at 600°C	Ti grade 2	200	2.3 N	2.6 N
	LST	200	4 N	4.2 N
Heat treated at 1000°C	Ti grade 2	200	N.A.	3.2 N
	LST	200	N.A.	7.1 N

Table 3.3 – *Lc values for as-sprayed GA and SA coatings and post heat treated at 600°C and 1000°C on various substrates.*

a)   b)
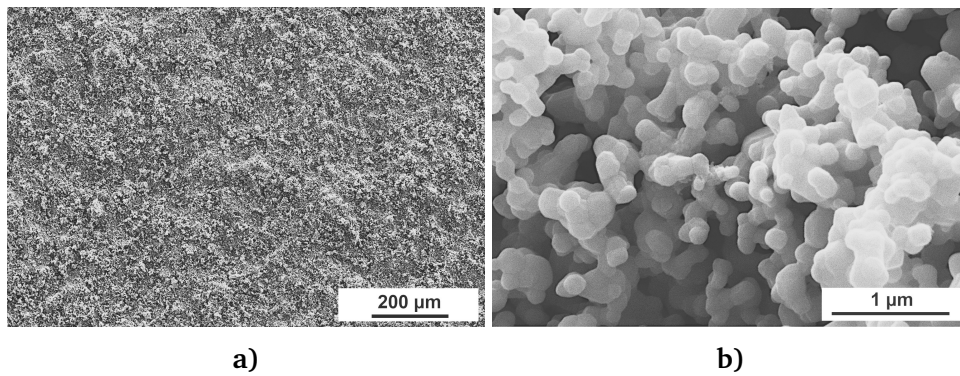
Figure 3.27 – *Top view SEM images of a SA coating on a Ti Grade 2 substrate at 200 mm SoD and post-heated at 1000°C.*

c)   d)
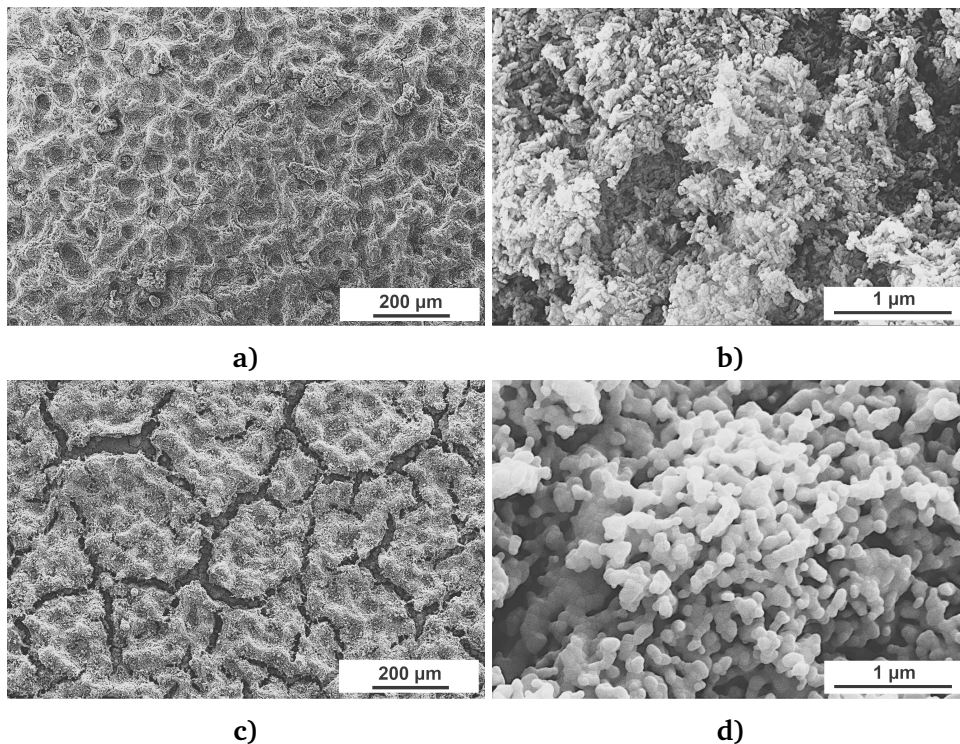
Figure 3.28 – *Top view SEM images of a GA coating on a Ti Grade 2 substrate at 200 mm SoD and post-heated at 600°C (a,b) and 1000°C (c,d).*

3.3 Novel HAp-based hybrid coatings with enhanced bio-activity

By far, plasma spraying is the most industrially used technique for the deposition of HAp coatings. APS or VPS can be easily employed to fabricate coatings with thicknesses ranging from a few tenth of microns to millimeters. The powder is injected in the plasma, melted (or partially melted) and propelled toward the substrate. Unfortunately, due to the high temperature used during deposition, HAp can suffer undesirable phase transformation and the shaping process can cause residual thermal stresses in the coatings. Even if HAp bioceramics possess good biocompatibility and high osteoconductivity, they also present some weaknesses: especially a lack of sufficient osteoinductivity to induce osteogenic formation of new bone, which is crucial for the regeneration of large bone defects and bone tissue engineering.

To overcome the osteoinductivity issues, this thesis proposes to develop hybrid composites based on collagen-HAp and bioglass-HAp. As shown before, CS allows maintaining all the structural and chemical features, such as the grain size and chemical composition. The possibility offered by CS to use thermal-sensitive osteoinductive materials in combination with a high productivity makes of CS a technology of great interest.

Another issue addressed in this thesis is to combat the health complication associated with postoperative infections caused by antibiotic-resistant bacterial strains. Silver, especially in nanometer size, demonstrates an effective way to strike against antibiotic-resistant bacteria. Since CS deposition operates low temperatures, this technology can be successfully used to deposit thermal-sensitive material containing silver nanoparticles without any coalescence of those nanoparticles upon thermal effect, thus keeping their good antimicrobial properties.

3.3.1 Anti-microbial and anti-infective Ag-HAp based coatings by CS

To date, one of the most common strategy for preventing infection and minimize contamination during surgery and post-operative interventions is antibiotic prophylaxis. Unfortunately, in the last decade, the efficacy of antibiotics decreased due to the appearance of antibiotic-resistant bacterial strains. The estimated risk of infection of an implant after a total replacement surgery is fairly low, 0.5–5%, but the consequences are very serious. Ag demonstrates to be effective over a broad spectrum: antibacterial, antifungal and antiviral. Compared with other metal ions, Ag has shown high antimicrobial activity while maintaining relatively low cytotoxicity. As a

Figure 3.29 – *XRD patterns of Ag@HAp feedstock and associated coating.*

result, research on Ag nanoparticles has become an emerging field in recent years [117, 74].

The previously synthesized Ag-functionalized GA powder by PVD for 90 minutes was used to develop our antimicrobial coatings, labeled as Ag@HAp. These coatings were prepared as mentioned in the subchapter 3.2 on Ti grade 2 at 200 mm SoD.

a)

b)
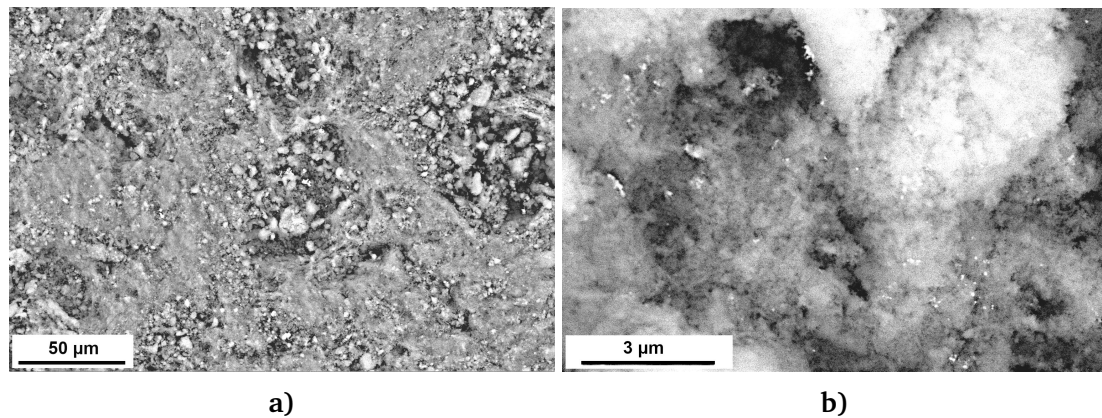
Figure 3.30 – *Top view SEM images of Ag@HAp coatings fabricated on Ti grade 2 at 200mm SoD.*

a)

b)
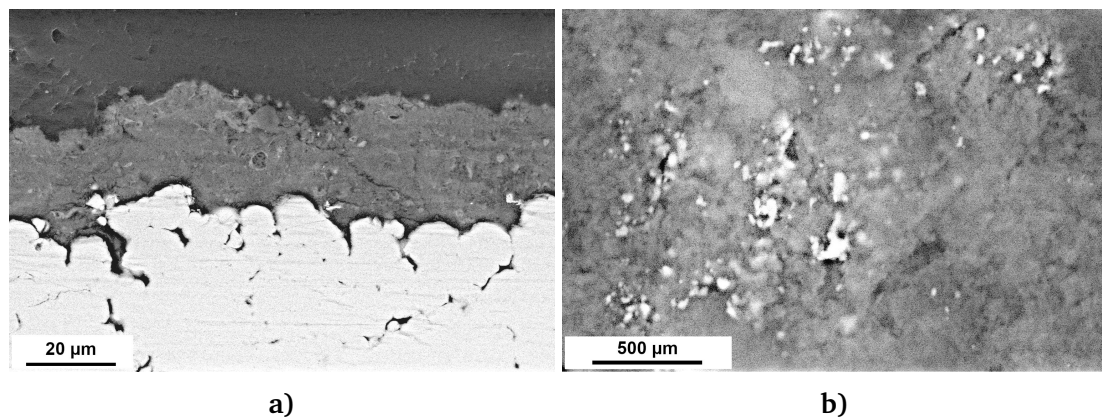
Figure 3.31 – *Cross-sectional SEM images of Ag@HAp coatings fabricated on Ti grade 2 at 200mm SoD.*

The Figures 3.30 and 3.31 present the top view and cross-sectional SEM images of the as-obtained Ag@HAp coatings, respectively. At high magnification, the acicular HAp grains and the spherical Ag nanoparticles are visible (white contrast). No real change are observed in comparison to undoped GA coatings produced in the same conditions. By using Rietveld refinement analyses (HighScore Plus software) on the XRD spectrum, it is shown that the Ag content is kept at the same level in the coating as it is in the feedstock powder, namely 5.4 at.%. The Ag nanoparticles are quite homogeneously distributes in the volume of the material, knowing that only those located in the vicinity of the coating surface will be useful for the antimicrobial purpose.

3.3.2 Bioinspired collagen-hydroxyapatite hybrid coatings

The Coll@HAp coatings with 5 and 10 wt.% collagen (Figures 3.32 and 3.33) were fabricated like the Ag@HAp coating. The ATR-FTIR spectra (Figure 3.34) show the presence and retention of collagen and hydroxyapatite after CS deposition. All the major characteristic stretching peaks of collagen are present (amide I- C=O, amide II- N-H, and amide III- C-N in the regions of 1636-1661 cm^{-1}, 1549 - 1558 cm^{-1} and 1200 - 1300 cm^{-1}), which validates the conservation of the integrity of the proteins in the composition of collagen molecules. The peaks become sharper with the increasing collagen concentration. Concerning the HAp characteristic peaks of tetrahedral PO_4^{3-}, they are observed at 563, 603, 962 and 1033–1091 cm^{-1}. The 2 peaks at 563 and 603 cm^{-1} correspond to the PO_4^{-3} ν_4 mode. The peak at 962 cm^{-1} is for PO_4^{-3} ν_1 and the peaks at 1033–1091 cm^{-1} are due to PO_4^{3-} ν_3.
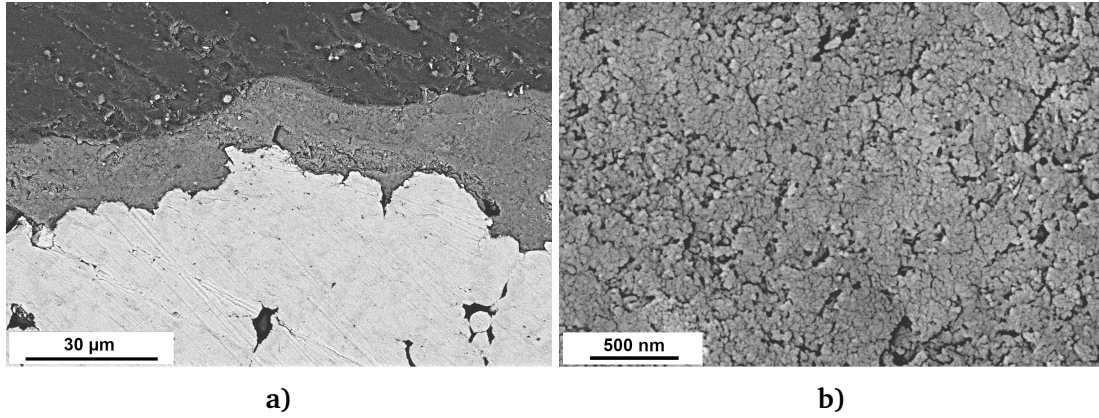
Figure 3.32 – *Cross-sectional SEM images of 5 wt.% Coll@HAp coating fabricated on Ti grade 2 at 200 mm SoD.*
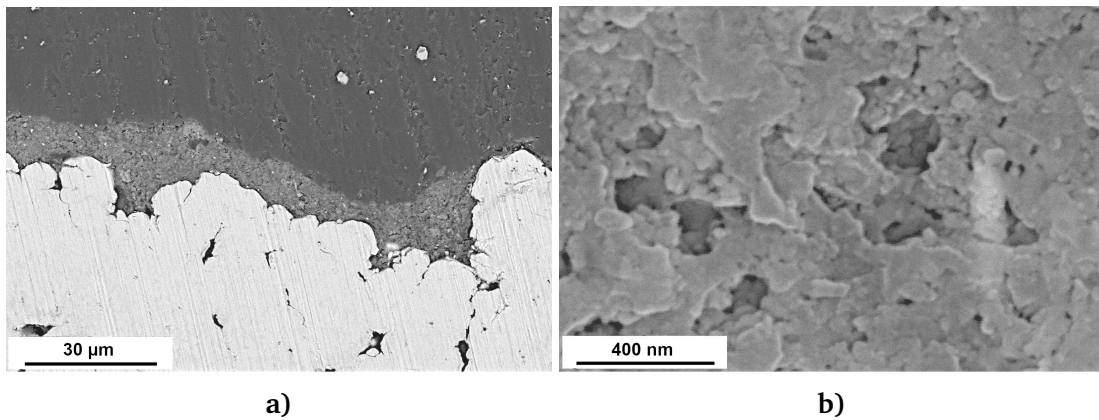
Figure 3.33 – *Cross-sectional SEM images of 10 wt.% Coll@HAp coating fabricated on Ti grade 2 at 200 mm SoD.*
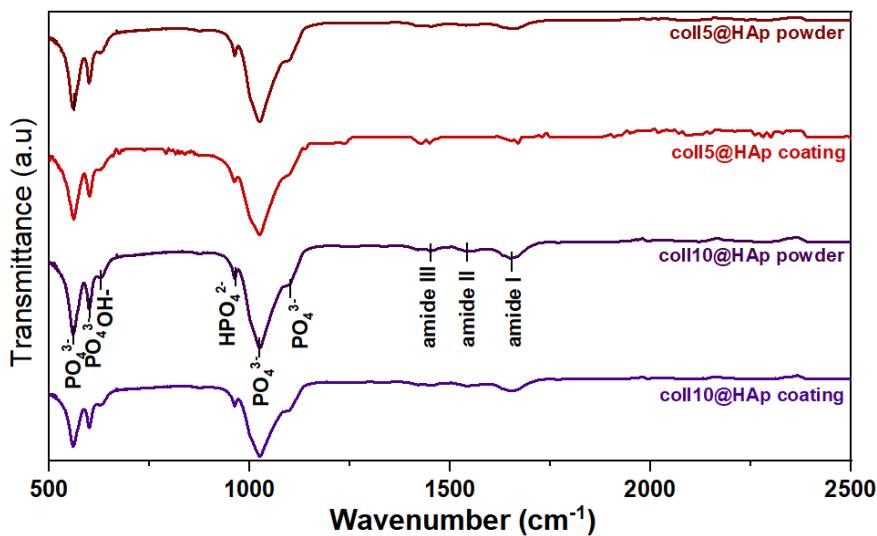
Figure 3.34 – *ATR-FTIR patterns of COLL5@HAp and COLL10@HAp powders and deposited on Ti grade 2 at 200mm SoD.*

3.3.3 Bioglass-HAp hybrid coatings

The Bioglass@HAp coatings with 5 and 10 wt.% bioglass (Figures 3.31 a)and 3.36) were fabricated like the Ag@HAp and Coll@HAp coatings. Because of the bioglass amorphous nature and its IR signature similar to HAp, XRD and FTIR analyses failed to reveal specific peaks of feedstocks and coatings, respectively. As it can be clearly observed from Figure 3.35 b), the bioglass initial blocks do not really fragment at the impact. They are just embedded and dispersed in a matrix of GA elementary grains after compaction. The coating consolidation is only due to to a mechanical anchor through particles packing. The blocks of bioglass being much larger than the GA elementary particles, the packing is promoted by the bimodal size distribution and quite thick coatings can be obtained.

The extreme surface chemical compositions of the bioglass@HAp powders and coatings were analysed by XPS. The homogeneity of these surfaces was demonstrated through similar signals registered on three randomly selected regions. As observed in the Figure 3.37 a), the typical elements that compose the hybrid coatings, Ca 2p, P 2p, Si 2p, Na 1s, and O 1s are present. Some representative high resolution XPS spectra are presented in Figure 3.37 b) for Si 2p and Na 1s. In the Table 3.4 the quantification of the elements, calculated from the XPS analyses, is given. Basically, the coatings chemical composition is similar to that of the feedstock powders. The Si 2p photoelectron spectra of the BG10@HAp coating and powder show enhanced intensities due to the higher bioglass content.

a)   b)
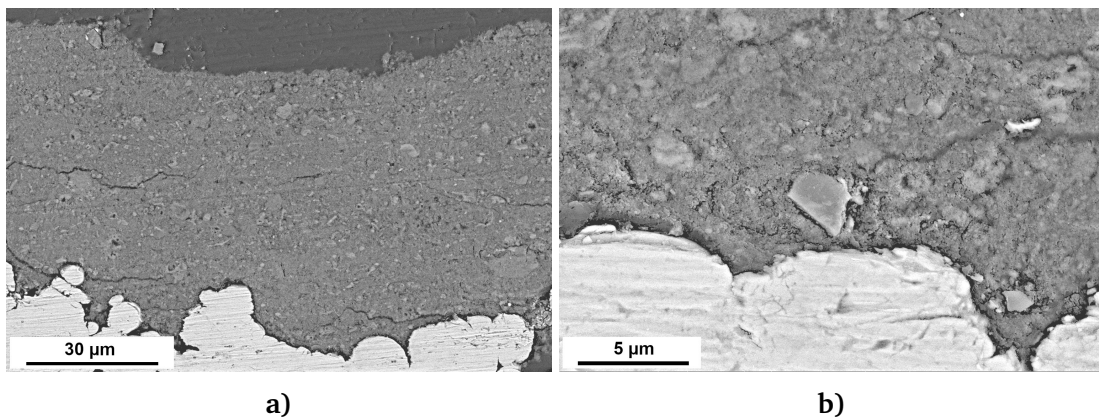
Figure 3.35 – *Cross-sectional SEM images of 5 wt.% Bioglass@HAp coating fabricated on Ti grade 2 at 200 mm SoD.*

a)   b)
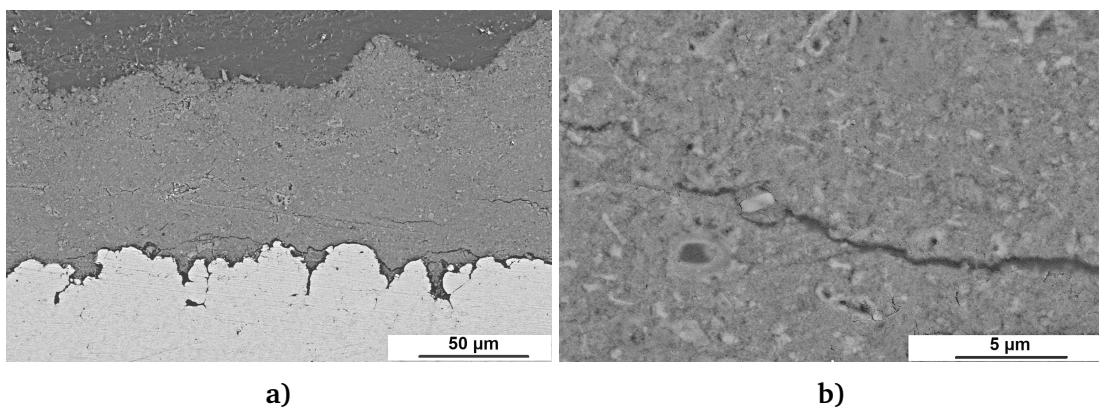
Figure 3.36 – *Cross-sectional SEM images of 10 wt.% Bioglass@HAp coating fabricated on Ti grade 2 at 200 mm SoD.*
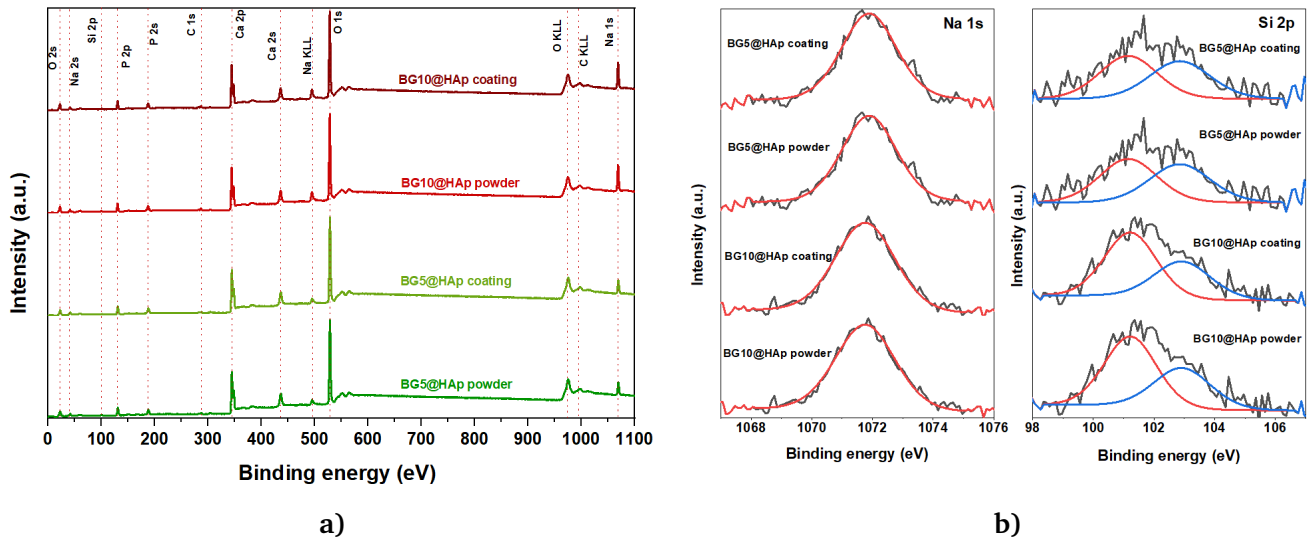
Figure 3.37 – *XPS spectra of 5 wt.% and 10 wt.% Bioglass@HAp feedstock powders and coatings fabricated on Ti grade 2 at 200 mm SoD.*

	Na 1s [%]	O 1s [%]	Ca 2p [%]	C 1s [%]	P 2p [%]	Si 2p [%]
BG5@HAp powder	5.5	63.2	17.5	3.9	9.1	0.8
BG5@HAp coatings	5.4	63.3	17.4	3.8	9.2	0.9
BG10@HAp powder	10.0	60.2	15.3	5.2	8	1.3
BG10@HAp coatings	9.9	60.6	15.4	5.0	7.8	1.3

Table 3.4 – *Atomic contents (calculated from the XPS analyses) of the elements present in BG5@HAp and BG10@HAp feedstocks and coatings.*

3.4 Conclusion - Chapter 3

In this chapter we first demonstrated the feasibility of the fabrication of HAp-based coatings by CS. In a second step, we extended the approach to the fabrication of hybrid coatings while including various "dopants" (*i.e.* silver nanoparticles, collagen, bioglass) for enhanced bioactivity and antimicrobial properties. In both cases, the microstructures of the feedstock powders were kept constant while deposited by CS in terms of elementary grain size and morphology, as well as chemical composition and cristallinity. Only a fragmentation of the initial agglomerates was observed, but not of the elementary particles included in them. These latter ones were just compacted upon multiple successive impacts, the compaction (*i.e.* the resorption of the porosity) decreasing when the cohesion of the upstream agglomerates increased, thus reducing the mobility of the elementary particles at the impact. This particle mobility at the impact allowed covering very complex substrates topography such as laser textured surfaces with the capability to fill even hidden "spots". In any cases, the compaction was responsible for the coating consolidation through mechanical anchor resulting from the particles interlocking in the granular compact. However, in the absence of real chemical bonding, the adhesion onto the substrates was very poor, even after some post heat treatments.

Chapter 4 : *In vitro* biological properties of the CS coatings

Overview ───

This last short chapter is devoted to the biocompatibility evaluation of the hydroxyapatite and hybrid composites coatings previously obtained by CS, in view of possible applications in the BTE field. The biocompatibility evaluation for BTE purpose is a complex analysis, influenced by the structural and functional characteristics of samples, but also the biological assessment technique itself (*i.e.* sterilisation methods, nature of bone cells or tissues, reproducibility of the tests). Here, our biological studies aimed more specifically at exploring the influence of different HAp-based coatings (samples presented in Chapter 3) on the viability of osteoblast cells growth and their proliferation patterns.

4.1 Introduction

Biocompatibility and osseointegration are two key factors that need to be considered to validate the quality of a biomaterial devoted to medical implants for BTE applications. Multidisciplinary collaborations between engineers, materials scientists, biologists, and clinicians already established advanced strategies in using different biomaterials to find solutions to regenerate through implants large trauma, to cure diseases or to compensate for the ageing of bones (*e.g.* osteporosis) [140, 141].

Whatever the synthetic material implanted in the body, it has to be biocompatible so that no inflammatory tissue reaction occurs. As a bioactive element, the general purpose of an orthopaedic device is to stimulate the bone regeneration. The implanted material is also expected to keep its integrity by withstanding physiological media without dimensional changes, brittle fracture or unexpected breaking in the long-term coming from fatigue under stress and/or corrosion. The biocompatibility evaluation of coatings, for instance, depends on various factors such as: (1) the materials type and composition, (2) the structural and functional characteristics of these materials, (3) their processing methodologies, (4) the sterilisation techniques, (5) the interaction with cells, (6) the hypothetical interferences between the cells and the host and (7) the reproducibility, sensitivity, and linearity of the analysis [36].
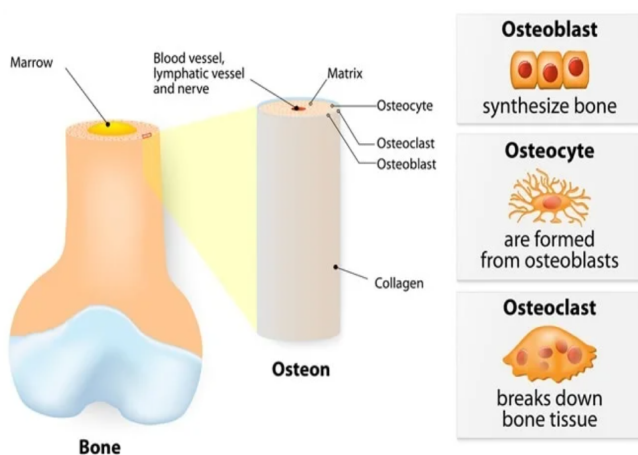
Figure 4.1 – *Bone structure and the important cells located in the osseous tissue.*

Apart from the surface chemistry, the coatings topography also affects the cell behaviour in terms of cell adhesion, activation, proliferation, alignment and orientation. Besides, *in vitro* tests ensuring the growth of cells on the surface of tested materials are not fully reliable because they cannot completely reflect the implant *in vivo* responses. Nevertheless, *in vitro* is the first unavoidable step for the testing of the biomaterial surface effects on cell functionality. After developing biomaterials at the laboratory level, the transfer to durable, reproducible and certified products is a very rigorous process that involves multiple clinical trials [142]. To form an ideal environment of the implanted bone, the used biomaterial, with or without bioactive coatings, needs to provide a cellular reaction and colonisation by osteoblasts. These processes will lead to osteoconduction. The bone grows on the implant forming the bound and promoting a functional interface [43, 37, 143]. Another factor is the type and magnitude of the applied external mechanical load since the bone adapts its microstructure as a function of this load. Osteoblasts, which are the bone-forming cells, are used as template for mineralisation, synthesis and formation of bone matrix at the early stage of reconstruction. These cells also participate in the adjustment of phosphate and calcium proportions in and out of the bone tissue. Alkaline phosphatase preparations supply in abundance the active osteoblasts. Exhibiting a cuboidal morphology in their active state, two potential behaviour can be predicted for the future of these osteoblasts: i) becoming bone lining cells and osteocytes or ii) degenerating and undergoing an apoptosis. So, osteoblasts are really the mediators for new bone formation, while bone resorption is mainly dependent on osteoclasts (Figure 4.1) [36].

4.2   Cell viability and proliferation studies

Cell viability and cytotoxicity tests are used to determine metabolic or cellular changes linked to viable or non-viable cells. These assays are very useful to detect structural variations such as loss of membrane integrity upon cell death or physiological and biochemical activities indicative of living cells [144].

Cytotoxicity assays are a type of *in vitro* tests employed to determine if the implant part will cause cell death because of leaching toxic substances or direct contact with surface. When a new biomaterial is integrated in a specific implant design, this toxicology test combined with a methodological approach is devoted to evaluate if the required biocompatibility criteria are met before performing further in-depth *in vivo* analyses. Indeed, it is essential to know how many viable cells remain at the end of the experiment regardless of the type of cell-based assay being used.

The Food and Drug Administration (FDA) guidance and other international standards advise the researcher to follow the ISO 10993-5 standard, "*Tests for Cytotoxicity—in vitro Methods*", to assess *in vitro* cytocompatibility for medical implants. This standard specifies the incubation of culture cells in direct contact with parts of the medical implants [145].

MTT test

The quantitative evaluation of cytotoxicity can be made through a colorimetric method involving a tetraziolum based salt whose abbrevation is MTT: the 3-(4,5-dimethylthiazol-2-yl)-2,5-diphenyl-2H-tetrazolium bromide. Developed by Mosmann in 1983 and considered to be the "gold standard" for cell viability and proliferation studies [36], the so-called MTT test consists in dosing by a catalysis reaction viable cells with MTT through mitochondria acting as a biological marker [146]: the added yellow-coloured MTT enters into mitochondria of a cell where it is reduced to a formazan precipitate by reaction with mitochondrial succinate dehydrogenase (Figure 4.2). The insoluble purple formazan is impermeable to the cell membrane and accumulates in healthy cells. To solubilise and extract formazan from the living cells, the solution is treated with isopropanol. The optical density (OD) of resulting solubilised formazan is evaluated by absorbance spectrophotometry technique at 490 nm. Obtained OD values are directly proportional to the number of metabolically active cells in the culture able to be determined with a straight calibration curve. High OD values signifies a high concentration of viable cells in the studied biological culture.

LDH test

Another cytotoxicity conventional method is the lactate dehydrogenase (LDH) test consisting in the evaluation of the cell membrane viability. In this test, the lactate dehydrogenase, which is a soluble cytosolic enzyme, is released in the extracellular medium when the cells are dead because of the damage to their plasma membranes (Figure 4.2). So LDH concentration is indirectly measured and quantified. In this way, a testing solution containing L-lactate, diaphrose, tetrazolium salt INT (2-(4-iodophenyl)-3-(4-nitrophenyl)5-phenyl-2H-tetrazolium chloride) and nicotinamide adenine dinucleotide (NAD$^+$) is added to the cells. The NAD$^+$ is reduced into NADH in the presence of L-lactate through the catalysis reaction of LDH. The tetrazolium salt INT is then reduced into a red formazan produced by NADH. As for MTT test, the red formazan proportion can be determined by absorbance spectrophotometry at 490 nm [146]. A low detected optical density (OD) indicates a low activity of LDH in the extracellular medium, and as a consequence, a high cellular viability.

To summarize, a great cellular viability is highlighted by: i) high OD values for MTT test and ii) low OD values for LDH test.

Experimental procedure used in this work

In order to perform such previously described citotoxicity tests, the CS samples were subjected to different successive steps. They were first sterilised overnight by exposure to the UV light. The preliminary assessments related to materials biocompatibility were performed through indirect contact assay with the stabilised Vero cell line of fibroblasts isolated from a monkey kidney. The procedure consisted in maintaining the tested materials in a well-known Eagle's minimal essential medium (EMEM) for 24 hours at 37°C, according to ISO10993-5. This is a cell culture medium developed by Harry Eagle and used for the supply of nutritive elements required for *in vitro* cell proliferation. The ratio of surface area

Figure 4.2 – *3D cross-section of a cell highlighting the different elements of its structure.*

to medium volume was 3 cm^2·mL^{-1}. The extraction medium was then collected and added to Vero cells culture, grown for 24 h in EMEM supplemented both with 10% of fetal bovine serum (FBS) and 1% of antifungal antibiotic (penicillin/streptomycin) at 37°C in a wet atmosphere with 5% CO$_2$. After 24 h, the cytotoxic potential of the extraction medium and the metabolic activity of viable cells were analysed using the LDH and MTT assays (Figure 4.3). The cytotoxic solution was prepared by EMEM with 5% of DMSO. This solution was used as a positive control, and the Vero cell-specific culture medium was used as a negative control. After incubating the cells with the appropriate culture medium, the cell monolayer was examined by phase-contrast microscopy (Figure 4.4).

Results

The cytotoxic potential of different CS coatings was investigated by testing the effect of the extraction media on the Vero cell line, through MTT and LDH assays. Various grades of materials referenced as SA (Sintered Agglomerates of hydroxyapatite), GA (Green Agglomerates of hydroxyapatite), Ag@HAp (silver with hydroxyapatite), BG5@HAp (5 wt.% of bioglass combined with hydroxyapatite), BG10@HAp (10 wt.% of bioglass combined with hydroxyapatite), COL5@HAp (5 wt.% of collagen combined with hydroxyapatite) and COL10@HAp (10 wt.% of collagen combined with hydroxyapatite) were compared both to the negative control medium (CTRL) and to the great positive cytotoxic conditions (MEM+5%DMSO). As it can be observed from Figure 4.3 a), LDH-OD values related to tested CS specimens so as CTRL reach a value close to 1.1 testifying the viability of cells. Note that SA (Sintered Agglomerates of hydroxyapatite) sample exhibits the greatest value. In comparison, the culture in a highly cytotoxic environment induces a drastic reduction of the viable cells treated with the 5% DMSO: LDH-OD value is almost divided by a factor 3. In addition, results of MTT tests are reported in Figure 4.3 b). All the average MTT-OD values ranging between 0.105 to 0.125 are close to those obtained in the negative control medium CTRL. Under strongly positive cytotoxic conditions (EMEM+5%DMSO), a significant increase of MTT-OD value reaching about 0.2 can be observed, emphasising the existence of an increased number of cells with a destroyed membrane. These results show once more that the analysed surfaces of all tested CS specimens exhibit a low cytotoxic potential.
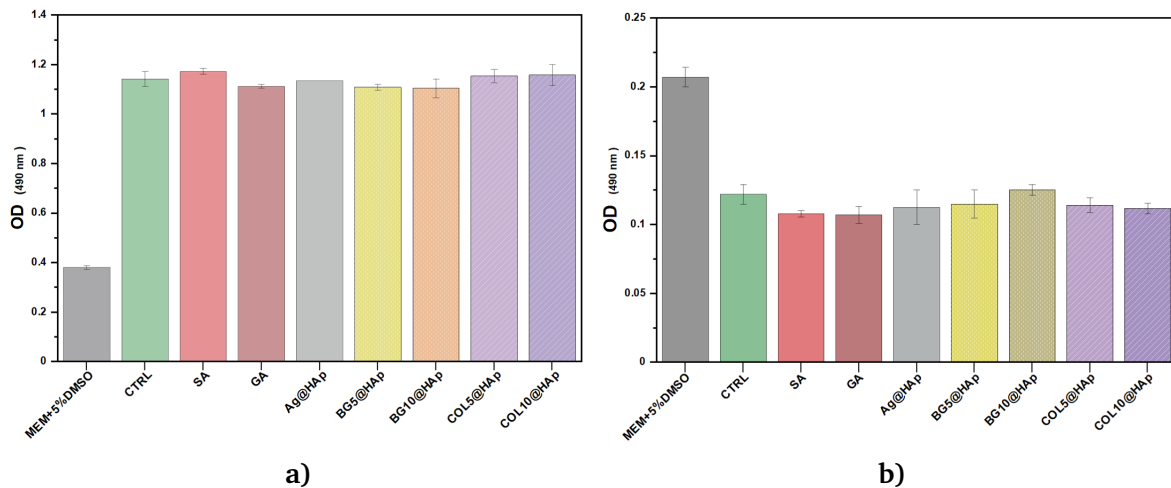
Figure 4.3 – *The cytotoxic potential of the analysed samples highlighted by indirect contact studies, using the LDH test (a) and the MTT test (b) compared to a positive cytotoxicity medium (MEM + 5% DMSO.*

The Figure 4.4 presents the morphology of Vero cells highlighted by phase-contrast microscopy. The interaction of the viable cells with the extraction medium was studied after 24 h. Cells of positive cytotoxicity control (MEM + 5% DMSO), negative cytotoxicity control (MEM + SFB) and coming from CS analysed surfaces of the different materials were all collected after 24h. From these observations, this interaction did not cause a significant change in the cells morphological characteristics compared to those maintained in the normal growth medium. However, in the positive cytotoxicity control, an increased number of dead cells turning to yellow color could be observed.
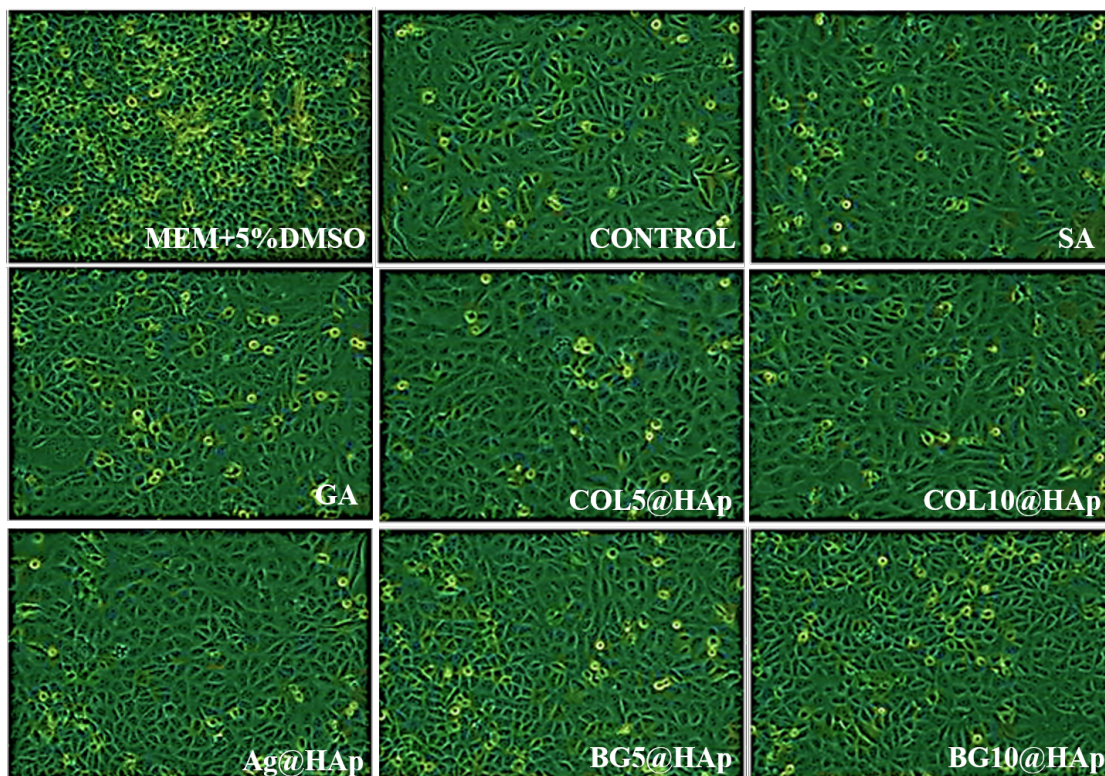
Figure 4.4 – *Observation of Vero cells morphology by phase-contrast microscopy after 24 h of culture of all the CS samples and references.*

4.3 *In vitro* studies of osteoblasts

4.3.1 Osteoblasts proliferation assessment

The structural and functional ability of human bone cells to colonize an artificial implant is called osseointegration. The selection of suitable and reliable materials to design and optimise implants relies on the specific application. The developed implant needs to establish a bond with the surrounding host bone, otherwise insufficient osseointegration leads to fibrous tissue formation and rejection [140]. High-performance biomaterials used in regenerative medicine applications can be obtained by controlling both surface properties of materials and the modulated performances of biomolecules and cells. Indeed, cell interaction is highly sensitive to the roughness of the coating related to microstructural surface characteristics such as size and morphology of grains/pores. As a consequence, the accurate control of these characteristics plays an essential role in the cell adhesion/detachment behaviour and it has consequently a further impact on cell fate [147, 148].

Our studies aimed at exploring the influence of different HAp-based coatings (samples presented in Chapter 3) on osteoblasts growth and proliferation patterns. The response of osteoblasts to the CS samples surfaces were determined using the MC3T3-E1 mouse pre-osteoblast cell line. MC3T3-E1 cells were cultured in Dulbecco's Minimal Essential Medium (DMEL) supplemented with a 10% fetal bovine serum and a 1% antibiotic-antifungal (penicillin/streptomycin) and then incubated at 37°C in a humid atmosphere containing 5% of CO_2. Osteoblasts were seeded in direct contact with the test samples under various experimental conditions (standard or osteoinductive - additional medium with 50 μg·mL^{-1} ascorbic acid and 5 nM β-glycerophosphate) and maintained in culture for various time intervals. The cell density at the time of seeding was 4 x 10^4 cells·cm^2. Before starting the experiments, the materials were sterilised by exposure to UV light for 60 minutes in a laminar flow hood for cell cultures. The proliferation capacity was investigated using the MTT test. The adhesion degree to the substrate and the osteoblasts morphology were highlighted by immunofluorescent labelling of cytoskeletal actin and vinculin, a protein present in focal adhesions. The MTT quantitative evaluation assay was used to investigate the effect of the 7 CS samples on the proliferation of MC3T3-E1 osteoblasts, which was based on the correlation between mitochondrial activity dehydrogenases of metabolically active viable cells and the number of living cells attached to the sample surface. The ability of CS samples and metal substrate (control) to support osteoblasts viability and proliferation was achieved using this method at intervals of 1, 3 and 5 days after seeding (Figure 4.5). Culture of MC3T3-E1 pre-osteoblasts in direct contact with the sample surfaces indicated a great biocompatibility as an increased percentage of seeded cells maintained their metabolic activity. Moreover, the obtained graph showed an increase in the number of cells in the interval between 1-5 days in the case of all the investigated surfaces. However, there was a difference in the growth rate of MC3T3-E1 cells depending on the biomaterial on which they were cultured. As it can be seen in Figure 4.5, the area represented by COL10@HAp induced the highest metabolic activity in the studied range, while BG10@HAp showed a low metabolic activity compared to the other analysed samples. This activity is the expression of the number of viable cells.
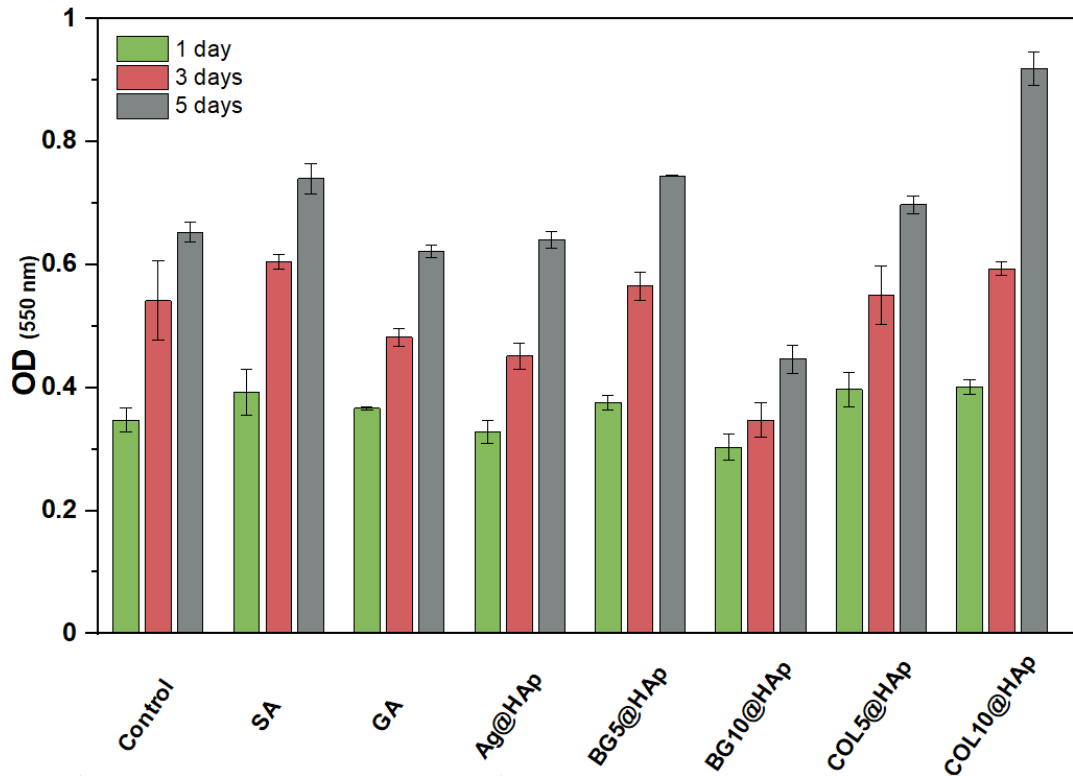
Figure 4.5 – *MTT cell-proliferation assay of MC3T3-E1 cells grown directly onto CS samples and metal substrate (control), used as a control, after 1, 3 and 5 days after seeding.*

4.3.2 Osteoblasts adhesion assessment

Cell adhesion represents the first stage of cell-biomaterial interaction. This process is mainly controlled by the adhesive molecules (*e.g.* fibronectin) and the specific receptors located on the cell membrane. At the level of synthetic surfaces, cell adhesion is a consequence of the adsorption of proteins onto the substrate and it is dependent on the biomaterial surface characteristics. In our study, the adhesion capacity of MC3T3-E1 osteoblasts was investigated 2 h after seeding on the tested samples by marking cytoskeletal actin with phalloidin coupled with Alexa Fluor 488, and respectively of vinculin with anti-vinculin primary antibody and a specific secondary antibody coupled with Alexa Fluor 546 (Figure 4.6). The fluorescence microscopy images at the focal adhesion sites level highlight the vinculin with a punctiform appearance at the cells periphery. Thus, the obtained results demonstrate the ability of the 7 studied CS coatings surfaces to support the adhesion of MC3T3-E1 cells. However, a slightly reduced level of adhesion was observed when the cells were cultured on BG10@HAp, which was probably due to the high reactivity of Bioglass with its increasing percentage, that led to the rapid exchange of ions with the medium and to an increase of pH.

The morphological characteristics of osteoblasts were evaluated through the substrate population degree as well as the shape and display on the substrate of the cells that follow immunofluorescent labelling, as previously described. The morphology of MC3T3-E1 osteoblasts cultured in direct contact with the surface of the studied CS samples 24h after the seeding was highlighted by fluorescence microscopy (Figure 4.7). Observations show that the cells progressively spread over the surface of the studied CS samples, and most of the osteoblasts adopt a polygonal morphology, slightly elongated, characteristic of this cell type. Moreover, there is an organised cytoskeleton, with well-defined stress fibres distributed predominantly throughout the cell body. The
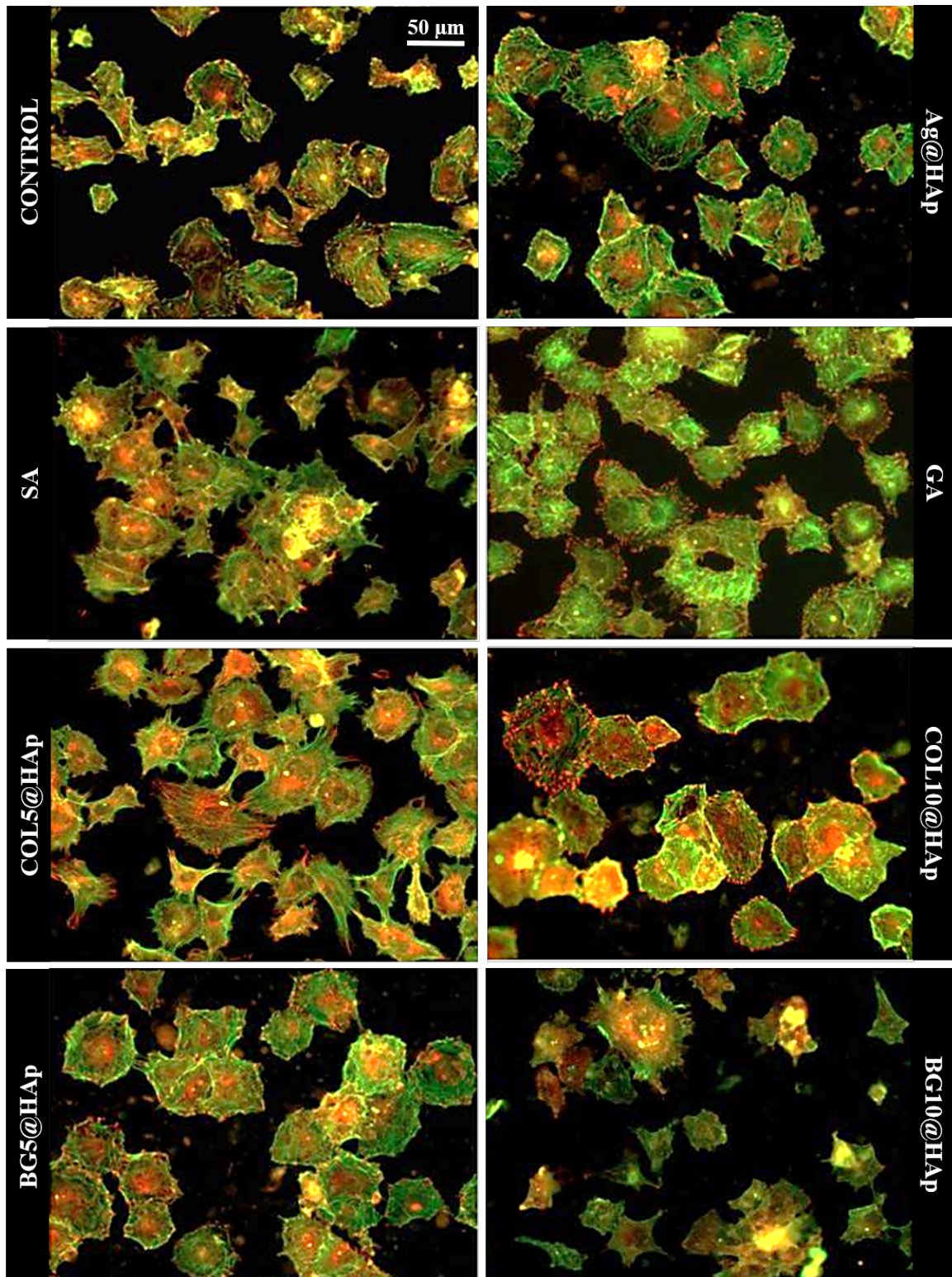
Figure 4.6 – *Osteoblast MC3T3-E1 cell adhesion highlighted through fluorescent labelling of cytoskeletal actin with phalloidin coupled with Alexa Fluor 488 (green) and vinculin with specific secondary antibody coupled with Alexa Fluor 546 (red).*
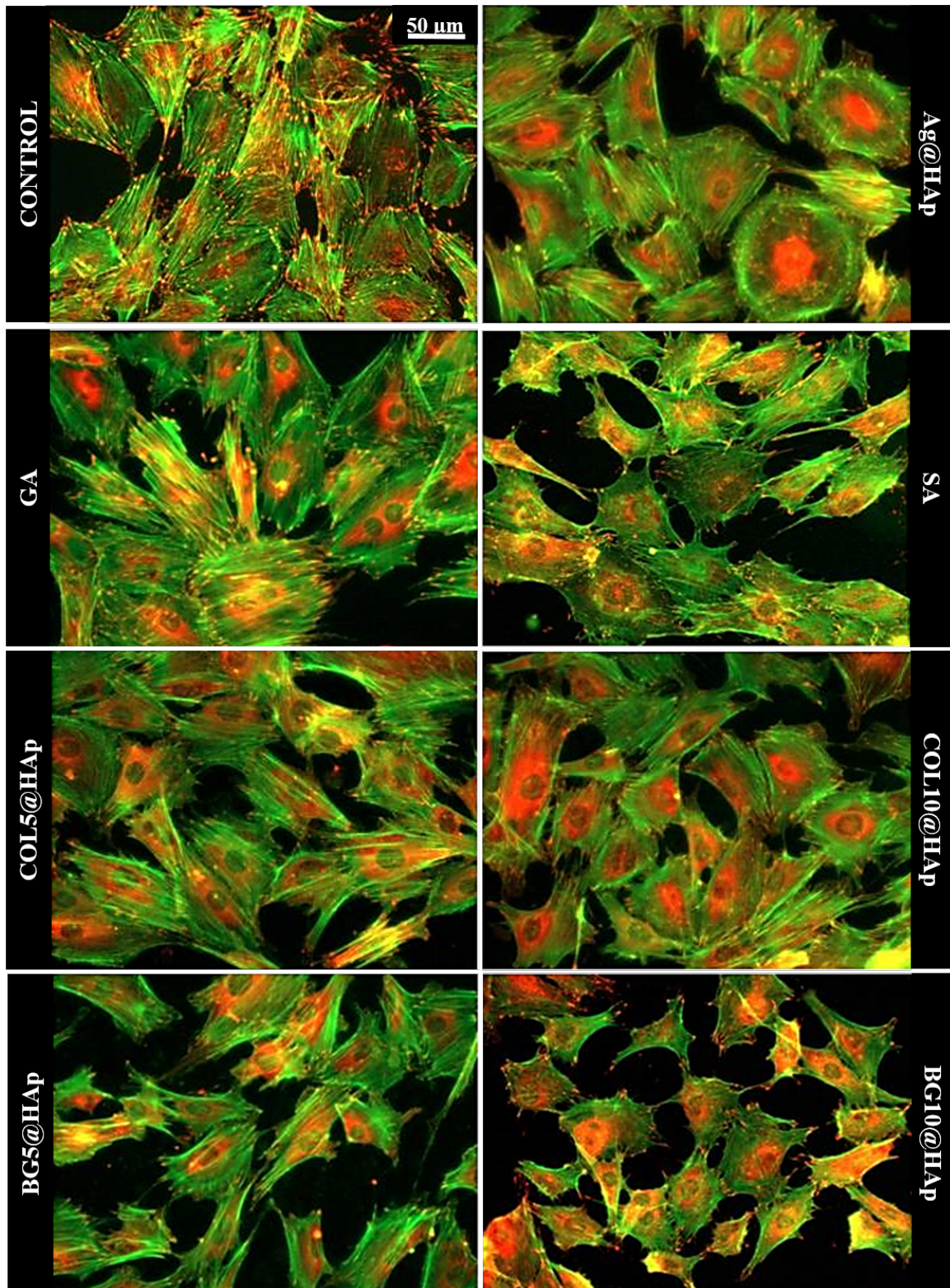
Figure 4.7 – *Characteristics of MC3T3-E1 osteoblasts highlighted by fluorescent labelling of cytoskeletal actin with phalloidin coupled with Alexa Fluor 488 (green) and vinculin with specific secondary antibody coupled with Alexa Fluor 546 (red).*

vinculin is found at the focal adhesion contacts. These aspects are associated with strong adhesion of osteoblasts to the substrate. *In vitro* results demonstrate that all investigated surfaces have the ability to support the development of MC3T3-E1 cells with normal morphology and numerous focal adhesion points that anchor the cells to the surface of the tested samples. Slightly lower cell density was observed in osteoblasts cultured on BG10@HAp 24 h after seeding compared to other surfaces. Moreover, the degree of the cellular display was approximately similar to a reduction in BG15@HAp and BG10@HAp substrates.

4.4   Conclusion - Chapter 4

According to the ISO 10993-5 standard, the indirect studies of cytotoxicity performed by contact on CS coatings demonstrated that the analysed biomaterials did not show toxicity in biological environments. Performed *in vitro* tests indicated a different behaviour of MC3T3-E1 osteoblasts depending on the physico-chemical properties of the CS coatings surfaces. However, taking into account the experimental studied conditions, a satisfied bio-performance of all analysed surfaces was observed in terms of cell viability and proliferation. Furthermore, the response of MC3T3-E1 pre-osteoblasts to direct contact with the CS coatings proved i) the ability of tested surfaces to support cell proliferation within 1-5 days of seeding, ii) the adequate adhesion to the substrate and iii) the ability to promote the normal development of the actin skeleton of cells. Therefore, all the tested CS coatings are biocompatible, representing suitable candidates for biomedical applications.

General conclusion and future perspectives

This thesis was devoted to the development of the Cold Spray (CS) coating technique to deposit HAp-based biomaterials that could be used in medical implants for Bone Tissue Engineering (BTE). We exploited the CS capability to perform the deposition at low temperature, thus preventing from any undesirable phase transformation and grain growth, two of the key factors to obtain a better osseointegration.

The current extensive efforts pursued in academia and the industrial sector are indeed to design effective coatings that can produce a favourable interaction with the living tissues and allow for a biological healing process. In this thesis, we first evaluated the possibility to adapt High Pressure CS (HPCS) to obtain such HAp-based ceramic coatings. We also went beyond the state of the art while studying the fabrication of novel HAp-based hybrid coatings with potentially enhanced bio-activity adding bio-active "dopants" to the HAp.

Normally Low Pressure CS (LPCS) is more suitable than HPCS to deposit ceramics like HAp because of a better stream feeding stability. In our case, since we worked with HPCS, we observed such a trend when using a radial injection of the feedstock powder which did not allow to get homogeneous coatings. More specifically, the powder jet stream was operating with pulses, followed by immediate clogging. However, when switching the powder injection system from a standard radial system to an axial one, HPCS was more stable and reliable, so that we could perform the deposition tests.

In order to better understand the CS deposition mechanisms of HAp, FIB-SEM investigations were carried out on single particle impacts, while varying the particles in-flight velocity. The results showed that, whatever the HAp feedstock powders used, as-delivered (GA powder) or pre-sintered (SA powder), they maintained their cristallinity and grain size upon deposition, confirming the low temperature involved in the CS coating process. Another factor that influenced the deposition was the substrate surface state in terms of roughness and hardness. To study these parameters, 3 types of substrates were prepared on the basis of a TA6V alloy: grit-blasted, laser textured and top-coated with Ti grade 2 by HPCS. When comparing GA and SA powders, GA led to thicker coatings, which could be attributed to a better ability to undergo compaction upon multiple impacts. This was in line with mechanical tests performed on single agglomerates in situ in a SEM under loading-unloading cyclic solicitations. Being a more cohesive powder, SA was less prone to compaction. The coatings consolidation was essentially due to a mechanical anchor through particles interlocking (granular compacts) and effect of high roughness (e.g. laser textured substrates). No chemical reactions were really involved in the consolidation process, so that a poor adhesion of the coatings was registered, which was actually the major drawback of these coatings.

Compared to Aerosol Deposition Method (ADM), for which coatings with good adhesion could be obtained under vacuum by others, the main difference for CS was the atmospheric environment. In CS, we were working with hot nitrogen gas to accelerate the powders at the required velocity in a surrounding air atmosphere. It was likely that gas molecules could be easily adsorbed on fresh surfaces resulting of the fragmentation, thus inhibiting possible chemical reactions and negatively affecting the adhesion strength. Moreover, close to the substrate there was probably also a compression of the atmospheric gas that could potentially decrease the particles initial velocity reducing the impact energy necessary to fragment the elementary particles contained in the agglomerates. Such a fragmentation of elementary particles was indeed not observed. In order to mitigate this issue of adhesion, post heat

treatments were applied with a limited success in terms of adhesion improvement, as demonstrated by scratch tests. Finally, as already mentioned, we developed novel HAp-based hybrid coatings with an expected enhanced bio-activity. Starting from commercially-available HAp powders, we fabricated by spraydrying collagen-HAp and biogalss-HAp agglomerates having the necessary flowability for CS. The distribution of the "dopants" in the agglomerates was quite homogeneous. In addition, by spraydrying we were able to maintain the collagen into a stable form. Another issue addressed was to obtain antimicrobial HAp-based coatings, while functionalizing the HAp powder feedstock with silver nanoparticles by PVD. The various chemical and physical analyses performed on the hybrid coatings showed no changes upon deposition. The potential applications of those hybrid coatings are multiple: (i) for collagen-HAp, the structural collagen protein is expected to promote regenerative cells to repopulate bone defect areas, (ii) for bioglass-HAp, bioglass is seen as a corrosion protective material, and (iii) for Ag-HAp, Ag is added as a powerful antibacterial agent combating the health complications associated with post-operative infections caused by antibiotic-resistant bacterial strains. All the biologically tests carried out on the aforementioned hybrid coatings did not show any specific toxicity. In addition, those hybrid coatings were able to support the cells proliferation. To conclude as for the perspectives, to date the bonding phenomena that lead to the consolidation of ceramic (here HAps) coatings deposited by CS are not yet completely elucidated and remain under debate. In our attempt to better investigate this consolidation, we faced many theoretical and experimental issues that would need additional investigations to be solved, such as for instance:

1- A more reliable characterization of the agglomerates fragmentation. In this aim, the mechanical tests we performed at the Imperial College London (ICL) on single agglomerates in a SEM were highly valuables. But, for a better exploitation of them, they would require the use of really model agglomerates to get more accurate results. Also, to be more representative of what happens at the impact, solicitations at very high loading rates would be required. This seems to be possible with the new original set-up the team of ICL recently bought.

2- A deeper insight in the fragmentation mechanisms through numerical simulations. This is likely what must be done at first in the near future. When thinking about numerical simulations, one has to consider which methodology has to be applied. Discrete Element Modelling (DEM) is probably the method of choice, the problem remaining how to treat the mechanical contacts between the discrete elements (i.e. the elementary particles of the agglomerates) in ballistic conditions. The modelling of the mechanical response of the contacts in such specific conditions requires at a minimum the knowledge of the Hugoniot elastic limit of the material. In any cases, this point 2 is strongly linked to point 1 if one wants to establish relationships between numerical simulations and experiments.

3- The inclusion of plastic "dopants" into the HAp agglomerates. Adding metallic particles of a size and quantity to be tuned would of course promote the consolidation. But it could also affect the bio-activity. For instance, toxicity problems may appear due to metallic ion release under corrosion. A good balance between both phenomena has then to be found.

4- The exploration of new CS parametric fields. It is likely that working with LPCS under vacuum would be a better option than HPCS in ambient atmosphere, but this has still to be confirmed.

Bibliography

[1] J. R. Davis, *Handbook of Thermal Spray Technology*. ASM International, 2004.

[2] R. Rija Nirina, C. Verdy, and H. Liao, "Cold gas dynamic spray additive manufacturing today: Deposit possibilities, technological solutions and viable applications," *Materials & Design*, vol. 133, 2017-07-01. [Online]. Available: https://doi.org/10.1016/j.matdes.2017.07.067

[3] M. Oksa, E. Turunen, T. Suhonen, T. Varis, and S.-P. Hannula, "Optimization and characterization of high velocity oxy-fuel sprayed coatings: techniques, materials, and applications," *Coatings*, vol. 1, no. 1, pp. 17–52, 2011. [Online]. Available: https://doi.org/10.3390/coatings1010017

[4] R. Rija Nirina, C. Verdy, and H. Liao, "Cold gas dynamic spray additive manufacturing today: Deposit possibilities, technological solutions and viable applications," *Materials and Design*, vol. 133, 2017-07-01. [Online]. Available: https://doi.org/10.1016/j.matdes.2017.07.067

[5] Oerlikon, "An introduction to thermal spray," https://www.oerlikon.com, May 2018.

[6] T. Schmidt, H. Assadi, F. Gärtner, H. Richter, T. Stoltenhoff, H. Kreye, and T. Klassen, "From particle acceleration to impact and bonding in cold spraying," *Journal of Thermal Spray Technology*, vol. 18, no. 5-6, p. 794, 2009. [Online]. Available: https://doi.org/10.1007/s11666-009-9357-7

[7] T. Van Steenkiste, J. Smith, and R. Teets, "Aluminum coatings via kinetic spray with relatively large powder particles," *Surface and Coatings Technology*, vol. 154, no. 2-3, pp. 237–252, 2002. [Online]. Available: https://doi.org/10.1016/S0257-8972(02)00018-X

[8] T. Schmidt, F. Gärtner, H. Assadi, and H. Kreye, "Development of a generalized parameter window for cold spray deposition," *Acta materialia*, vol. 54, no. 3, pp. 729–742, 2006. [Online]. Available: https://doi.org/10.1016/j.actamat.2005.10.005

[9] M. Walker, "Microstructure and bonding mechanisms in cold spray coatings," *Materials Science and Technology*, vol. 34, no. 17, pp. 2057–2077, 2018. [Online]. Available: https://doi.org/10.1080/02670836.2018.1475444

[10] G. Bae, Y. Xiong, S. Kumar, K. Kang, and C. Lee, "General aspects of interface bonding in kinetic sprayed coatings," *Acta Materialia*, vol. 56, no. 17, pp. 4858–4868, 2008. [Online]. Available: https://doi.org/10.1016/j.actamat.2008.06.003

[11] A. M. Vilardell, N. Cinca, S. Dosta, I. G. Cano, and J. M. Guilemany, "Feasibility of using low pressure cold gas spray for the spraying of thick ceramic hydroxyapatite coatings," *International Journal of Applied Ceramic Technology*, vol. 16, no. 1, pp. 221–229, 2019. [Online]. Available: https://doi.org/10.1111/ijac.13088

[12] R. Chakrabarty and J. Song, "Numerical simulations of ceramic deposition and retention in metal-ceramic composite cold spray," *Surface and Coatings Technology*, vol. 385, p. 125324, 2020. [Online]. Available: https://doi.org/10.1016/j.surfcoat.2019.125324

[13] J.-O. Kliemann, H. Gutzmann, F. Gärtner, H. Hübner, C. Borchers, and T. Klassen, "Formation of cold-sprayed ceramic titanium dioxide layers on metal surfaces," *Journal of thermal spray technology*, vol. 20, no. 1, pp. 292–298, 2011. [Online]. Available: https://doi.org/10.1007/s11666-010-9563-3

[14] M. Yamada, H. Isago, H. Nakano, and M. Fukumoto, "Cold spraying of TiO 2 photocatalyst coating with nitrogen process gas," *Journal of thermal spray technology*, vol. 19, no. 6, pp. 1218–1223, 2010. [Online]. Available: https://doi.org/10.1007/s11666-010-9520-1

[15] A. R. Toibah, M. Sato, M. Yamada, and M. Fukumoto, "Cold-sprayed TiO2 coatings from nanostructured ceramic agglomerated powders," *Materials and Manufacturing Processes*, vol. 31, no. 11, pp. 1527–1534, 2016. [Online]. Available: https://doi.org/10.1080/10426914.2015.1090587

[16] H. Y. Lee, Y. H. Yu, Y. C. Lee, Y. P. Hong, and K. H. Ko, "Thin film coatings of WO 3 by cold gas dynamic spray: A technical note," *Journal of thermal spray technology*, vol. 14, no. 2, pp. 183–186, 2005. [Online]. Available: https://doi.org/10.1361/105996304523791

[17] M. Hasniyati, H. Zuhailawati, R. Sivakumar, B. K. Dhindaw, and S. Noor, "Cold spray deposition of hydroxyapatite powder onto magnesium substrates for biomaterial applications," *Surface Engineering*, vol. 31, no. 11, pp. 867–874, 2015. [Online]. Available: https://doi.org/10.1179/1743294415Y.0000000068

[18] A. C. Noorakma, H. Zuhailawati, V. Aishvarya, and B. K. Dhindaw, "Hydroxyapatite-coated magnesium-based biodegradable alloy: cold spray deposition and simulated body fluid studies," *Journal of materials engineering and performance*, vol. 22, no. 10, pp. 2997–3004, 2013. [Online]. Available: https://doi.org/10.1007/s11665-013-0589-9

[19] A. M. Vilardell, N. Cinca, N. Garcia-Giralt, S. Dosta, I. G. Cano, X. Nogués, and J. M. Guilemany, "In-vitro comparison of hydroxyapatite coatings obtained by cold spray and conventional thermal spray technologies," *Materials Science and Engineering: C*, vol. 107, p. 110306, 2020. [Online]. Available: https://doi.org/10.1016/j.msec.2019.110306

[20] J. Breme, E. Eisenbarth, and V. Biehl, "Titanium and its alloys for medical applications," *Titanium and Titanium Alloys: Fundamentals and Applications*, pp. 423–451, 2003. [Online]. Available: https://doi.org/10.1002/3527602119.ch16

[21] P. Pinke, L. Caplovic, and T. Kovacs, "The influence of heat treatment on the microstructure of the casted ti-6al-4v titanium alloy," *Slovak University of Technology Bratislava. Web*, vol. 11, 2011.

[22] M. Peters, J. Hemptenmacher, J. Kumpfert, and C. Leyens, "Structure and properties of titanium and titanium alloys," *Titanium and titanium alloys: fundamentals and applications*, pp. 1–36, 2003. [Online]. Available: https://doi.org/10.1002/3527602119.ch1

[23] I. Manjubala, T. Sastry, and R. S. Kumar, "Bone in-growth induced by biphasic calcium phosphate ceramic in femoral defect of dogs," *Journal of biomaterials applications*, vol. 19, no. 4, pp. 341–360, 2005. [Online]. Available: https://doi.org/10.1177/0885328205048633

[24] G. Ma and X. Y. Liu, "Hydroxyapatite: hexagonal or monoclinic?" *Crystal Growth and Design*, vol. 9, no. 7, pp. 2991–2994, 2009. [Online]. Available: https://doi.org/10.1021/cg900156w

[25] L. L. Hench, "Bioceramics: from concept to clinic," *Journal of the american ceramic society*, vol. 74, no. 7, pp. 1487–1510, 1991. [Online]. Available: https://doi.org/10.1111/j.1151-2916.1991.tb07132.x

[26] F. E. Bastan, G. Erdogan, T. Moskalewicz, and F. Ustel, "Spray drying of hydroxyapatite powders: The effect of spray drying parameters and heat treatment on the particle size and morphology," *Journal of Alloys and Compounds*, vol. 724, pp. 586–596, 2017. [Online]. Available: https://doi.org/10.1016/j.jallcom.2017.07.116

[27] N. Durán, M. Durán, M. B. de Jesus, A. B. Seabra, W. J. Fávaro, and G. Nakazato, "Silver nanoparticles: A new view on mechanistic aspects on antimicrobial activity," *Nanomedicine: Nanotechnology, Biology, and Medicine*, vol. 12, no. 3, pp. 789–799, 2016. [Online]. Available: https://doi.org/10.1016/j.nano.2015.11.016

[28] G. Bräuer, "4.03 - Magnetron Sputtering," in *Comprehensive Materials Processing*, S. Hashmi, G. F. Batalha, C. J. Van Tyne, and B. Yilbas, Eds. Oxford: Elsevier, 2014, pp. 57–73. [Online]. Available: https://doi.org/10.1016/B978-0-08-096532-1.00403-9

[29] L. Martin, Y.-H. Chu, and R. Ramesh, "Advances in the growth and characterization of magnetic, ferroelectric, and multiferroic oxide thin films," *Materials Science and Engineering: R: Reports*, vol. 68, no. 4-6, pp. 89–133, 2010. [Online]. Available: https://doi.org/10.1016/j.mser.2010.03.001

[30] H. Koivuluoto, J. Larjo, D. Marini, G. Pulci, and F. Marra, "Cold-sprayed al6061 coatings: Online spray monitoring and influence of process parameters on coating properties," *Coatings*, vol. 10, no. 4, p. 348, 2020. [Online]. Available: https://doi.org/10.3390/coatings10040348

[31] A. M. Vilardell, N. Cinca, I. G. Cano, A. Concustell, S. Dosta, J. M. Guilemany, S. Estradé, A. Ruiz-Caridad, and F. Peiró, "Dense nanostructured calcium phosphate coating on titanium by cold spray," *Journal of the European Ceramic Society*, vol. 37, no. 4, pp. 1747–1755, 2017. [Online]. Available: https://doi.org/10.1016/j.jeurceramsoc.2016.11.040

[32] Q.-Y. Chen, Y.-L. Zou, X. Chen, X.-B. Bai, G.-C. Ji, H.-L. Yao, H.-T. Wang, and F. Wang, "Morphological, structural and mechanical characterization of cold sprayed hydroxyapatite coating," *Surface and Coatings Technology*, vol. 357, pp. 910–923, 2019. [Online]. Available: https://doi.org/10.1016/j.surfcoat.2018.10.056

[33] ASTM-F67-13, "Specification for unalloyed titanium, for surgical implant applications," ASTM International, Tech. Rep., 2017. [Online]. Available: http://www.astm.org/cgi-bin/resolver.cgi?F67-13R17

[34] ASTM-F136-13, "Specification for wrought titanium-6aluminum-4vanadium ELI (extra low interstitial) alloy for surgical implant applications," ASTM International, Tech. Rep., 2013. [Online]. Available: http://www.astm.org/cgi-bin/resolver.cgi?F136-13

[35] N. Eliaz and N. Metoki, "Calcium phosphate bioceramics: a review of their history, structure, properties, coating technologies and biomedical applications," *Materials*, vol. 10, no. 4, p. 334, 2017. [Online]. Available: https://doi.org/10.3390/ma10040334

[36] L. Ambrosio, *Biomedical composites*. Woodhead Publishing, 2017.

[37] R. Pignatello, *Advances in biomaterials science and biomedical applications*. BoD–Books on Demand, 2013.

[38] A. Ion, E. Andronescu, D. Radulescu, M. Rdulescu, F. Iordache, B. S. Vasile, A. V. Surdu, M. G. Albu, H. Maniu, M. C. Chifiriuc *et al.*, "Biocompatible 3d matrix with antimicrobial properties," *Molecules*, vol. 21, no. 1, p. 115, 2016.

[39] B. D. Ratner, A. S. Hoffman, F. Schoen, J. E. Lemons, W. R. WAGNER, S. E. SAKIYAMA-ELBERT, G. ZHANG, and M. J. YASZEMSKI, *Introduction—biomaterials science: an evolving, multidisciplinary endeavor*. Elsevier, Academic Press, Cambridge, MA, USA,, 2013.

[40] A. J. Salinas and M. Vallet-Regí, "The sol–gel production of bioceramics," in *Key Engineering Materials*, vol. 391. Trans Tech Publ, 2009, pp. 141–158. [Online]. Available: https://doi.org/10.4028/www.scientific.net/KEM.391.141

[41] N. Calha, A. Messias, F. Guerra, B. Martinho, M. A. Neto, and P. Nicolau, "Effect of geometry on deformation of anterior implant-supported zirconia frameworks: An in vitro study using digital image correlation," *Journal of prosthodontic research*, vol. 61, no. 2, pp. 139–148, 2017. [Online]. Available: https://doi.org/10.1016/j.jpor.2016.08.004

[42] A. Goharian, *Osseointegration of Orthopaedic Implants*. Academic Press, 2019.

[43] L. L. Hench and J. M. Polak, "Third-generation biomedical materials," *Science*, vol. 295, no. 5557, pp. 1014–1017, 2002. [Online]. Available: https://doi.org/10.1126/science.1067404

[44] M. S. Zafar, I. Farooq, M. Awais, S. Najeeb, Z. Khurshid, and S. Zohaib, "Bioactive surface coatings for enhancing osseointegration of dental implants," in *Biomedical, therapeutic and clinical applications of bioactive glasses*. Elsevier, 2019, pp. 313–329.

[45] A. Moridi, S. M. Hassani-Gangaraj, M. Guagliano, and M. Dao, "Cold spray coating: review of material systems and future perspectives," *Surface Engineering*, vol. 30, no. 6, pp. 369–395, 2014-06. [Online]. Available: https://doi.org/10.1179/1743294414Y.0000000270

[46] P. L. Fauchais, J. V. R. Heberlein, and M. Boulos, *Thermal Spray Fundamentals: From Powder to Part*. Springer US, 2014. [Online]. Available: http://doi.org/10.1007/978-0-387-68991-3

[47] L. Pawlowski, *The Science and Engineering of Thermal Spray Coatings*. John Wiley & Sons, 2008-04-30. [Online]. Available: https://doi.org/10.1002/9780470754085

[48] P. L. Fauchais, J. V. R. Heberlein, and M. I. Boulos, "Overview of thermal spray," in *Thermal Spray Fundamentals: From Powder to Part*, P. L. Fauchais, J. V. Heberlein,

and M. I. Boulos, Eds. Springer US, 2014, pp. 17–72. [Online]. Available: https://doi.org/10.1007/978-0-387-68991-3_2

[49] P. Fauchais, A. Vardelle, and B. Dussoubs, "Quo vadis thermal spraying?" *Journal of Thermal Spray Technology*, vol. 10, no. 1, pp. 44–66, 2001. [Online]. Available: https://doi.org/10.1361/105996301770349510

[50] D. Tejero-Martin, M. Rezvani Rad, A. McDonald, and T. Hussain, "Beyond traditional coatings: A review on thermal-sprayed functional and smart coatings," *Journal of Thermal Spray Technology*, vol. 28, no. 4, pp. 598–644, 2019-04-01. [Online]. Available: https://doi.org/10.1007/s11666-019-00857-1

[51] A. P. Alkhimov, A. N. Papyrin, V. F. Kosarev, N. I. Nesterovich, and M. M. Shushpanov, "Gas-dynamic spraying method for applying a coating," russian patentus 5 302 414A, 1994. [Online]. Available: https://patentimages.storage.googleapis.com/92/16/7f/93e032d9041894/US5302414.pdf

[52] R. Nikbakht, S. H. Seyedein, S. Kheirandish, H. Assadi, and B. Jodoin, "The role of deposition sequence in cold spraying of dissimilar materials," *Surface and Coatings Technology*, vol. 367, pp. 75–85, 2019-06-15. [Online]. Available: http://10.1016/j.surfcoat.2019.03.065

[53] R. Dykhuizen and M. Smith, "Gas dynamic principles of cold spray," *Journal of Thermal spray technology*, vol. 7, no. 2, pp. 205–212, 1998. [Online]. Available: https://doi.org/10.1361/105996398770350945

[54] H. Assadi, F. Gärtner, T. Stoltenhoff, and H. Kreye, "Bonding mechanism in cold gas spraying," *Acta Materialia*, vol. 51, no. 15, pp. 4379–4394, 2003. [Online]. Available: https://doi.org/10.1016/S1359-6454(03)00274-X

[55] M. Grujicic, J. R. Saylor, D. E. Beasley, W. S. DeRosset, and D. Helfritch, "Computational analysis of the interfacial bonding between feed-powder particles and the substrate in the cold-gas dynamic-spray process," *Applied Surface Science*, vol. 219, no. 3, pp. 211–227, 2003. [Online]. Available: https://doi.org/10.1016/S0169-4332(03)00643-3

[56] M. Grujicic, C. L. Zhao, W. S. DeRosset, and D. Helfritch, "Adiabatic shear instability based mechanism for particles/substrate bonding in the cold-gas dynamic-spray process," *Materials & design*, vol. 25, no. 8, pp. 681–688, 2004. [Online]. Available: https://doi.org/10.1016/j.matdes.2004.03.008

[57] C.-J. Li, W.-Y. Li, Y.-Y. Wang, G.-J. Yang, and H. Fukanuma, "A theoretical model for prediction of deposition efficiency in cold spraying," *Thin Solid Films*, vol. 489, no. 1, pp. 79–85, 2005. [Online]. Available: https://doi.org/10.1016/j.tsf.2005.05.002

[58] W. Li, K. Yang, D. Zhang, X. Zhou, and X. Guo, "Interface behavior of particles upon impacting during cold spraying of cu/ni/al mixture," *Materials & Design*, vol. 95, pp. 237–246, 2016. [Online]. Available: https://doi.org/10.1016/j.matdes.2016.01.122

[59] T. Hussain, "Cold spraying of titanium: a review of bonding mechanisms, microstructure and properties," in *Key engineering materials*, vol. 533. Trans Tech Publ, 2013, pp. 53–90. [Online]. Available: 10.4028/www.scientific.net/KEM.533.53

[60] H. Singh, T. Sidhu, S. Kalsi, and J. Karthikeyan, "Development of cold spray from innovation to emerging future coating technology," *Journal of the Brazilian Society of Mechanical Sciences and Engineering*, vol. 35, 2013-10-01. [Online]. Available: https://doi.org/10.1007/s40430-013-0030-1

[61] D. Goldbaum, J. M. Shockley, R. R. Chromik, A. Rezaeian, S. Yue, J.-G. Legoux, and E. Irissou, "The effect of deposition conditions on adhesion strength of Ti and Ti6Al4V cold spray splats," *Journal of thermal spray technology*, vol. 21, no. 2, pp. 288–303, 2012. [Online]. Available: https://doi.org/10.1007/s11666-011-9720-3

[62] S. Rech, A. Surpi, S. Vezzù, A. Patelli, A. Trentin, J. Glor, J. Frodelius, L. Hultman, and P. Eklund, "Cold-spray deposition of Ti2AlC coatings," *Vacuum*, vol. 94, pp. 69–73, 2013. [Online]. Available: https://doi.org/10.1016/j.vacuum.2013.01.023

[63] H. Gutzmann, F. Gärtner, D. Höche, C. Blawert, and T. Klassen, "Cold spraying of Ti2AlC MAX-phase coatings," *Journal of thermal spray technology*, vol. 22, no. 2, pp. 406–412, 2013. [Online]. Available: https://doi.org/10.1007/s11666-012-9843-1

[64] D. W. Sun, M. P. Sealy, Z. Y. Liu, C. H. Fu, Y. B. Guo, F. Z. Fang, and B. Zhang, "Finite element analysis of machining damage in single-grit grinding of ceramic knee implants," *Procedia Manufacturing*, vol. 1, pp. 644–654, 2015. [Online]. Available: https://doi.org/10.1016/j.promfg.2015.09.058

[65] X. Zhang and H. Hao, "Experimental and numerical study of boundary and anchorage effect on laminated glass windows under blast loading," *Engineering Structures*, vol. 90, pp. 96–116, 2015. [Online]. Available: https://doi.org/10.1016/j.engstruct.2015.02.022

[66] F. Meng, D. Hu, Y. Gao, S. Yue, and J. Song, "Cold-spray bonding mechanisms and deposition efficiency prediction for particle/substrate with distinct deformability," *Materials & Design*, vol. 109, pp. 503–510, 2016. [Online]. Available: https://doi.org/10.1016/j.matdes.2016.07.103

[67] C.-J. Li, G.-J. Yang, X.-C. Huang, W.-Y. Li, and A. Ohmori, "Formation of tio 2 photocatalyst through cold spraying," in *ITSC 2004: International Thermal Spray Conference 2004: Advances in Technology and Application*, 2004, pp. 315–319.

[68] J. H. Han, S. W. Lee, E. A. Lee, T. Y. Xiong, Z. Bao, and H. Du, "Photocatalytic properties of TiO2 coatings prepared by cold spray process," in *Materials science forum*, vol. 510. Trans Tech Publ, 2006, pp. 130–133. [Online]. Available: https://doi.org/10.4028/www.scientific.net/MSF.510-511.130

[69] M. Yamada, Y. Kandori, K. Sato, and M. Fukumoto, "Fabrication of titanium dioxide photocatalyst coatings by cold spray," *Journal of Solid Mechanics and Materials Engineering*, vol. 3, no. 2, pp. 210–216, 2009. [Online]. Available: https://doi.org/10.1299/jmmp.3.210

[70] K. Schmidt, S. Buhl, N. Davoudi, C. Godard, R. Merz, I. Raid, E. Kerscher, M. Kopnarski, C. Müller-Renno, and S. Ripperger, "Ti surface modification by cold spraying with TiO2 microparticles," *Surface and Coatings Technology*, vol. 309, pp. 749–758, 2017. [Online]. Available: https://doi.org/10.1016/j.surfcoat.2016.10.091

[71] H. Park, F. Cao, J. Kwon, and C. Lee, "The effect of shock-induced plastic deformation on alumina deposition during vacuum kinetic spraying," in *International Thermal Spray Conference and Exposition: Innovative Coating Solutions for the Global Economy, ITSC 2013*.   ASM International, 2013, pp. 279–285.

[72] D. Seo, M. Sayar, and K. Ogawa, "SiO2 and MoSi2 formation on inconel 625 surface via SiC coating deposited by cold spray," *Surface and Coatings Technology*, vol. 206, no. 11, pp. 2851–2858, 2012. [Online]. Available: https://doi.org/10.1016/j.surfcoat.2011.12.010

[73] Q. Chen and G. Thouas, *Biomaterials: a basic introduction*.   CRC Press, 2014.

[74] N. Sanpo, M. L. Tan, P. Cheang, and K. A. Khor, "Antibacterial property of cold-sprayed HA-ag/PEEK coating," *Journal of thermal spray technology*, vol. 18, no. 1, pp. 10–15, 2009. [Online]. Available: https://doi.org/10.1007/s11666-008-9283-0

[75] J. H. Lee, H. L. Jang, K. M. Lee, H.-R. Baek, K. Jin, K. S. Hong, J. H. Noh, and H.-K. Lee, "In vitro and in vivo evaluation of the bioactivity of hydroxyapatite-coated polyetheretherketone biocomposites created by cold spray technology," *Acta biomaterialia*, vol. 9, no. 4, pp. 6177–6187, 2013. [Online]. Available: https://doi.org/10.1016/j.actbio.2012.11.030

[76] J. H. Lee, H. L. Jang, K. M. Lee, H.-R. Baek, K. Jin, and J. H. Noh, "Cold-spray coating of hydroxyapatite on a three-dimensional polyetheretherketone implant and its biocompatibility evaluated by in vitro and in vivo minipig model," *Journal of Biomedical Materials Research Part B: Applied Biomaterials*, vol. 105, no. 3, pp. 647–657, 2017. [Online]. Available: https://doi.org/10.1002/jbm.b.33589

[77] M. Chagnon, L.-G. Guy, and N. Jackson, "Evaluation of magnesium-based medical devices in preclinical studies: Challenges and points to consider," *Toxicologic pathology*, vol. 47, no. 3, pp. 390–400, 2019. [Online]. Available: https://doi.org/10.1177/0192623318816936

[78] M. Vilardell, N. Cinca, S. Dosta, I. G. Cano, and J. M. Guilemany, "Multifunctional miro-nano structured hydroxyapatit coatings onttianum ti6al4v for biomedical applications by cold gas spray," *Acta. de Protocolarizaci on num*, vol. 809, 2015. [Online]. Available: https://doi.org/10.1111/jace.14076

[79] E. Kergourlay, D. Grossin, N. Cinca, C. Josse, S. Dosta, G. Bertrand, I. Garcia, J. M. Guilemany, and C. Rey, "First cold spraying of carbonated biomimetic nanocrystalline apatite on ti6al4v: Physical–chemical, microstructural, and preliminary mechanical characterizations," *Advanced Engineering Materials*, vol. 18, no. 4, pp. 496–500, 2016. [Online]. Available: https://doi.org/10.1002/adem.201500409

[80] J. H. Noh, D. W. Kim, J. S. An, H. R. Chang, D. H. Kim, K. S. Hong, and D. K. Chin, "Method for modifying the surface of a bioinert material," korean patentus 13/148 795, Jan. 12, 2012, uS Patent App. 13/148,795.

[81] L. Zhang, W. T. Zhang, and Z. Y. Wu, "Numerical simulation of hydroxyapatite particle impacting on ti substrate in cold spraying," in *Applied Mechanics and Materials*, vol. 130. Trans Tech Publ, 2012, pp. 900–903. [Online]. Available: https://doi.org/10.4028/www.scientific.net/AMM.130-134.900

[82] M. Kaur and K. Singh, "Review on titanium and titanium based alloys as biomaterials for orthopaedic applications," *Materials Science and Engineering: C*, 2019. [Online]. Available: https://doi.org/10.1016/j.msec.2019.04.064

[83] K. Wang, "The use of titanium for medical applications in the USA," *Materials Science and Engineering: A*, vol. 213, no. 1, pp. 134–137, 1996. [Online]. Available: https://doi.org/10.1016/0921-5093(96)10243-4

[84] L. K. Khoo, W. Sakdajeyont, M. Khanijou, D. Seriwatanachai, S. Kiattavorncharoen, V. Pairuchvej, and N. Wongsirichat, "Titanium fixture implants treated by laser in dentistry," *Journal of Oral and Maxillofacial Surgery, Medicine, and Pathology*, 2019. [Online]. Available: https://doi.org/10.1016/j.ajoms.2019.08.001

[85] M. Geetha, A. K. Singh, R. Asokamani, and A. K. Gogia, "Ti based biomaterials, the ultimate choice for orthopaedic implants–a review," *Progress in materials science*, vol. 54, no. 3, pp. 397–425, 2009. [Online]. Available: https://doi.org/10.1016/j.pmatsci.2008.06.004

[86] A. YazdanYar, U. Aschauer, and P. Bowen, "Interaction of biologically relevant ions and organic molecules with titanium oxide (rutile) surfaces: A review on molecular dynamics studies," *Colloids and Surfaces B: Biointerfaces*, vol. 161, pp. 563–577, 2018. [Online]. Available: https://doi.org/10.1016/j.colsurfb.2017.11.004

[87] C. Leyens, "Oxidation and protection of titanium alloys and titanium aluminides," *Titanium and titanium alloys: fundamentals and applications*, pp. 187–230, 2003. [Online]. Available: https://doi.org/10.1002/3527602119.ch6

[88] L. Wanying, L. Yuanhua, C. Yuhai, S. Taihe, and A. Singh, "Effect of different heat treatments on microstructure and mechanical properties of ti6al4v titanium alloy," *Rare metal Materials and engineering*, vol. 46, no. 3, pp. 634–639, 2017. [Online]. Available: https://doi.org/10.1016/S1875-5372(17)30109-1

[89] S. Zhang, *Biological and Biomedical Coatings Handbook, Two-Volume Set*. CRC Press, 2011. [Online]. Available: https://doi.org/10.1201/9780367807177

[90] E. Rivera-Muñoz and R. Fazel, *Biomedical Engineering—Frontiers and Challenges*. InTech, 2011. [Online]. Available: http://dx.doi.org/10.17977/um024v3i12018p016

[91] R. Murugan and S. Ramakrishna, "Development of nanocomposites for bone grafting," *Composites Science and technology*, vol. 65, no. 15-16, pp. 2385–2406, 2005. [Online]. Available: https://doi.org/10.1016/j.compscitech.2005.07.022

[92] S. Samavedi, A. R. Whittington, and A. S. Goldstein, "Calcium phosphate ceramics in bone tissue engineering: a review of properties and their influence on cell behavior," *Acta biomaterialia*, vol. 9, no. 9, pp. 8037–8045, 2013. [Online]. Available: https://doi.org/10.1016/j.actbio.2013.06.014

[93] G. Turnbull, J. Clarke, F. Picard, P. Riches, L. Jia, F. Han, B. Li, and W. Shu, "3d bioactive composite scaffolds for bone tissue engineering," *Bioactive materials*, vol. 3, no. 3, pp. 278–314, 2018. [Online]. Available: https://doi.org/10.1016/j.bioactmat.2017.10.001

[94] G. Ruphuy, A. Saralegi, J. C. Lopes, M. M. Dias, and M. F. Barreiro, "Spray drying as a viable process to produce nano-hydroxyapatite/chitosan (n-HAp/CS) hybrid microparticles mimicking bone composition," *Advanced Powder Technology*, vol. 27, no. 2, pp. 575–583, 2016. [Online]. Available: https://doi.org/10.1016/j.apt.2016.02.010

[95] A. L. Boskey and R. Roy, "Cell culture systems for studies of bone and tooth mineralization," *Chemical reviews*, vol. 108, no. 11, pp. 4716–4733, 2008. [Online]. Available: https://doi.org/10.1021/cr0782473

[96] M. G. Albu, I. Titorencu, and M. V. Ghica, *Collagen-based drug delivery systems for tissue engineering*. chapter, 2011, vol. 17. [Online]. Available: https://doi.org/10.5772/22981

[97] R. Maynes, *Structure and function of collagen types*. Elsevier, 2012. [Online]. Available: https://doi.org/10.1016/B978-0-12-481280-2.X5001-6

[98] K. Gelse, E. Pöschl, and T. Aigner, "Collagens—structure, function, and biosynthesis," *Advanced drug delivery reviews*, vol. 55, no. 12, pp. 1531–1546, 2003. [Online]. Available: https://doi.org/10.1016/j.addr.2003.08.002

[99] J. R. Jones, "Reprint of: Review of bioactive glass: From hench to hybrids," *Acta biomaterialia*, vol. 23, pp. S53–S82, 2015. [Online]. Available: https://doi.org/10.1016/j.actbio.2012.08.023

[100] J. R. Jones, L. M. Ehrenfried, and L. L. Hench, "Optimising bioactive glass scaffolds for bone tissue engineering," *Biomaterials*, vol. 27, no. 7, pp. 964–973, 2006. [Online]. Available: https://doi.org/10.1016/j.biomaterials.2005.07.017

[101] M. Vallet-Regí, "Ceramics for medical applications," *Journal of the Chemical Society, Dalton Transactions*, no. 2, pp. 97–108, 2001. [Online]. Available: https://doi.org/10.1039/B007852M

[102] S. Yang, K.-F. Leong, Z. Du, and C.-K. Chua, "The design of scaffolds for use in tissue engineering. part i. traditional factors," *Tissue engineering*, vol. 7, no. 6, pp. 679–689, 2001. [Online]. Available: https://doi.org/10.1089/107632701753337645

[103] P. K. Chu and X. Liu, *Biomaterials fabrication and processing handbook*. CRC press, 2008.

[104] S. Yang, K.-F. Leong, Z. Du, and C.-K. Chua, "The design of scaffolds for use in tissue engineering. part ii. rapid prototyping techniques," *Tissue engineering*, vol. 8, no. 1, pp. 1–11, 2002. [Online]. Available: https://doi.org/10.1089/107632702753503009

[105] S. Best, A. Porter, E. Thian, and J. Huang, "Bioceramics: past, present and for the future," *Journal of the European Ceramic Society*, vol. 28, no. 7, pp. 1319–1327, 2008. [Online]. Available: https://doi.org/10.1016/j.jeurceramsoc.2007.12.001

[106] M. Šupová, "Problem of hydroxyapatite dispersion in polymer matrices: a review," *Journal of Materials Science: Materials in Medicine*, vol. 20, no. 6, pp. 1201–1213, 2009. [Online]. Available: https://doi.org/10.1007/s10856-009-3696-2

[107] R. Hwang, V. Mirshafiee, Y. Zhu, and T. Xia, "Current approaches for safer design of engineered nanomaterials," *Ecotoxicology and environmental safety*, vol. 166, pp. 294–300, 2018. [Online]. Available: https://doi.org/10.1016/j.ecoenv.2018.09.077

[108] A. Nouri and A. Sola, "Powder morphology in thermal spraying," *Journal of Advanced Manufacturing and Processing*, vol. 1, no. 3, p. e10020, 2019. [Online]. Available: https://doi.org/10.1002/amp2.10020

[109] A. B. D. Nandiyanto and K. Okuyama, "Progress in developing spray-drying methods for the production of controlled morphology particles: From the nanometer to submicrometer size ranges," *Advanced Powder Technology*, vol. 22, no. 1, pp. 1–19, 2011. [Online]. Available: https://doi.org/10.1016/j.apt.2010.09.011

[110] W. Julklang and B. Golman, "Numerical simulation of spray drying of hydroxyapatite nanoparticles," *Clean Technologies and Environmental Policy*, vol. 17, no. 5, pp. 1217–1226, 2015. [Online]. Available: https://doi.org/10.1007/s10098-015-0931-z

[111] B. W. Kanwate, R. V. Ballari, and T. G. Kudre, "Influence of spray-drying, freeze-drying and vacuum-drying on physicochemical and functional properties of gelatin from labeo rohita swim bladder," *International journal of biological macromolecules*, vol. 121, pp. 135–141, 2019. [Online]. Available: https://doi.org/10.1016/j.ijbiomac.2018.10.015

[112] G. Bertrand, P. Roy, C. Filiatre, and C. Coddet, "Spray-dried ceramic powders: A quantitative correlation between slurry characteristics and shapes of the granules," *Chemical Engineering Science*, vol. 60, no. 1, pp. 95–102, 2005. [Online]. Available: https://doi.org/10.1016/j.ces.2004.04.042

[113] D. M. Silva, H. K. N. Vyas, M. L. Sanderson-Smith, and V. Sencadas, "Development and optimization of ciprofloxacin-loaded gelatin microparticles by single-step spray-drying technique," *Powder technology*, vol. 330, pp. 201–209, 2018. [Online]. Available: https://doi.org/10.1016/j.powtec.2018.02.029

[114] A. Gharsallaoui, G. Roudaut, O. Chambin, A. Voilley, and R. Saurel, "Applications of spray-drying in microencapsulation of food ingredients: An overview," *Food research international*, vol. 40,

no. 9, pp. 1107–1121, 2007. [Online]. Available: https://doi.org/10.1016/j.foodres.2007.07.004

[115] I. Chopra, "The increasing use of silver-based products as antimicrobial agents: a useful development or a cause for concern?—authors response," *Journal of Antimicrobial Chemotherapy*, vol. 60, no. 2, p. 447–448, 2007.

[116] M. Ribeiro, F. J. Monteiro, and M. P. Ferraz, "Infection of orthopedic implants with emphasis on bacterial adhesion process and techniques used in studying bacterial-material interactions," *Biomatter*, vol. 2, no. 4, pp. 176–194, Oct. 2012. [Online]. Available: https://www.ncbi.nlm.nih.gov/pmc/articles/PMC3568104/

[117] A. Pfalzgraff, K. Brandenburg, and G. Weindl, "Antimicrobial Peptides and Their Therapeutic Potential for Bacterial Skin Infections and Wounds," *Frontiers in Pharmacology*, vol. 9, p. 281, 2018. [Online]. Available: 10.3389/fphar.2018.00281

[118] J. W. Alexander, "History of the medical use of silver," *Surgical Infections*, vol. 10, no. 3, p. 289–292, 2009.

[119] S. Castiglioni, A. Cazzaniga, L. Locatelli, and J. A. M. Maier, "Silver Nanoparticles in Orthopedic Applications: New Insights on Their Effects on Osteogenic Cells," *Nanomaterials (Basel, Switzerland)*, vol. 7, no. 6, May 2017. [Online]. Available: https://doi.org/10.3390/nano7060124

[120] P. J. Kelly and R. D. Arnell, "Magnetron sputtering: a review of recent developments and applications," *Vacuum*, vol. 56, pp. 159–172, Mar. 2000. [Online]. Available: http://www.sciencedirect.com/science/article/pii/S0042207X9900189X

[121] S. Chandra and P. Fauchais, "Formation of solid splats during thermal spray deposition," *Journal of Thermal Spray Technology*, vol. 18, no. 2, pp. 148–180, 2009. [Online]. Available: https://doi.org/10.1007/s11666-009-9294-5

[122] R. Kromer, S. Costil, J. Cormier, L. Berthe, P. Peyre, and D. Courapied, "Laser patterning pretreatment before thermal spraying: a technique to adapt and control the surface topography to thermomechanical loading and materials," *Journal of Thermal Spray Technology*, vol. 25, no. 3, pp. 401–410, 2016. [Online]. Available: https://doi.org/10.1007/s11666-015-0352-x

[123] M. Fukumoto, H. Nagai, and T. Yasui, "Influence of surface character change of substrate due to heating on flattening behavior of thermal sprayed particles," *Journal of thermal spray technology*, vol. 15, no. 4, pp. 759–764, 2006. [Online]. Available: https://doi.org/10.1361/105996306X146776

[124] M. S. Brown and C. B. Arnold, "Fundamentals of laser-material interaction and application to multiscale surface modification," in *Laser precision microfabrication*. Springer, 2010, pp. 91–120. [Online]. Available: https://doi.org/10.1007/978-3-642-10523-4_4

[125] D. Bäuerle, R. Denk, J. D. Pedarnig, K. Piglmayer, J. Heitz, and G. Schrems, "Perspectives of laser processing and chemistry," *Applied Physics A*, vol. 77, no. 2, pp. 203–207, 2003. [Online]. Available: https://doi.org/10.1117/12.482081

[126] B. N. Chichkov, C. Momma, S. Nolte, F. Von Alvensleben, and A. Tünnermann, "Femtosecond, picosecond and nanosecond laser ablation of solids," *Applied physics A*, vol. 63, no. 2, pp. 109–115, 1996. [Online]. Available: https://doi.org/10.1007/BF01567637

[127] W. M. Steen and J. Mazumder, *Laser material processing*. Springer science & business media, 2010. [Online]. Available: https://doi.org/10.1007/978-1-84996-062-5

[128] X. L. Mao, A. C. Ciocan, and R. E. Russo, "Preferential vaporization during laser ablation inductively coupled plasma atomic emission spectroscopy," *Applied spectroscopy*, vol. 52, no. 7, pp. 913–918, 1998. [Online]. Available: https://doi.org/10.1366/0003702981944706

[129] T. Marrocco, D. McCartney, P. Shipway, and A. Sturgeon, "Production of titanium deposits by cold-gas dynamic spray: numerical modeling and experimental characterization," *Journal of Thermal Spray Technology*, vol. 15, no. 2, pp. 263–272, 2006. [Online]. Available: https://doi.org/10.1361/105996306X108219

[130] C.-J. Li and W.-Y. Li, "Deposition characteristics of titanium coating in cold spraying," *Surface and Coatings Technology*, vol. 167, no. 2-3, pp. 278–283, 2003. [Online]. Available: https://doi.org/10.1016/S0257-8972(02)00919-2

[131] W. Wong, A. Rezaeian, E. Irissou, J. G. Legoux, and S. Yue, "Cold spray characteristics of commercially pure ti and ti-6al-4v," in *Advanced Materials Research*, vol. 89. Trans Tech Publ, 2010, pp. 639–644.

[132] H. Assadi, T. Schmidt, H. Richter, J.-O. Kliemann, K. Binder, F. Gärtner, T. Klassen, and H. Kreye, "On parameter selection in cold spraying," *Journal of thermal spray technology*, vol. 20, no. 6, pp. 1161–1176, 2011. [Online]. Available: https://doi.org/10.1007/s11666-011-9662-9

[133] M. Grujicic, C. Zhao, C. Tong, W. DeRosset, and D. Helfritch, "Analysis of the impact velocity of powder particles in the cold-gas dynamic-spray process," *Materials Science and Engineering: A*, vol. 368, no. 1-2, pp. 222–230, 2004. [Online]. Available: https://doi.org/10.1016/j.msea.2003.10.312

[134] A. Alkhimov, V. Kosarev, and S. Klinkov, "The features of cold spray nozzle design," *Journal of thermal spray technology*, vol. 10, no. 2, pp. 375–381, 2001. [Online]. Available: https://doi.org/10.1361/105996301770349466

[135] V. Nguyen, C. Wang, C. Thomas, and Z. Zhang, "Mechanical properties of single alginate microspheres determined by microcompression and finite element modelling," *Chemical engineering science*, vol. 64, no. 5, pp. 821–829, 2009. [Online]. Available: https://doi.org/10.1016/j.ces.2008.10.050

[136] S. F. Yap, M. Adams, J. Seville, and Z. Zhang, "Understanding the mechanical properties of single micro-particles and their compaction behaviour," *China Particuology*, vol. 4, no. 1, pp. 35–40, 2006. [Online]. Available: https://doi.org/10.1016/S1672-2515(07)60231-0

[137] Z. Zhang, G Sun, "Mechanical properties of melamine-formaldehyde microcapsules," *Journal of microencapsulation*, vol. 18, no. 5, pp. 593–602, 2001. [Online]. Available: https://doi.org/10.1080/02652040010019541

[138] N. Cinca, A. M. Vilardell, S. Dosta, A. Concustell, I. Garcia Cano, J. M. Guilemany, S. Estradé, A. Ruiz, and F. Peiró, "A new alternative for obtaining nanocrystalline bioactive coatings: study of hydroxyapatite deposition mechanisms by cold gas spraying," *Journal of the American Ceramic Society*, vol. 99, no. 4, pp. 1420–1428, 2016. [Online]. Available: https://doi.org/10.1111/jace.14076

[139] A. M. Vilardell, N. Cinca, A. Concustell, S. Dosta, I. G. Cano, and J. M. Guilemany, "Cold spray as an emerging technology for biocompatible and antibacterial coatings: state of art," *Journal of Materials Science*, vol. 50, no. 13, pp. 4441–4462, 2015. [Online]. Available: https://doi.org/10.1007/s10853-015-9013-1

[140] W. Jin and P. K. Chu, "Orthopedic implants," in *Encyclopedia of Biomedical Engineering*. Elsevier, 2019, pp. 425–439. [Online]. Available: https://doi.org/10.1016/B978-0-12-801238-3.10999-7

[141] M. Assad and N. Jackson, "Biocompatibility evaluation of orthopedic biomaterials and medical devices: A review of safety and efficacy models," *Encyclopedia of Biomedical Engineering*, p. 281–309, 2019. [Online]. Available: https://doi.org/10.1016/b978-0-12-801238-3.11104-3

[142] G. Thrivikraman, G. Madras, and B. Basu, "In vitro/in vivo assessment and mechanisms of toxicity of bioceramic materials and its wear particulates," *RSC Advances*, vol. 4, no. 25, pp. 12 763–12 781, 2014. [Online]. Available: https://doi.org/10.1039/C3RA44483J

[143] M.-F. Solá-Ruiz, C. Pérez-Martínez, J.-J. Martín-del Llano, C. Carda-Batalla, and C. Labaig-Rueda, "In vitro preliminary study of osteoblast response to surface roughness of titanium discs and topical application of melatonin," *Medicina oral, patologia oral y cirugia bucal*, vol. 20, no. 1, p. e88, 2015. [Online]. Available: doi:10.4317/medoral.19953

[144] G. H. Lee and J.-T. Kim, *Ultrasmall lanthanide oxide nanoparticles for biomedical imaging and therapy*. Woodhead Publishing, 2014.

[145] Ö. S. Aslantürk, *In vitro cytotoxicity and cell viability assays: principles, advantages, and disadvantages*. InTech, 2018, vol. 2.

[146] A. Gloria, R. De Santis, and L. Ambrosio, "Polymer-based composite scaffolds for tissue engineering," *Journal of Applied Biomaterials and Biomechanics*, vol. 8, no. 2, pp. 57–67, 2010. [Online]. Available: https://doi.org/10.1177/228080001000800201

[147] E. E. Golub and K. Boesze-Battaglia, "The role of alkaline phosphatase in mineralization," *Current opinion in Orthopaedics*, vol. 18, no. 5, pp. 444–448, 2007. [Online]. Available: https://doi.org/10.1097/BCO.0b013e3282630851

[148] T. Goto, T. Narushima, and K. Ueda, "Biological and biomedical coatings handbook-processing and characterization," *Boca Raton: CRC*, 2011.

Dépôts base hydroxyapatite élaborés par *cold spray* : architecture, nanostructure et bioactivité

Résumé : La projection dynamique à froid (CS) est considérée comme un procédé de revêtement à l'état solide par impact. Par conséquent, les effets néfastes de l'oxydation à haute température, de l'évaporation, de la fusion, de la cristallisation, des contraintes thermiques résiduelles, etc., rencontrés avec les techniques traditionnelles de projection thermique, sont minimisés, voire éliminés. Le procédé CS peut présenter un intérêt dans le domaine des revêtements biomédicaux pour l'ingénierie des tissus osseux (BTE), à savoir les revêtements d'hydroxyapatite (HAp). Le procédé CS peut éviter la transformation de la phase HAp en d'autres phosphates de calcium (phosphate tricalcique, phosphate tétracalcique, oxyde de calcium) pendant le dépôt. Ici, notre travail se concentre d'abord sur le dépôt par CS de matériaux à base de HAp tout en analysant en détail toutes les étapes du procédé (formation de "splats", processus d'adhésion et de croissance). Plus précisément, nous étudions l'influence des propriétés mécaniques de la poudre brute, l'état de surface du substrat (rugosité, dureté), la pression et la distance entre le "canon à poudres" et le substrat. Des revêtements de bonne qualité sont obtenus en optimisant les paramètres suscités. Il est démontré que la construction des dépôts résulte principalement de phénomènes physiques liés à la capacité d'empilement granulaire et à l'ancrage mécanique sur la rugosité du substrat. Aucun phénomène chimique n'est activé, ce qui conduit à des revêtements ayant une adhérence faible. En tirant profit du procédé CS, nous étendons dans un deuxième temps l'approche à de nouveaux revêtements hybrides bioactifs en introduisant du collagène, un bioverre ou des nanoparticules d'argent antimicrobiennes dans les poudres an amont. Les revêtements obtenus sont ensuite testés en termes microstructural, mécanique et biologique (in vitro) montrant une bonne biocompatibilité pour le BTE.

Mots clés : *Projection dynamique à froid, dépôts, hydroxyapatite, microstructure, propriétés.*

Hydroxyapatite-based architectured and nano-structured bioactive coatings fabricated by cold spray

Abstract: Cold spray (CS) is considered as a solid-state coating process by impact. As a result, the harmful effects of high-temperature oxidation, evaporation, melting, crystallization, residual thermal stresses, etc., encountered with traditional thermal spray techniques, are minimized or even eliminated. CS can be of interest in the field of biomedical coatings for Bone Tissue Engineering (BTE), namely hydroxyapatite (HAp) coatings. CS can avoid HAps phase transformation into other calcium phosphates (tricalcium phosphate, tetracalcium phosphate, calcium oxide) during the deposition.

Our work here first focuses on CS of HAp-based materials while analyzing in details all the CS processing steps (formation of "splats", adhesion process and further growth process). More specifically, the influence of the raw powder mechanical properties, substrate surface state (i.e. roughness,hardness), CS pressure and stand-off distance between the gun and the substrate, are investigated. Good quality coatings can be obtained while optimizing the aforementioned parameters. It is shown that the build-up of coatings is mostly due to physical phenomena linked to particles packing ability and mechanical anchor on the roughness of the substrate. No consolidation through chemical phenomena is activated leading to coatings with a poor adhesion.

Taking advantage of CS, in a second step we extend the approach to novel functionaly-graded enhanced bio-active hybrid coatings introducing whether collagen, bioglass or antimicrobial silver nanoparticles in the HAp feestocks. The as-obtained coatings are then tested at the microstructural, mechanical and biological (in vitro) levels showing good biocompatibility for BTE.

Keywords: *Cold spray, coatings, hydroxyapatite, microstructure, properties.*